Fermilab

FERMILAB-THESIS-1997-30

**UNIVERSITY OF CALIFORNIA**

**Los Angeles**

# Parasitic extraction of 900 GeV/c protons from the Tevatron using a bent silicon crystal and measurement of the $b\bar{b}$ production cross section at $\sqrt{s} = 38.8\ GeV$

A dissertation submitted in partial satisfaction of the

requirements for the degree Doctor of Philosophy

in Physics

by

**Sathyadev Ramachandran**

1997

The dissertation of Sathyadev Ramachandran is approved.

W. Slater

W. Mangione-Smith

D. B. Cline, Committee Chair

University of California, Los Angeles

1997

To youthful days spent learning physics...

# Contents

# List of Figures

# List of Tables

# ACKNOWLEDGEMENTS

I would like to acknowledge the support and encouragement from my thesis advisor Prof. D. B. Cline prior to my enrollment at UCLA to pursue my interest in High Energy Physics and helping me sustain it in course of my graduate studies. I would also like to acknowledge the efforts by T. Murphy, L. Spiegel, R. A. Carrigan, W. Gabella, A. Bogacz, A. McManus and G. Corti in providing me with invaluable advise for the successful completion of my work at Fermilab and my dissertation committee members Prof. W. Slater and Prof. W. Mangione-Smith for their efforts in guiding me through the final stages of the dissertation. Jim Kolonko and Penny Lucky made life much easier with help on the administrative side while at UCLA. Fellow students: A. Boden, P. Hanlet, C. Durandet, A. Ledovskoy, K. Hagan, A. Blankman, Z. Cao need special mention for their help and friendship. Many thanks to all you guys: Arijit, Ashutosh, Brajesh, Bala, Carlos, Dhiman, Sudeshna, Mrinmoy, Vipin, Prakash, Prem, Prajakta, Sailesh, Harsh and Harpreet for your companionship in sharing the best and worst times while at Fermilab. My friends from IITM days: Roddy, Sathya, Raghu and Lokki for their e-mail friendships during the first few years in the States and later by Karra, Siva and others. My parents for their enormous patience and everlasting encouragement to pursue my dreams. To my teachers who have helped me all along and in particular Prof. Deshmukh (IITM) who strongly advised me to pursue higher studies in the United States.

# VITA

| | |
|---|---|
| January 16, 1966 | Born, Kodungallur, Kerala, India |
| 1987 | B.Sc.(Honours) Physics<br>Jadavpur University<br>Calcutta, India |
| 1989 | M.Sc. Physics<br>Indian Institute of Technology<br>Madras, India |
| 1991-1996 | Research Assistant<br>University of California, Los Angeles |
| 1993-1996 | Stationed at Fermilab |

# ABSTRACT OF THE DISSERTATION

## Parasitic extraction of 900 GeV/c protons from the Tevatron using a bent silicon crystal and measurement of the $b\bar{b}$ production cross section at $\sqrt{s} = 38.8\ GeV$

by

Sathyadev Ramachandran
Doctor of Philosophy in Physics
University of California, Los Angeles, 1997
Professor D. B. Cline, Chair

This dissertation discusses results from an experiment demonstrating the feasibility of a novel extraction scheme using channeling in a bent crystal at future high-energy colliders for doing heavy flavor physics in a fixed target environment concurrently with collider experiments. In the second half of this dissertation we present the results from a measurement of the inclusive cross-section for $b\bar{b}$ production at the center-of-mass energy of 38.8 $GeV$ using the semileptonic decays of the beauty mesons.

# Chapter 1

# Introduction

High-energy physics has a rich history of creating new tools to enhance its ability in solving problems faced by the limitation of available technology at each phase of its growth. The discovery of electrons and X-rays early on in this century with the invention of the discharge tube was the first step in which began the field of particle physics in our quest to understand the fundamental laws of nature. Close on the heels of this discovery there came a virtual revolution of ideas as the urge to further explore the constituents of matter grew, and with it the need to develop techniques to solve the puzzles of nature. Present day accelerators like the Tevatron are the end product of a long chain of discoveries and inventions made in this century. The primary motivation has been always driven by the need to produce higher energy beams to look for new particles that seemed to proliferate the microscopic world in a series of experiments done over three decades from the 1940's to the 1970's. One of the earliest steps in this direction was the pioneering effort in the late 1920's by E. Lawrence in constructing the first circular accelerator which culminated in the idea of synchronous acceleration which has made possible the development of machines like the Tevatron. With the need to look for rare processes to better constrain our theoretical models and also to search for exotic particles, ever increasing demands were being made on the available accelerator techniques. In order to look for particles with higher masses came the idea to exploit the larger centre-of-mass energy available in beam collisions compared to the older technique of having the target at rest. This meant a need to optimise the beam parameters to increase the chances for interaction and ideas like stochastic cooling were developed to improve on the performance of collider beam luminosity.

In this same spirit an experiment was proposed at Fermilab in the early 90's to test a new technique of beam extraction for the Superconducting Super Collider which was to be built near Dallas in Texas. The extraction scheme proposed for the SSC was to employ a relatively well known concept of channeling, first seen in the 1960's with very low energy beams. The idea was to extract a reasonable fraction of the circulating beam at 20 TeV to be used for a heavy-flavor fixed target experiment which was being proposed to run parasitically with collider operations at the SSC. Conventional methods of beam extraction at such high energies poses practical problems with no cost-effective or elegant solution. Electrostatic septa which are routinely used for extraction both at Fermilab and the SPS at CERN, are insufficient to provide the larger momentum kick required for a 20 TeV beam like the one at the SSC or at future trans-TeV accelerators. The larger length needed for the septa makes its construction and alignment difficult. The larger septum thickness required poses a problem as the needed transverse step-size in one turn for the kicked beam should be such as to take them over the septa wires. Since the new extraction scheme proposed for the SSC was not a proven technique, experiment E853 [8] at Fermilab proposed to demonstrate the feasibility of this idea by extracting $10^{-6}/sec$ of the circulating proton beam with an intensity of $10^{12}$ protons in the Tevatron at 900 GeV/c.

The extraction scheme proposed for the SSC was for the Super Fixed Target Beauty physics experiment. A similar experiment E771 was getting ready to take data at Fermilab with a beam energy of 800 GeV/c during the early 1990's. At this time the collider detectors at Fermilab were also on the threshold of producing quality heavy flavor physics results. Measurements that can be done at the collider and in a fixed target environment complement each other as they correspond to vastly different centre-of-mass energies. At the time of writing this document there is a great deal of interest in measuring the beauty cross-section, since the experiment HERA-B, which is in the same energy domain as the Fermilab fixed target hadroproduction experiments and is scheduled to take data around 1998. The motivation to do B physics experiments lies in the ultimate goal to look for CP violation. It is yet to be seen whether this can be achieved at experiments like HERA-B or will be first seen at the various dedicated collider beauty factories like the ones at Cornell or SLAC which are electron machines. In this document is also presented the results from a cross-section measurement of $b\bar{b}$ production from the Fermilab experiment E771 which wrote close to 1.47 million dimuon triggers during a brief six-week run in late 1991.

In the course of this thesis a case will be made for using extraction schemes like channeling to get a very high-energy beam from a future collider facility to do fixed target experiments in heavy flavor physics. Quantitative estimates will be made of beam Luminosity required for the various physics programs that can be initiated at a facility like Fermilab using channeling in a bent crystal as a possible parasitic extraction scheme.

# PART I

## Parasitic extraction of 900 GeV/c protons from the Tevatron using a bent silicon crystal

# Chapter 2

# Crystal Extraction

## 2.1 Phenomena of Channeling

The transmission of charged particles through matter is determined by its interaction with the atoms that make up matter. Earlier in the century the energy loss of charged particles resulting from interactions with matter was calculated assuming a random distribution of atoms which describe the amorphous state. This is the well known Bethe-Bloch equation for energy loss. However, it came to be known later that crystalline materials showed higher transmission rates for charged particles passing through them when they happened to be aligned along certain directions as dictated by the symmetry of the crystal lattice. A crystal being a regular arrangement of atoms sitting at fixed lattice positions, a charged particle passing through it will see certain directions as more open than others. Intuitively, stated the charged particle projectile sees atoms as arranged periodically along strings or in planes. Hence the motion along this direction is determined by its coherent scattering off these strings or planes of atoms and not by individual scattering as is the case when passing through an amorphous material or when it is not aligned along these more open directions within a crystal. The channeling effect was first seen in the early sixties from the energy loss of positive ions in crystalline materials.

The first observations of bending channeling at high energies (GeV range) were done at the PS at CERN and also at Serpukhov. Since then many experiments have been done with higher energies at various laboratories around the world. The most recent one was at Fermilab at the highest energy so far with 900 GeV/c proton beam.

### 2.1.1 Classical Approximation

It is quite interesting to note that a classical mechanics calculation suffices to understand most of the features observed for the transmission of a projectile through a crystal lattice, especially so when incident with a small angle to an axial direction, resulting in a strong correlation between successive collisions with a string or plane of atoms. This observation led Lindhard to introduce the continuum model where the charges from individual atoms in a string or plane is smeared along or over it respectively. The transverse and longitudinal motions of the projectile are separated, as the interaction of the projectile with this continuum of charge is independent of the longitudinal position of the particle. The transverse motion in the case of having a smeared plane of charge is one dimensional as opposed to the case of a smeared string where it is two-dimensional.

The continuum potential is given by,

$$U(y) = N\ d_p \int_{-\infty}^{\infty} V(\sqrt{x^2 + y^2 + z^2})\ dx\ dy \tag{2.1}$$

where $N$ is the atomic density, and $d_p$ the planar spacing, and $y$ represents the transverse co-ordinate to the crystal plane. In the continuum model since the potential is independent of the longitudinal co-ordinates x, z in the planar case the *transverse energy* $E_\perp$ is a conserved quantity.

$$E_\perp = \frac{p_\perp^2}{2\gamma M} + U(y) = 1/2pv\psi^2 + U(y) \tag{2.2}$$

where the two terms are the kinetic energy and potential energy respectively, p is the momentum of the incident particle and $\psi$ is its local angle to the plane direction. The transverse energy is given by the value it acquires at the surface of the crystal,

$$E_\perp = E_\perp(z = 0) = 1/2pv{\psi_0}^2 + U(y_0) \tag{2.3}$$

This implies a distribution in transverse energy for a perfectly aligned parallel beam with respect to the crytalline axis.

The potential used by Lindhard in his calculations is the atomic screened Coulomb potential which has the following analytical form [3],

$$V(r) = \frac{Z_1 Z_2 e^2}{r}(1 - \frac{r}{(r^2 + C^2 a^2)^{1/2}}) \tag{2.4}$$

where, C $\approx \sqrt{3}$ is a constant and $a = 0.8853 a_0 (Z_1^{2/3} + Z_2^{2/3})^{-1/2}$ gives the screening length where $a_0$ is the Bohr radius. The critical angle can be derived from this as discussed in the next section.

The planar continuum potential after averaging over the plane for the above form is,

$$U(y) = 2\pi Z_1 Z_2 e^2 N d_p [(y^2 + C^2 a^2)^{1/2} - y] \tag{2.5}$$

where y is the distance from the plane and $d_p$ is the inter-planar distance.

### 2.1.2 Critical Angles

The *critical channeling angle* is usually defined as the minimum angle of incidence of the particle, with respect to the string of atoms in the case of axial channeling or the plane of atoms in the case of planar channeling, that allows it to penetrate into the string or the plane as the case may be for a given crystal type with a certain symmetry and particle energy. This is determined by equating the transverse kinetic energy to the maximum height of the electrostatic potential well seen by the particle due to the atoms in the lattice.

$$E_{\perp}^{crit} = \frac{1}{2} pv\psi_{crit}^2 = U^{max} \tag{2.6}$$

The critical angles for axial and planar cases are given by $\psi_1$ and $\psi_p$ respectively,

$$\psi_1 = \sqrt{\frac{4Z_1Z_2e^2}{pvd}} \tag{2.7}$$

$$\psi_p = \sqrt{4Z_1Z_2e^2Nd_pCa/pv} \tag{2.8}$$

### 2.1.3 Dechanneling

In the previous section while deriving the incidence angle value at which the particle does not channel, we made a naive assumption about the stability of the potential well and its essentially static behaviour with time. In reality the crystal atoms located at each lattice site has thermal vibrations and the presence of electrons in the vicinity of the lattice sites also induces perturbations to the motion of the particle in the continuum potential. This leads to a change in the transverse energy, on an average which increases with penetration. This results in dechanneling. The source of this loss depends on the transverse energy of the beam. For low values of transverse energy, it is the scattering with the electrons that is important, though at higher energies nuclear scattering begins to dominate.

For well channeled particles, their depletion due to the dechanneling process can be approximated by,

$$n = n_0 \; exp(-z/L_0) \tag{2.9}$$

where the dechanneling length $L_0$ scales linearly with momentum. The dechanneling lengths for negative particles is shorter as they are more likely to be around regions closer to the nucleus due to Coulomb attraction and hence get dechanneled sooner.

## 2.2 Channeling Application

The phenomenon of channeling has been used for a wide variety of applications in solid-state physics to high-energy physics. Low energy channeling as in solid-state physics is useful in determining defects in crystals and material characterisations. The high magnetic field that relativistic particles experience as they pass through a crystal was used in a Fermilab experiment E761 [71] to measure the magnetic moment of the $\Sigma^-$.

### 2.2.1 Channeling in Bent crystals

All the discussion so far had to do with straight crystals. It has been seen that when crystals are bent elastically, the channeled particles still follow the bent planes in the crystal. A bent crystal with a constant curvature can be described in the continuum approximation by introducing a centrifugal force modifying the effective potential the particle sees to,

$$Y_{eff}(y) = Y(y) - \kappa pvy \tag{2.10}$$

where y is the distance from the centerline between the atomic planes and $\kappa = 1/R$, where R is the radius of curvature. The effect of the bending is to shift the particle trajectories towards the outer atomic plane, and the potential barrier is lowered reducing the critical angle for channeling as shown in fig. 2.2.

It was shown by Tsyganov that there is a critical radius of curvature $R_c$ for which there is no potential well and hence no channeling. This is reached when $Y_{eff}$ has a minimum at $x = d_p/2$, which gives

$$R_c = pv/\pi Z_1 Z_2 e^2 N d_p \tag{2.11}$$

### 2.2.2 Beam Extraction Application

Deflection of a beam of charged particles using a curved crystal is quite different from the deflection achieved in an external magnetic field or electrostatic field in that it is entirely determined by the physical curvature of the atomic planes along which the particles are channeled. A useful choice from the many atomic planes in a crystal is one of low Miller index value such as the (1,1,0) plane. Since the deflection is independent of the particle energy or momentum, this has a distinct advantage for its application as an extraction system.

In a bent crystal the equilibrium planar trajectory moves away from the middle of the planar channel (see fig. 2.2). This is a result of the lowering of one side of the continuum potential well. Theoretically total dechanneling sets in when the

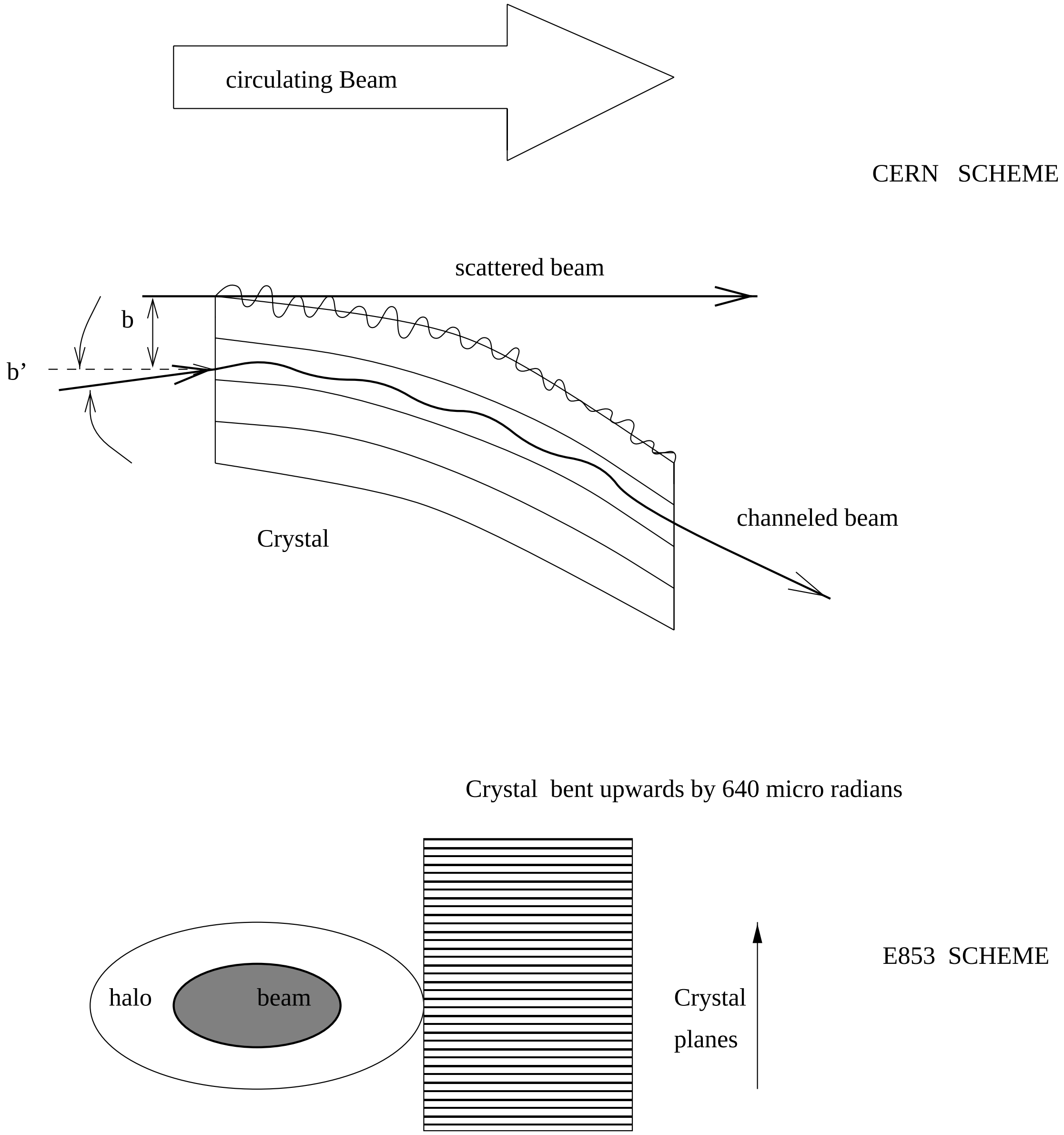

Figure 2.1: Channeling in Bent crystal. Shown here is the scheme used in the CERN experiment and that used in the Fermilab experiment. At CERN the beam intercepts the crystal across the planes. Hence the incident beam need to penetrate deep into the crystal to avoid the surface irregularities. In the Fermilab scheme the beam enters the crystal along the planes and gets bent upward by the crystal.

Figure 2.2: Planar potential for straight and bent crystal

equilibrium trajectory gets as close as the Thomas-Fermi screening distance from the atomic plane. This critical radius of curvature is an extreme lower limit and is not of any special concern for us in achieving a total deflection of 640 $\mu$radian with a 4 $cm$ long Silicon crystal. An important requirement on the particle beam for deflection is that it must be incident within the critical angle for channeling perpendicular to the particular plane used. Beam divergence parallel to the atomic planes is inconsequential.

The goal of parasitic extraction can be achieved with different schemes which depend on the lattice parameters at the crystal location. Of interest are those schemes which leave the core of the beam undisturbed while moving the particles in the halo of the beam onto the crystal surface. The RF manipulation schemes proposed need a large horizontal dispersion at the crystal location to give a typical synchrotron displacement times the dispersion comparable to the beam $\sigma_x$. By generating a signal that creates large particle diffusion rates only for greater synchrotron amplitudes, it would be possible to preserve the luminosity lifetime at the same time while maximizing the extraction efficiency.

### About the Experiment

The goal of the experiment is to extract one million 900 $GeV/c$ protons with $10^{12}$ protons circulating in the Tevatron, to study the extraction efficiency, also to show that the luminosity lifetime of the circulating beam is not adversely affected and that no intolerable backgrounds are created for the two Tevatron collider experiments.

The experiment is located in the C0 straight section of the Tevatron abort line. A missing half-dipole (three-bend magnetic dogleg) provides a 4 milliradian horizontal kick so that the abort line can clear the magnets at the downstream end of the straight section. The crystal is placed at the side of the beam with an upward curvature of 640 $\mu$radian, sufficient to deflect the beam halo that strikes the crystal into the field-free region of the Lambertson magnets. Then the extracted beam traverses the two instrumented air gaps 40 *meters* apart and approximately 100 *meters* downstream of the position of the crystal and finally enters the beam dump. The air-gaps are instrumented with two scintillators and two silicon-strip planes each to count the extracted beam and measure its trajectory precisely. The scintillators also provide the trigger for the silicon planes. A fluorescent screen coupled to a CCD camera also provides a digital readout of the beam-profile for run-time diagnostics.

The most critical parameter is the alignment of the vertical angle of the crystal with the beam angle for channeling to occur. To align the beam quickly with the crystal, the crystal is mounted at the upstream end of a 1 *meter* long beam pipe which ends with articulating bellows. Two precision motors in x and y at each end of the pipe allow for the alignment of the crystal with four degrees of freedom. There is also a coarse horizontal stepping motor used to plunge the crystal holder in and out of the beam line so that when not in use, the crystal is completely outside of the Tevatron aperture.

Given that the Tevatron beam has a vertical angular divergence of 11.5 $\mu radians$ and that at the Tevatron energy the critical angle of the crystal is 5.2 $\mu radians$, the alignment must be done to within 10 $\mu radians$ for channeling to ocuur. The tests done by us to study the reproducibilty and linearity of the goniometer precision movements show that this is easily satisfied. We were able to produce step-sizes of the order of 2.5 *microns* with each precision motor which translates to

2.5 $\mu$*radians* in angle with the 1 *meter* long lever-arm of the goniometer. The plunger mechanism was also tested satisfactorily to meet the reproducibility of the crystal positioning with every excursion of the crystal holder out of the beam-pipe. These measurements of alignment of the crystal holder surface with respect to goniometer coordinates were done using CODAX, a co-ordinate measuring machine with an accuracy of the order of a micron.

# Chapter 3

# E853 Apparatus

This chapter describes in detail the three main aspects that define the experiment E853. The Tevatron as the provider of the beam at 900 GeV/c for extraction is described highlighting the various stages of proton beam till its final delivery to our extraction device. A full section is devoted to the goniometer operations and calibration which are critical for successful alignment and reproducibility of the crystal motion during each study session. The last section is mostly related to the various instrumentation that were installed specifically for E853 and those which were already part of the Tevatron diagnostics which came useful for our purpose.

## 3.1 Tevatron

### 3.1.1 Introduction

The accelerator setup at Fermilab is done in several stages and is shown in fig. 3.1. It begins at the Preaccelerator consisting of a negative hydrogen ion source, a Cockcroft-Walton generator, an electrostatic accelerating column and a transport

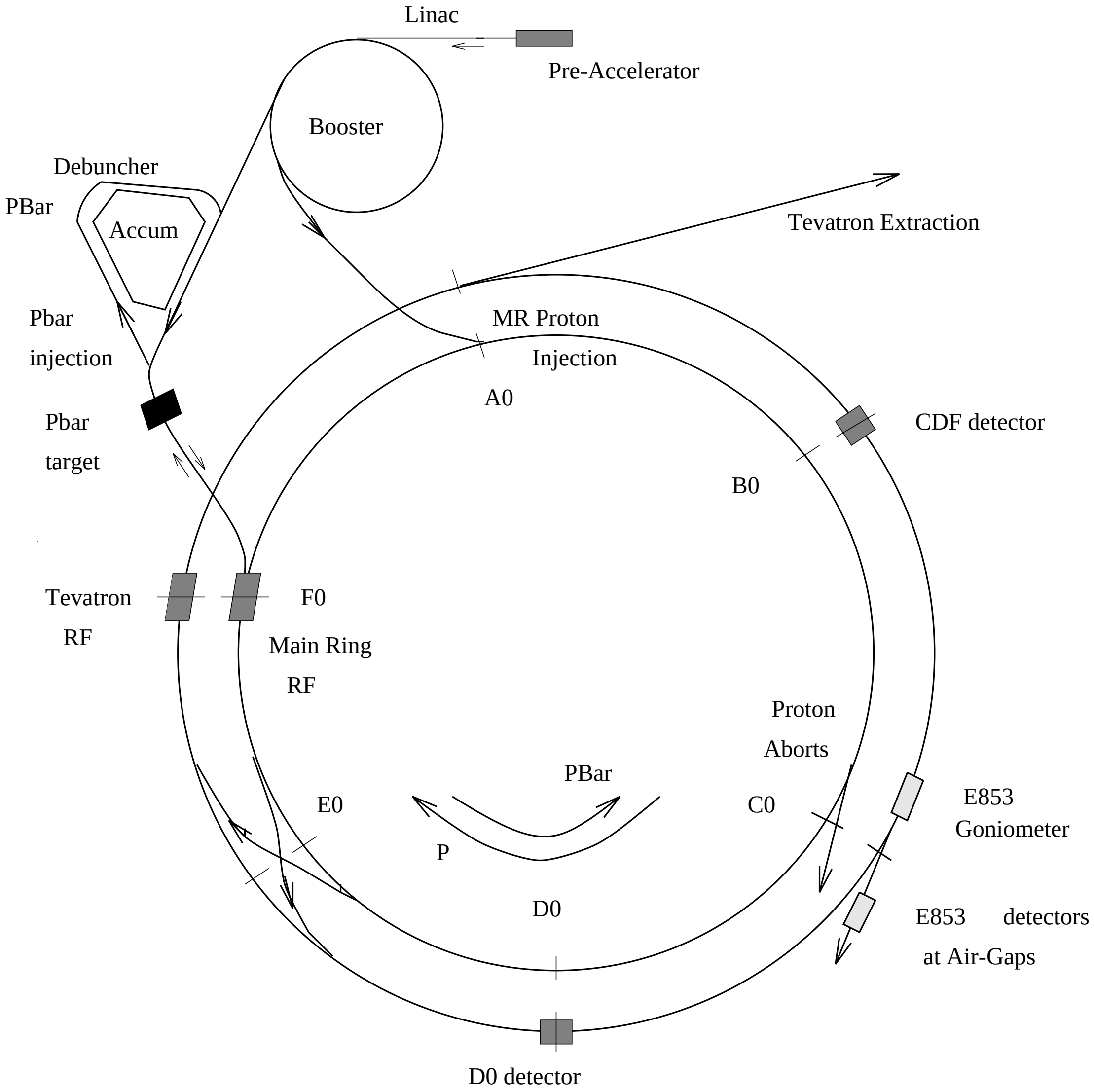

Figure 3.1: Layout of the Accelerator at Fermilab. E853 was located at C0. The air-gaps in the abort line were instrumented with scintillation detectors to count the extracted beam. Other elements used by E853 were the kicker magnet at E17 and the horizontal damper at F11, both of which are not shown in the picture.

line that feeds the beam into the Linac. The negative hydrogen ions are produced at 18 KeV in the source and accelerated upto 750 KeV and bunched by a single-gap RF cavity at 201.24 MHz before being injected into the Linac rf. The Linac is a two-stage machine which produces a pulsed beam of 400 MeV $H^-$ ions which is injected into the Booster. The first stage of the Linac only accelerates the ions to 116 MeV. The second stage has cavities that resonate with the fourth multiple of the first stage, 805 MHz.

The 400 MeV $H^-$ from the Linac is accelerated after charge-exchange injection at a rate of 15 Hz by the Booster to 8 GeV for injection into the Main Ring. The Booster is 151 m in diameter and is made of 96 dipole/quadrapole combinations and 17 cavity resonators. The beam at extraction from the Booster has the RF frequency of 52.813 MHz and is phase locked to the Main Ring RF. There are 84 RF buckets in the Booster.

The Main Ring is a 400 GeV proton synchrotron with a radius of 1000 m. It presently serves as a 150 GeV injector of protons and anti-protons for the Tevatron as well as for a 120 GeV beam used to produce anti-protons. It is comprised of 774 dipole magnets, 240 quadrupole magnets and 18 RF cavities. It contains 1113 RF buckets operating at 53 MHz.

The Tevatron is similar to the Main Ring in the structure of its basic lattice, but it uses superconducting magnets. In the collider mode it has “6 on 6” bunches. At the begining of the store six proton bunches are injected individually into the Tevatron followed by the same number of bunches for anti-protons. After injection they are ramped to 900 GeV for each beam. The bunch spacing alternates between 186 and 187 RF buckets due to the harmonic number being an odd number. The beam crossing happens every 3.5 $\mu sec$ and each bucket is 18.8 nsec long. Once at flattop, the Tevatron continues to circulate the beam for several hours till various factors reduce the beam intensity. Each such session is called a store.

### 3.1.2 C0 Abort Lattice

Most of the E853 related instrumentation is located along the C0 abort line. The abort lattice was designed to have an extraction system that would be fast (one turn) and clean so that it does not pose a problem for the string of superconducting magnets in the Tevatron. It consists of kicker magnets and magnetic septa and has a long lever arm so as to ensure adequate beam separation.

To design the abort line keeping in mind the above mentioned constraints an unorthodox solution was adopted by reducing the length of the B48-3 dipole in half, together with the C11-3 dipole. This provided for a 4 mrad change in the Tevatron orbit which angled the beam away from the magnets downstream and towards the beam dump. The missing 8 mrad bend by the removal of the half-dipoles had to be supplied by warm magnets in the straight section itself. These are the Lambertson and the current-sheet septa, where the circulating beam is in the field region and the aborted beam in the field free region. The horizontal geometry is shown in fig. 3.2 and the vertical geometry is a straight line above that of the Tevatron.

The abort for a 1000 GeV beam is achieved with four kicker modules with peak fields of 3.7 kGauss with a rise-time of 1.5 $\mu$sec. The Lambertson magnets in the upstream end of the straight-section provide the initial beam separation. With a maximum field value of 11.09 kGauss a string of three magnets provide for a 5.5 mrad bend. The current septum magnets provide the extra 3 mrad bend required for a closed orbit for the circulating beam.

### 3.1.3 Kicker Magnet at E17

In all kick mode studies done the kicker magnet located at E17 along the Tevatron lattice was used to impart an instantaneous kick in the transverse plane to the beam, such that this led to a significant step-size into the face of the crystal by the beam in the first turn around the Tevatron. The kick is applied only to a single bunch of the six bunches in the machine. The nominal value used for the kicker voltage was 10 kVolt. At 5 KVolt we did not see sufficient beam perturbation to get to hit the crystal face. The decay time of the kicker voltage was a few $\mu seconds$. The maximum step size achieved at the crystal with a 10 Kvolt kick was 500 $\mu m$.

### 3.1.4 Horizontal Damper at F11

For some diffusion mode studies the horizontal damper at F11 was used to introduce noise in the transverse phase-space to increase the extraction rate. The associated beam growth leads to multiple scattering of the large angle halo particles encountering the crystal on successive turns. These particles get channeled on future traversals through the crystal provided they have an incidence angle within the critical angle of acceptance. Noise induced diffusion studies were carried out only in a couple of runs to study its effect on the extraction efficiency. This mode cannot be used for parasitic extraction due to its destructive effect on the beam.

### 3.1.5 Loss Monitors

As part of beam diagnostics of the Accelerator, BPM's provide the amount of circulating beam left in the machine at any time during the course of a store. This is a time averaged quantity over many turns in the ring. IBEAMS can be easily read off an accelerator parameter page. IBEAMS measures the net loss rate in the ring, not just that due to the crystal. IBEAMS is still a useful quantity for normalising the extraction rate in the diffusion mode as in this mode the extraction process happens over a period of the order of hundreds of turns.

### 3.1.6 Flying Wires

This is device used for beam profile measurements in the Tevarton. A thin carbon-fiber filament is flipped through the beam with a speed of ≈ 5 m/sec. The secondary particles from the interaction of the beam with the carbon filament is then detected as a function of time using a scintillator telescope, from which the beam intensity profile can be measured.

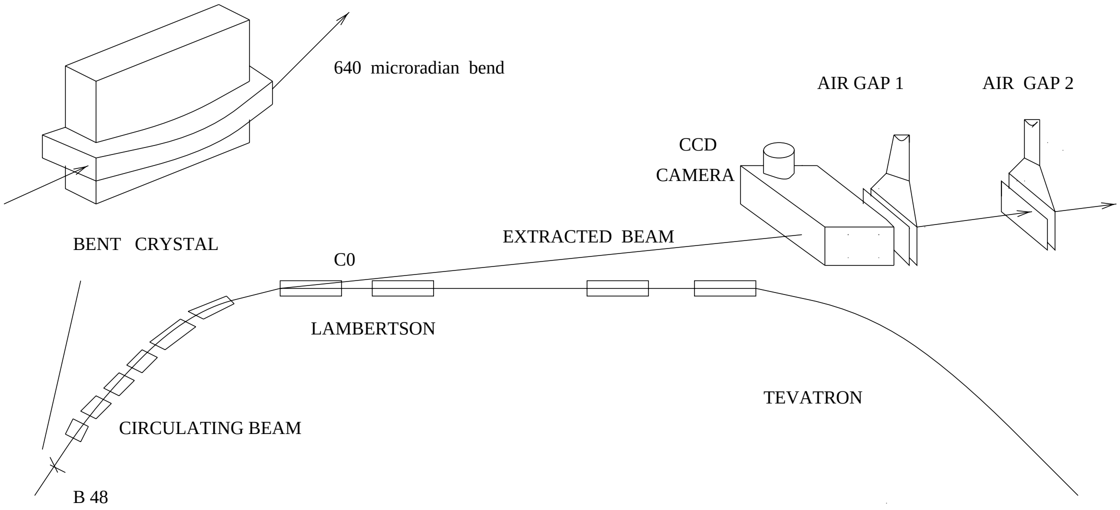

Figure 3.2: Shown here is the C0 area where the extracted beam goes into the field free region of the Lambertson magnet and is detected by the instrumentation located in the air gaps. Also shown is the location of the bent crystal at B48.

## 3.2 Goniometer

The goniometer is essentially a meter long pipe with the crystal positioned at one end of it on a retractable base. Each end of the pipe is placed on tables which can move either end of the pipe in the horizontal plane as well as in the vertical plane. The upstream end of the pipe has a port where the retractable mechanism is located. The driver for this is on an independent table with its own stepping motor. The step-size needed for this is not as fine as that required for the x and y motions of the goniometer pipe. There are five stepping motors for each degree of motion allowed for the goniometer.

### 3.2.1 4-point Bender

The bending mechanism for the crystal is located on the flat base at the end of the retraction mechanism mentioned earlier. In fact, the crystal is pre-bent by the bender tested for its bend angle before installation in the goniometer. An in-situ measurement of the bend angle was also done to ensure the integrity of the bend after its installation in the Tevatron.

The bending design chosen for E853 was that of a 4-point bender. A schematic of the design is shown in figure 3.2. Beyond the outer points of support for the bend the crystal has a straight overhang. More details on the design aspect of this can be found elsewhere [7].

### 3.2.2 Reproducibility Studies

Extensive reproducibility studies were carried out on table movements. These were done for different load conditions to simulate the real conditions with the meter-long insert attached to the tables. We verified the minimum step-size on the x,y motion stepping motors (2.5 $\mu$m) and on the motor used by the retraction mechanism (12.5 $\mu$m) using a high resolution (1 $\mu$m) optical encoder. The backlash error is of the order of 3 to 4 $\mu$m.

## 3.3 Extraction Line Instrumentation

The abort line at C0 is where the kicked beam enter to travel down into the beam dump during normal abort operations. Hence, the crystal bend angle of 640 $\mu$radians was chosen so as to bend the beam by the right amount at B48 so that it sees the full aperture of the abort line when it reaches C0 and travels down to the beam dump. Also along the abort line are two air gaps where we placed our various instruments for beam detection and measurement. In the next few sections a more detailed look at these devices is provided.

### 3.3.1 Scintillation Counters

A total of eight plastic scintillation counters of various shapes and sizes were used to monitor the beam flux close to the crystal and along the extraction line. These scintillators were coupled to the phototube using standard techniques to ensure maximum light collection. The phototube bases used were not all of the same kind. They ranged from 10-stage to 14-stage bases. The plastic was wrapped in aluminium foil and sealed with black tape to avoid any light leaks. These were then tested with radioactive sources and efficiencies were measured for each of the counters using Cosmic rays and a telescope setup. A plateau curve was also determined for each of these scintillator-phototube-high voltage base combinations

| counter | dimension | thickness | comments |
|---|---|---|---|
| U1 | 12 *in* wide | 1/2 *in* | 1/2 meter from xtal below beam pipe |
| U2 | 12 *in* wide | 1/2 *in* | 1/2 meter from xtal below beam pipe |
| AG1 | 1.25 *in* × 1.25 *in* | 1/4 *in* | 2 identical counters |
| AG2 | 1.25 *in* × 1.25 *in* | 1/4 *in* | 2 identical counters |
| FIN1 | 2 *in* × 1/32 *in* | 1/4 *in* | Horizontal |
| FIN2 | 2 *in* × 1/16 *in* | 1/4 *in* | Vertical |
| CAL | 2 *in* × 3/4 *in* | 1/4 *in* | Vertical |

Table 3.1: Counter sizes

before they were installed in the tunnel. From these curves one could determine the optimum high voltage values to be set on each of the counters to detect single particles in the diffusion mode where the particle flux expected is small enough to make it a counting experiment. Whereas in the kick mode of operation an instantaneous kick is imparted to the bunch as a whole horizontally, moving it deep into the crystal. As a result the fraction of the beam that gets extracted down the C0 abort line in the first few turns is large with the possibility of saturating the counters. Assuming a mere 10% extraction efficiency, and a circulating beam intensity of $1.0 \times 10^{10}$ per bunch, one can naively expect $10^9$ protons down the extraction line in a single RF bucket. A large flux of this nature can saturate either the counter itself or the ADCs being used to do charge integration. Hence, the voltages were selected for the kick mode after considerable tuning so as to avoid saturation. A summary table is given for all the counter characteristics.

### 3.3.2 CCD Camera

The CCD camera works in conjunction with the fluorescent screen which sits along the Tevatron extraction line at the first air gap. The screen is tilted at an angle of $45^0$, with the camera pointing at it $90^0$ from the beam line. When the proton beam hits the screen lighting it up, the image is captured and stored with the help of 'Frame Grabber' software available on a Macintosh platform. The image gets stored as a binary file which can be analysed later for measuring the intensity distribution in both the horizontal and vertical projections, from which one can also infer the beam size after the kicked beam is deflected by the bent crystal into the extraction line. Note, the beam is kicked only horizontally but the crystal deflects it in the vertical plane into the C0 abort line. The usefulness of the camera is mostly in the kick mode of operation, as there are enough beam particles to leave an image within the response time of the fluorescent screen. A large flux of $10^{10}$ protons saturates the screen, so that it is very difficult to extract reliable information on the beam intensity from the camera. Also, calibrating the CCD turned out to be a problem because of the auto-gain feature of the camera itself. The 'Frame-Grabber' can be configured to run in the free-wheeling mode as well as the triggered mode. During diffusion studies the former was used, but as the intensities extracted are very low per bucket ($19nsec$) it is very difficult to see a clear beam spot as can be seen in the kick mode. Despite the short comings of this device at both extremes of beam intensity values, it provides for a useful visual tool to guide one during the initial setup for crystal alignment. In our case before we saw channeling the CCD was useful in determining the aborted beam position with respect to the aperture of the Lambertson magnets.

## 3.4 Data Collection Procedure

Here we describe how the data collection was done in both modes of operation. Central to this is the Data Acquisition System developed to store information from the scintillation counters as well as the Silicon micro-strip detectors. Raw signals from the various counters at the air gaps are sent upstairs via RG-58 cables to the portakamps where they are used to form various logical combinations to be used as a trigger for the DAQ and also to monitor the individual as well as coincidence rates with the changing conditions in the experiment.

### 3.4.1 Logic Diagrams/DAQ

The raw signals from all the counters are split using a home-made star-network of resistors. Each counter signal is fed into an ADC unit which sits in the CAMAC crate which communicates directly with the DAQ program. During different runs a few counter signals were also stored into the ADC as decades of 10 and 100. A detailed version of the logic elements is presented in the following diagrams which are mostly self-explanatory.

### 3.4.2 DAQ and ACNET Controls

DAQ computer comprises of a VAX3100 station which communicates with the CAMAC crate filled with ADC, TDC and blind scalers. Each channel from every event is read out using a standard CAMAC software library provided FORTRAN like subroutine calls from a home-made DAQ program and stored as binary files. Routines to decode these files and analyse the data are written independent of the collection procedure. Simple online displays were done to monitor the high-voltages

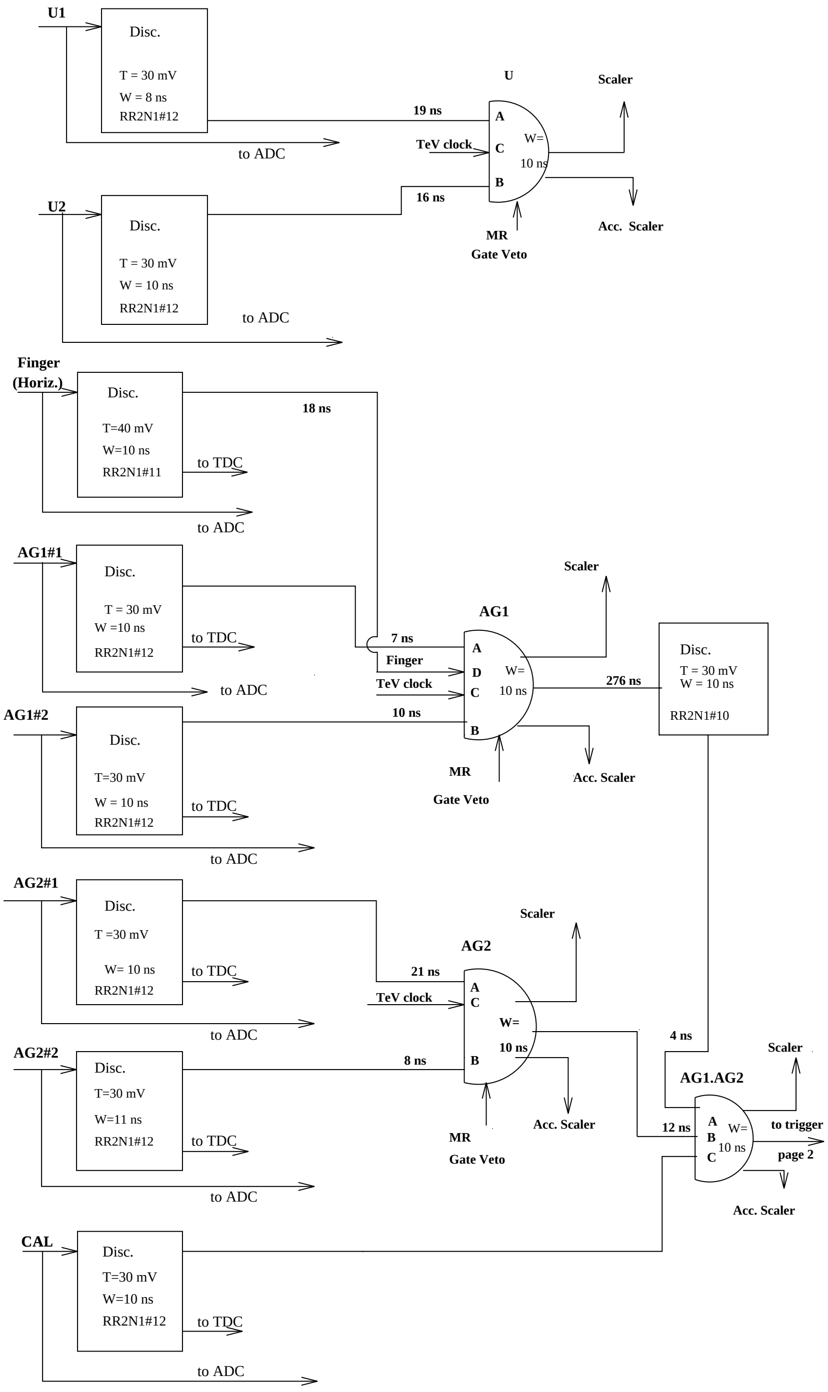

Figure 3.3: Shown here are all the raw signals from the various counters that are discriminated and the coincidences that are made for the interaction counters (U) and air gap counters (AG1 & AG2). The coincidence rates are also fed into the ACNET scalers and the DAQ scaler which then gets written out to disk. All of the above logic units were housed in NIM crates in the counting room.

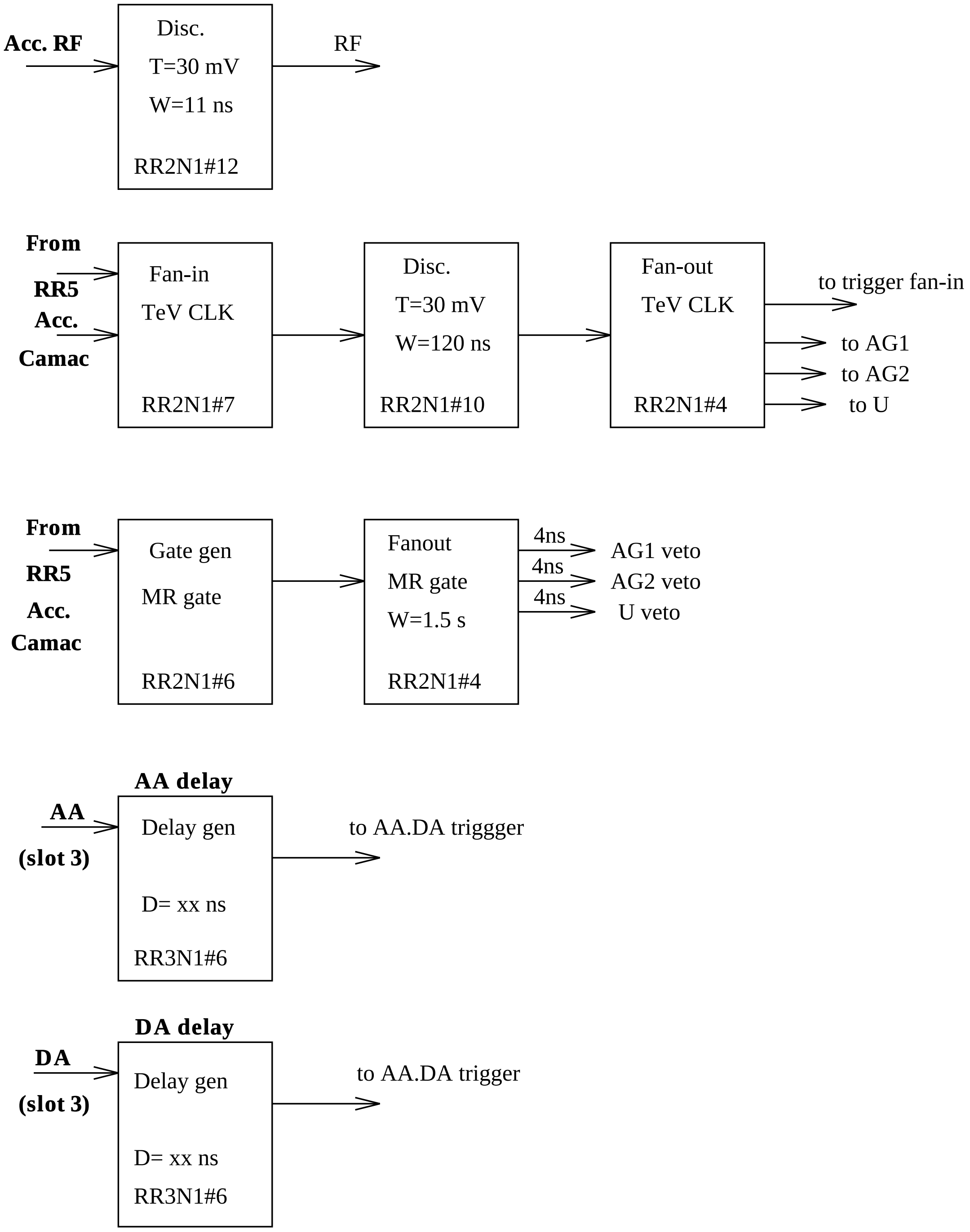

Figure 3.4: Shown here are the various signals we used from the ACNET camac crate. The RF signal, the Tevatron clock and the Main Ring signals are used as part of the trigger definition. Tev clock is also in the definition of counter coincidences. The DA trigger was used in the kick mode studies.

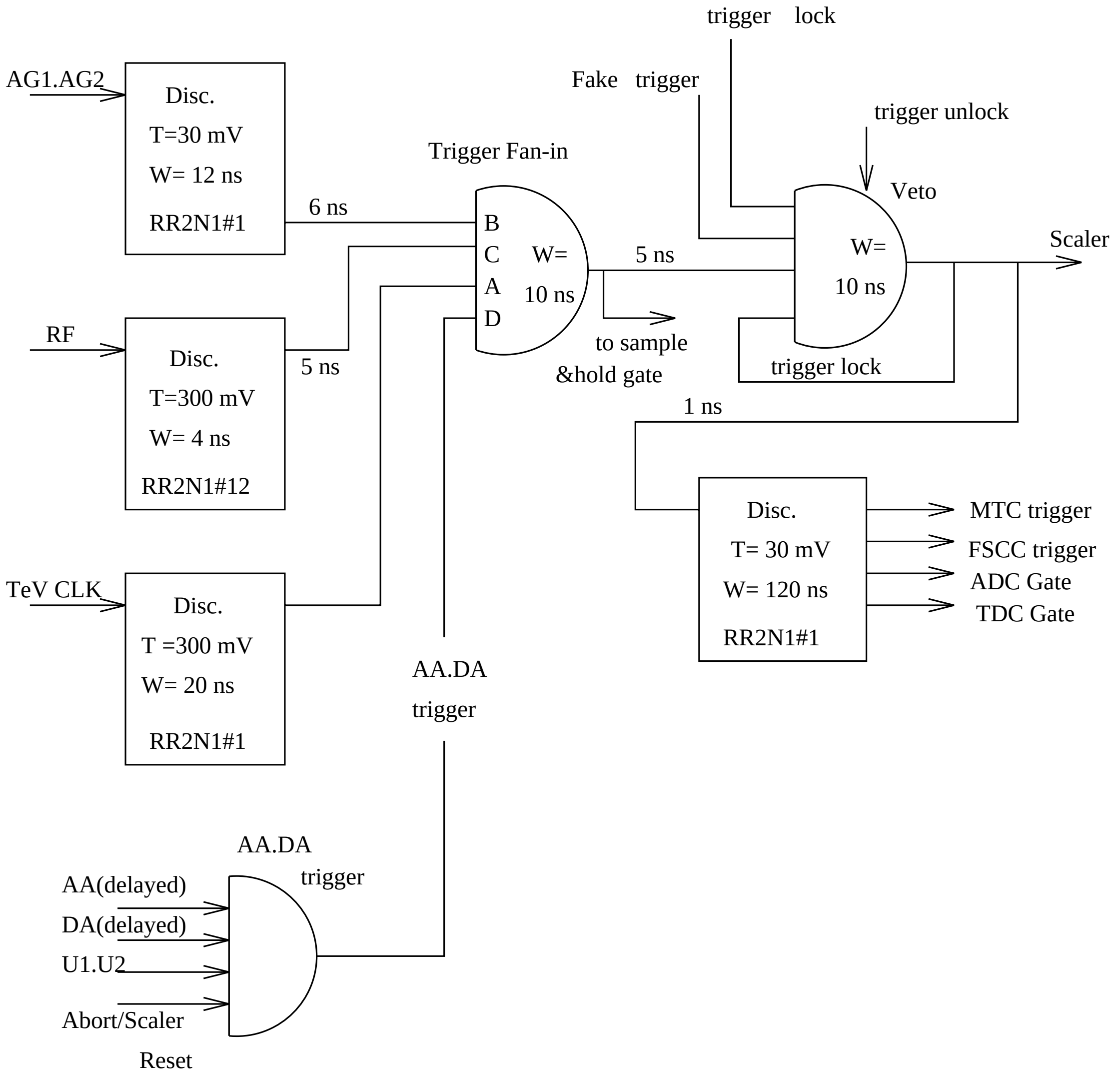

Figure 3.5: This diagram gives a detailed view of our trigger definition. The setup was flexible so as to switch between kick mode and diffusion mode data runs. The trigger is passed on to the scalers as well as to the silicon detector readout system (MTC & FSCC triggers) and the ADC and TDC gates for kick mode studies.

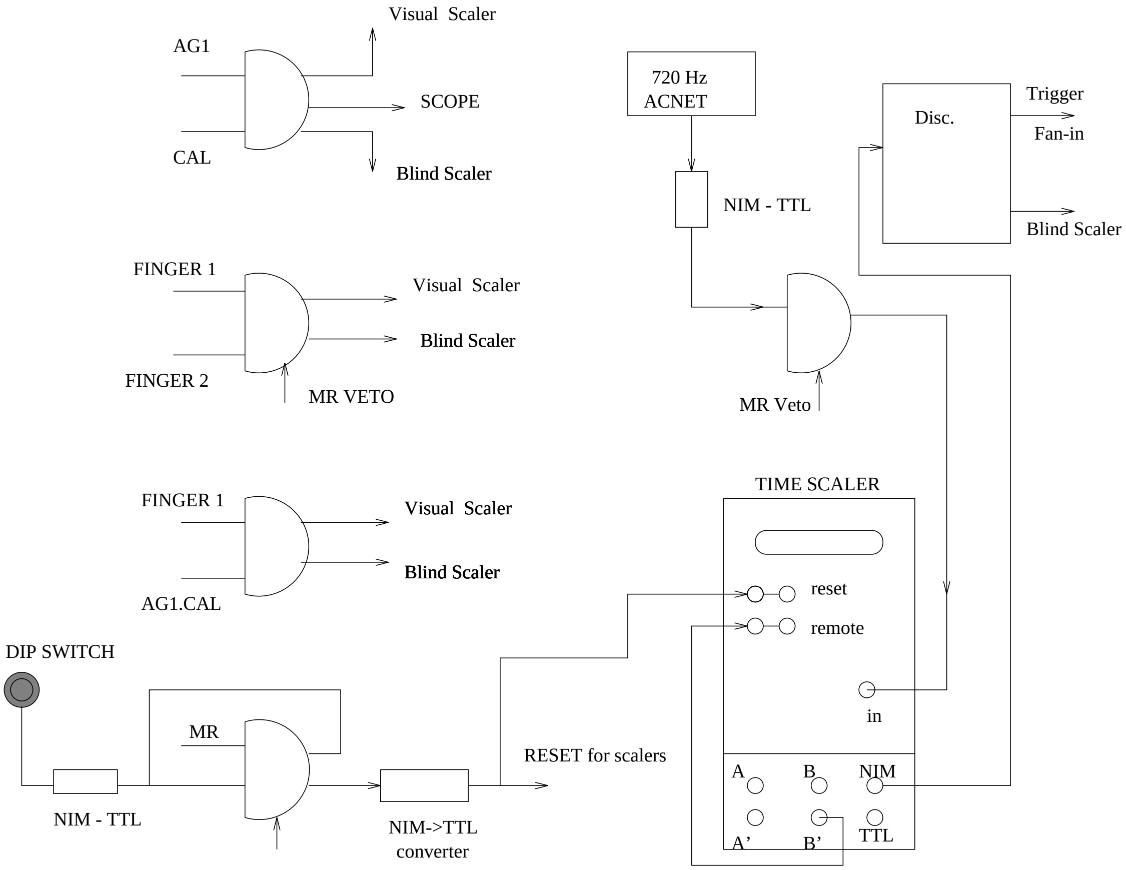

Figure 3.6: Shown here is the setup used during diffusion mode studies. The ACNET 720 Hz clock is used to time a 5 sec livetime for the scaler gates to be open. The TIME SCALER shown also generates the trigger which is fed into the general fan-in described earlier. The reset and start is run manually using the dip switch. The Main ring veto is also built into the definition for the livetime for the gate.

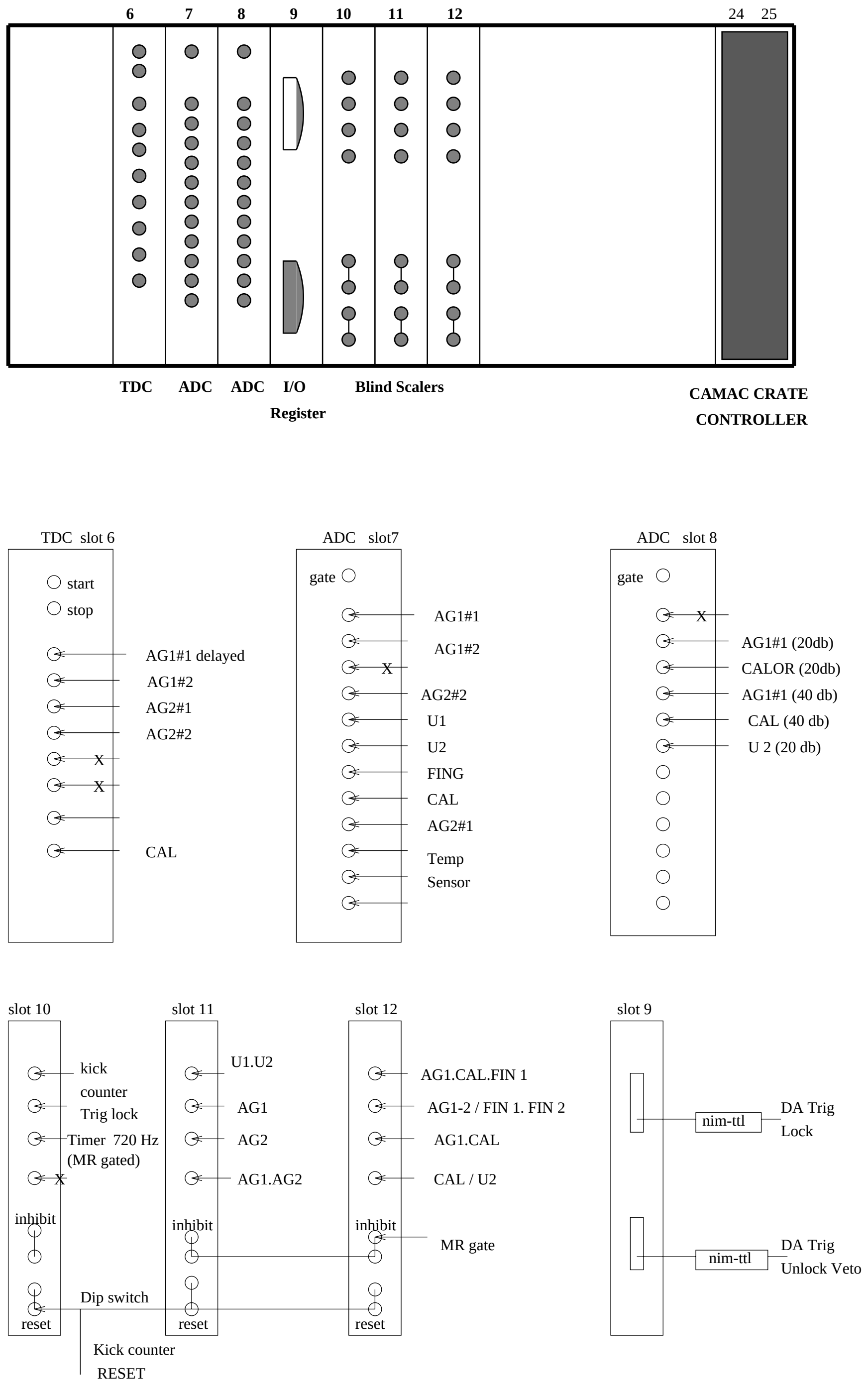

Figure 3.7: The camac crate configuration used by the DAQ is shown here. The various ADC, TDC and SCALER signals are read out to the DEC workstation which ran the DAQ software. Specially built cards in slots 1 & 2 (not shown here) were used to execute the readout.

on the counters, and it also printed on screen the ADC and SCALER values of the individual counters.

Use of ACNET was mainly as a control tool for the movement of the various stages on which the counters were mounted and to align the crystal by using the four degrees of freedom of the meter-long goniometer. It was also useful to monitor the loss rates at the air gap counters and next to the crystal, and to look for any increased activity at loss monitors located at B0 and D0 due to the insertion of the crystal into the beam halo. This was done by the ACNET utility called 'Fast Time Plots' which plotted the individual counter rates with time on a continual basis, providing an online monitor.

### 3.4.3 Kick Mode

In this mode of operation there are advantages of quick alignment of the crystal for channeling but at the cost of beam degradation at a rate that is not useful for parasitic extraction from the Tevatron. Kick mode was employed in all the initial runs of E853. The basic technique is to move the crystal into a pre-determined horizontal location close to the beam (about $4\sigma_x$ from the beam center). Then we kick the beam a few times so that the beam emittance increases, what we call "growing the beam". At the end of this process the beam has grown to such an extent that any more individual kicks will drive the beam into the crystal surface deep enough that it is away from the surface irregularities of the crystal edge which can be of the order of a few microns. The surface of the crystal has the same effect as that of the electrostatic septa wires, scattering the beam or interacting with it as the beam encounters an amorphous layer instead of the symmetry planes.

To get the vertical and horizontal beam profiles we use the flying wires before and after beam growth. Also once you know the beam emittances at a given location it is trivial to calculate the beam divergences knowing all the relevant lattice Twiss functions. To get an idea of the beam lost one monitors the IBEAMS counter on ACNET which gives a time average of the number of circulating protons in the Tevatron. The time averaging is done over many Tevatron turns.

For this mode the ADC readings for the various counters are the only information of importance. The DAQ is designed to read out the ADC value for only the second turn of the proton bunch around the ring after the beam is kicked. The first turn is not read out as the beam is on the far-side away from the crystal face due to the betatron motion in the ring and has not yet interacted with the crystal to produce any useful information. This feature is also predicted by the simulation results, and a comparison with data will be made in the chapter on data analysis and results. The CCD camera plays an important role in the kick mode as it is now sensitive to the beam flux, but usually gets saturated making a calibrated reading off the Frame-Grabber difficult. The SWICS are another useful device to get information about the beam profile and intensity distribution in this mode.

### 3.4.4 Diffusion Mode

Once the crystal has been aligned with respect to the beam for channeling to occur, the crystal is slowly moved into the tail of the beam halo. In this method the beam lifetime should not be seriously affected for parasitic crystal extraction with the Tevatron running in the collider mode.

In the diffusion mode extraction happens over a long time scale, of thousands of turns, compared to the kick mode. Most of the beam which does not channel undergoes multiple scattering and gets another chance to enter the crystal on successive turns. The most effective instrumentation for beam measurement in this mode are the scintillation counters set at voltage levels for single-particle identification. These values are obtained from plateau curves obtained with measurement from cosmic rays as well as data taken for beam-gas interactions that travel down the C0 abort line and trigger the counters.

We also were able to introduce an RF noise using the horizontal damper located at F11 during one of our sessions. This decreased our beam lifetime by a factor of 4 but lasted long enough as it was comparable to our study session period. Higher extraction rates were observed with noise on. It is to be noted that in the diffusion mode tools like the CCD camera and SWICS were not of much use as the extraction rates were well below their sensitivity.

# Chapter 4

# Simulation

## 4.1 Introduction

For a better understanding of the performance of the experiment as well as from the need to explore ideas for halo generation it is imperative that we have a reliable simulation that is representative of the experimental setup. The simulation [2] needs to cover all of the accelerator physics issues involved as well as fundamental physics processes that are charateristic of interactions of the proton beam with the silicon crystal. The former can be well represented in the form of Twiss functions and matrix transformations for particle transport between any given two locations of the Tevatron lattice. The latter however remains largely an open issue as to how exactly one may treat beam crystal interactions within approximations that are consistent with results that one can measure. Here, the major issues are that of the treatment of multiple scattering, channeling and beam loss due to inelastic nuclear collisions.

## 4.2 Beam

To model the beam efficiently we chose an annular distribution of the beam in $x$-$x'$ space. The reason for doing so is that the beam core is hardly disturbed at all. The initial collection of $80,000$ particles is populated as a gaussian distribution in this region with a sigma of $0.56mm$ (this is the same as the $\sigma_x$ for the beam during low intensity proton only stores). A simulation run with the crystal placed at its nominal position along the horizontal x-direction and a normally distributed beam transported around the Tevatron lattice yielded results which indicate that particles that lie outside of the ellipse defined by $x_2^{max} > x_{crystal}$ are scraped off by the crytal edge after 100 turns. This time scale is typical of the time involved between the positioning of the crystal close to the tail of the beam and start of a data taking session marked by the application of a kick to the beam to introduce a reasonable step-size into the crystal. Also, assuming a centroid shift of $0.5mm$ at the most one can see that the core of the beam within an ellipse defined by $x_1^{max}$, such that the difference of $x_{crystal}$ and $x_1^{max}$ is less than the centroid shift resulting from the kick guarantees that the core will not come in contact with the crystal. Hence, retaining only the annular region of the gaussian distribution defined by $x_1^{max}$ and $x_2^{max}$ ellipses is a valid procedure to reduce computing without adversely affecting the physics.

One needs to be careful in choosing the beam phase-space distribution in $x$, $x'$ that matches the Tevatron lattice in order to avoid emittance blowup due to mismatch. The general equation of the ellipse in terms of the lattice twiss functions $\alpha$, $\beta$ and $\gamma$ is given by,

$$\gamma x^2 + 2\alpha x x' + \beta x'^2 = \epsilon \tag{4.1}$$

The bi-gaussian distribution in $x$, $x^{'}$ space generated initially is not one that matches the tevatron lattice as given by the equation above. It corresponds to the case where $\alpha$ is zero reducing the above relation to the form given below where we use $\beta^{*}$ to denote the value of $\beta$ characteristic of the initial distribution.

$$\gamma x^{2} + \beta^{*} x^{'2} = \epsilon \tag{4.2}$$

where $\beta^{*}$ in terms of the lattice twiss fuctions is given by,

$$\beta^{*} = \beta cos^{2}\phi + \gamma sin^{2}\phi + 2\alpha sin\phi cos\phi \tag{4.3}$$

$$tan2\phi = \frac{2\alpha}{\beta - \gamma} \tag{4.4}$$

Hence, this distribution has to be rotated by the amount $\phi$ to get the right orientation of the matched distribution in phase-space.

### 4.2.1 Crystal

The interaction of the crystal with the beam is modeled as follows. Given the $x$, $x^{'}$ at the crystal face and the crystal geometry one can easily estimate the effective length of the beam trajectory within the crystal. This is used in calculating the probability for the incident particle to undergo inelastic nuclear interaction and also for calculating the effects of multiple scattering.

Each particle arriving at the crystal location is represented be a point in the transverse phase-space (four coordinates). First, we select an ensemble of particles interacting with the crystal, simply by applying obvious geometric criterion $x > x_{crystal}$ for the particle to meet the horizontal dimension of the crystal. Then a channeling criterion is applied to the interacting ensemble – all particles with $y^{'} < \theta_{crit}$, 'successfully' enter a crystal channel. We assume no dechanneling effects, therefore all those particles are assumed to channel through the entire length of the crystal and finally to be extracted from the beam – in our simulation they are removed from the distribution and further tracking.

All remaining particles traverse the bulk of the crystal (without being channeled), therefore they interact with an amorphous material rather than a crystal. Knowing the phase-space coordinates $x$, $x^{'}$ of a given particle at the crystal face and the crystal geometry one can easily calculate the the effective length of the beam trajectory within the crystal $l$ as follows.

$$l = \begin{cases} \frac{(x_{cryst}-x)}{sin\ x^{'}} & x^{'} < a \\ \\ \frac{L}{cos\ x^{'}} & x < b \\ \\ \frac{(X-x)}{sin\ x^{'}} & x > b \end{cases}$$

$$\begin{aligned} a &= -tan^{-1}(\frac{x - x_{cryst}}{L}) \\ b &= tan^{-1}(\frac{X-x}{L}) \end{aligned} \tag{4.5}$$

This is used to calculate the probability for the incident particle to undergo inelastic nuclear interaction given by the following distribution

$$P(l) = 1 - e^{-l/\lambda_T}. \tag{4.6}$$

where $\lambda_T$ is the nuclear collision length. Using this distribution, one can select a fraction of the initial ensemble (interacting with the crystal) to undergo wide angle nuclear scattering. In our simulation these particles are considered to have moved outside the angular apperture of the machine – they are removed from the ensemble and they are no longer being tracked by the simulation.

Now, all remaining particles in the ensemble undergo multiple scattering traversing the crystal. This interaction is implemented in our simulation by adding an angular deflection (in $x$ and $y$ plane) to the the original phase-space coordinate of each particle of the interacting ensemble. Those angular kicks are generated according to the Gaussian distribution, where the sigmas are given by the following expression

$$\sigma_x = \frac{13.6MeV}{\beta cp}\sqrt{\frac{l}{X_0}}[1 + 0.038\ln(\frac{l}{X_0})] \tag{4.7}$$

Finally, the resulting phase-space distribution (leaving the crystal) is 'propagated' through the entire Tevatron ring – it is mapped via the one turn transfer map, $R_1$, which includes the details of beam optics. This closes one loop of our tracking routine.

For completeness crystal properties are listed below in a table.

Table 4.1: Crystal Characteristics

| Crystal | Silicon |
|---|---|
| plane | 1 1 1 |
| Atomic No. | 14 |
| Atomic wt. | 28.09 |
| density | 2.33 $g/cm^2$ |
| dimension | $4cm \times 1cm \times 1cm$ |
| interaction length | 30.3 cm |
| radiation length | 9.36 cm |

## 4.3 Lattice Parameters

The simulation presented here resembles the sequence of events that are done during a data run for experiment E853 in the kick mode. The beam is set at 900 GeV/c. The crystal is positioned in the tail of the beam at 3 mm from the ideal orbit position at the crystal location. The data acquisition system is triggered on a signal that is sent out whenever the beam is kicked by the chosen dipole magnet located at E17. A map of the location of the crystal position and the kicker in the Tevatron is given in Figure 3.1. The matrix $R$ is the transfer matrix for a single turn around the Tevatron and $M$ is the transfer matrix between two locations 1 and 2 in terms of the twiss functions $\alpha$, $\beta$ and $\gamma$ at the locations and the phase difference $\delta\mu$ between the two points of the lattice.

$$R = \begin{pmatrix} cos\mu + \alpha_1 sin\mu & \beta_1 sin\mu \\ -\gamma_1 sin\mu & cos\mu - \alpha_1 sin\mu \end{pmatrix} \tag{4.8}$$

$$M = \begin{pmatrix} \sqrt{\frac{\beta_2}{\beta_1}}(cos\delta\mu + \alpha_1 sin\delta\mu) & \sqrt{\beta_1\beta_2} sin\delta\mu \\ -\frac{(1+\alpha_1\alpha_2) sin\delta\mu + (\alpha_2 - \alpha_1) cos\delta\mu}{\sqrt{\beta_1\beta_2}} & \sqrt{\frac{\beta_1}{\beta_2}}(cos\delta\mu - \alpha_2 sin\delta\mu) \end{pmatrix} \tag{4.9}$$

An up-to-date version of the Tevatron lattice was used to construct the lattice which extended into the extraction beamline. It stretches from the silicon crystal location at B48 through the air gaps AG1 and AG2. Based on the beam optics two 6 × 6 transfer matrices were found (from the crystal to the AG1 and AG2 locations). Finally, the vertical phase space distributions of the extracted beam were found in these locations. Numerical values of the vertical beam sizes and the vertical divergences were calculated in both AG1 and AG2 locations.

### 4.3.1 Extraction Lattice

An up-to-date version of the Tevatron injection lattice was used to calculate initial values of the TWISS functions at the crystal location. The Tevatron lattice was tuned so that the nominal betatron frequencies in the horizontal and vertical planes are $\nu_x = 20.585$ and $\nu_y = 20.574$, respectively.

The extraction lattice includes a sequence of five Tevatron elements downstream from the crystal location starting with a half-length horizontal bend magnet, two full horizontal bends and a doublet of focusing and defocusing quadrupoles. The rest of the CEX beam line is a long drift stretching through the C0 marker and both air gap locations (AG1 and AG2). The location of the crystal, AG1 and AG2 with respect to the C0 marker are given by the following distances: the crystal $= -61.0m$, AG1 $= 19.3m$ and AG2 $= 59.5m$. Values of the horizontal and vertical beta functions along the CEX beamline were obtained from MAD 8.14 calculation [22]. Similarly, the vertical parts of the transfer matrices between the crystal and the air gaps AG1 and AG2 are listed below.

$$M^{(1)} = \begin{pmatrix} 0.1560 & 41.28 \\ -0.02422 & -0.001537 \end{pmatrix} \tag{4.10}$$

$$M^{(2)} = \begin{pmatrix} -0.8177 & 41.34 \\ -0.02422 & -0.001537 \end{pmatrix} \tag{4.11}$$

The transfer map can be written in the following compact form,

$$\underline{y}^{(i)} = M^{(i)}\underline{y}^{(crystal)}, i = 1, 2 \tag{4.12}$$

where,

$$\underline{y} = \begin{pmatrix} y \\ y' \end{pmatrix} \tag{4.13}$$

The twiss functions for the Tevatron lattice calculated using the MAD program are listed below in the table.

Table 4.2: Lattice Twiss functions

| location | $\alpha$ | $\beta$ | $\mu$ |
|---|---|---|---|
| E17 kicker | -2.181 | 109.851 | 7.767 |
| crystal | 0.145 | 104.678 | 20.44 |

### 4.3.2 Extracted Beam Phase-Space

The beam entering the crystal is assumed to have a bi-gaussian distribution in the transverse phase-space $(y, y')$ characterized by the corresponding sigma values

$$\sigma_y = 330 \times 10^{-6} m \tag{4.14}$$

$$\sigma_{y'} = 11 \times 10^{-6} rad \tag{4.15}$$

Using linear transfer matrices described by Equations 4.10, 4.11 one can get the simple transformation rules for $\sigma_y$ and $\sigma_{y'}$

$$\sigma_y^i = \sqrt{\left(M_{11}^{(i)} \sigma_y^{(cryst)}\right)^2 + \left(M_{12}^{(i)} \sigma_{y'}^{(cryst)}\right)^2} \tag{4.16}$$

$$\sigma_{y'}^i = \sqrt{\left(M_{21}^{(i)} \sigma_y^{(cryst)}\right)^2 + \left(M_{22}^{(i)} \sigma_{y'}^{(cryst)}\right)^2} \tag{4.17}$$

Evolution of the initial bi-Gaussian distribution governed by the transfer map given by the Equation 4.12 is illustrated in Figures 4.2, 4.3, 4.4. The values of $\sigma_y$ and $\sigma_y^{'}$ transformed according to Equations 4.17 above are collected in the table below.

Table 4.3: Beam parameters

| vertical beam size/divergence<br>(bi-Gaussian distribution) | | |
|---|---|---|
| location | $\sigma_y[m]$ | $\sigma_{y'}[rad]$ |
| crystal | $330 \times 10^{-6}$ | $11.00 \times 10^{-6}$ |
| AG1 | $457 \times 10^{-6}$ | $7.99 \times 10^{-6}$ |
| AG2 | $529 \times 10^{-6}$ | $7.99 \times 10^{-6}$ |

### 4.3.3 Kick Mode

Prior to the crystal extraction process, the beam is perturbed by firing a horizontal kicker at the E17 location. The kicker is located approximately on the opposite side of the ring with respect to the crystal (upstream of the C0 marker). The amount of angular kick of $\Delta x^{'} = 30\mu$radian adds the following off set, $\underline{\Delta x}$ to every phase-space point at E17 location

$$\underline{\Delta x} = \begin{pmatrix} 0 \\ \Delta x^{'} \end{pmatrix} \tag{4.18}$$

For the purpose of particle tracking in our simulation one can mark the following two location of interest: the location of the crystal – labelled by (1) and the location of the E17 kicker labelled by (2). Using this convention one can define turn-by-turn phase-space tracking algorithm for the kick mode in the following compact matrix notation

$$\underline{x}_1^{(n)} = \underline{x}_1^{(0)} + R_1^{n-1} M_{2\rightarrow 1} \underline{\Delta x} \tag{4.19}$$

Here, $n$ is the turn number, $R_1$ is the one-turn transfer matrix (at the crystal location) and $\underline{x}_1^{(0)}$ is the initial phase-space configuration at the crystal location on the turn 'just before firing the kicker'. Above transformation is used for particle tracking in our simulation, where the transfer matrices $R_1$ and $M_{2\rightarrow 1}$ are calculated via Eqs. 4.8, 4.9 using values of the Twiss functions collected in Table 4.2.

## 4.4 Results

This simulation was done to gain a better understanding of the transverse phase-space evolution of the beam under kick mode extraction. To illustrate the combined effect of the transverse kick of the beam with the E17 magnet and its interaction with the silicon crystal located at B48 a snap-shot of the horizontal phase-space is displayed every turn after the beam interacts with the crystal. As was seen in the data the first turn around after the kick, the beam is on the far-side of the phase-space diagram with respect to the crystal resulting in no interaction with the crystal. In the second turn around we see our counter rates for interaction monitor go up as is the case in the simulation. Turns 4, 7 and 9 are the turns that undergo maximum beam-crystal interaction.

It is seen in the simulation that those particles which were not channeled the first time around but suffered multiple scattering arrive at the face of the crystal on a later turn providing for multi-turn extraction which enhances the total extraction efficiency.

An interesting result is illustrated in the snap-shot corresponding to turn number 50. It shows an uneven phase space depletion, which can be explained from beam dynamics considerations [2]. The beam phase-space grows following the kick till it stabilises after many turns. The phase-space also undergoes a rotation every turn which results in the pronounced interaction of the beam with the crystal every other turn. Roughly half of the angular component of the phase-space is exposed to the interaction with the crystal resulting in depletion of the beam.

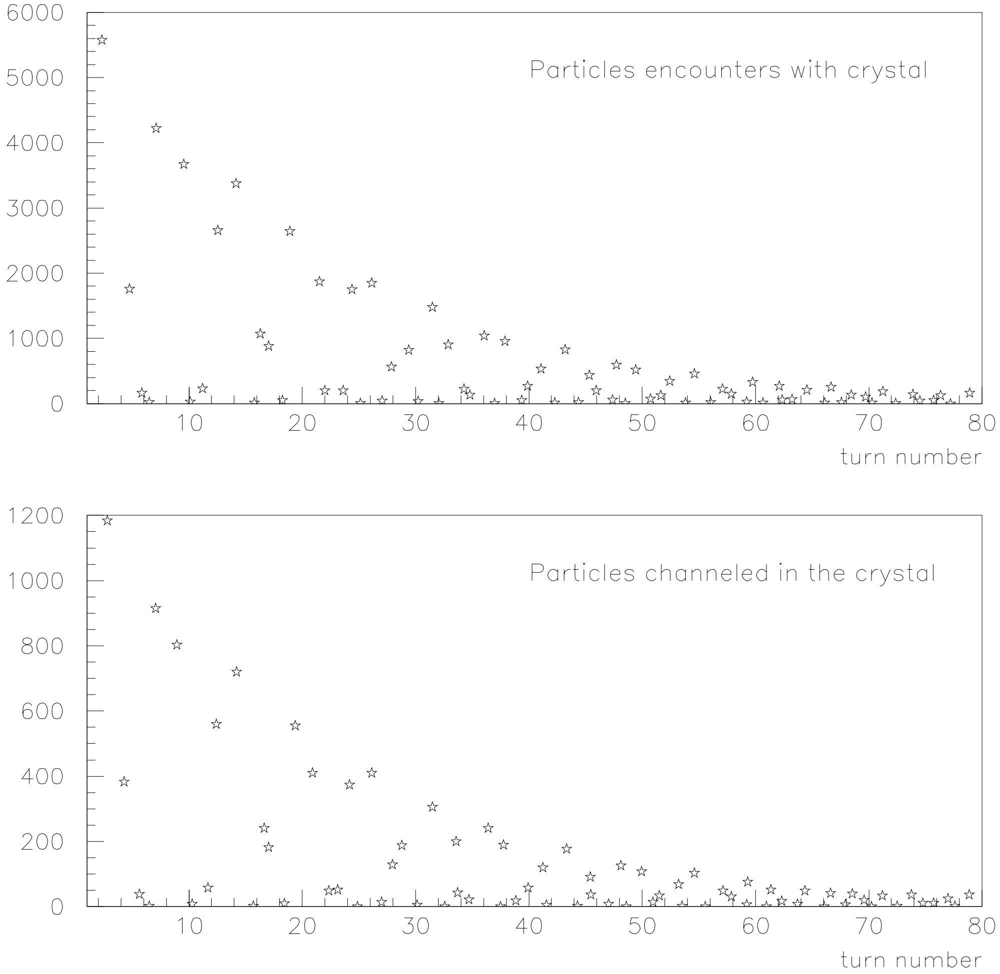

Figure 4.1: Particle count versus turn number.

Figure 4.2: Phase-space distribution for the first 5 turns.

Figure 4.3: Phase-space distribution for turns 6 through 11.

Figure 4.4: Phase-space distribution for turns 12 through 50.

# Chapter 5

# Diffusion Mode Data

## 5.1 Vertical Angle Scan

As the first step towards extraction the crystal has to be aligned in the vertical plane for the incident beam to be within the critical angle of acceptance for channeling. The critical angle for a silicon crystal with the symmetry axis chosen to be (1,1,1) is calculated to be 5 $\mu radian$. This is the half angle, defined by the angle between the center line for the planar channel and the direction of the incident projectile where the cutoff for channeling is expected to happen.

The beam in the Tevatron has a vertical angular divergence of about 11 $\mu radian$ which is comparable to the full angle acceptance for channeling. It is necessary that the crystal be vertically aligned with respect to the beam direction. Hence, for each run we perform a vertical angle scan by sweeping the vertical angle of the goniometer in small steps of 10 $\mu radians$ to find the angle at which extraction is maximized.

The absolute value for the optimum vertical angle for channeling varied from run to run due to the changing beam conditions in the Tevatron. For those runs for which substantial data was taken over the peak region as well as the tails, we have plots of the $\theta_v$ scan data as seen in the counters located at the first air gap approximately 80 meters downstream of the crystal location.

In most runs we were constrained by time considerations to limit to just a single data point for each value in $\theta_v$. Hence, to assign a reasonable error to these data points we rely on fluctuations in the counter rates recorded when multiple data points were taken for a fixed condition such as the $\theta_v$ value, and scale it appropriately to the varying rates for different $\theta_v$ values as a first step. Deviations from this method had to be chosen when no such possibility existed for a given scan or when an attempt to fit the data points resulted in a bad chisquare, indicating a possible underestimation of the errors. Different functional forms were used to fit the data from different runs and they are explained in the caption for each fit.

For most of the runs, if a measure of the fluctuations cannot be inferred from the scan data itself then the error is estimated from data taken under some other stable condition. In cases where the chisquare value is large, the r.m.s. fluctuation is scaled down from what was estimated for the peak rates and this yields an improved chisquare for the fit.

For all the $\theta_v$ scans the rates are as seen in the coincidence of the counters AG1-1 and AG1-2 located at the first air gap. The rates were recorded over a livetime of 5 seconds duration with the Main Ring veto on.

The function used to fit the data if Gaussian is given by,

$$G(N, X_0, \sigma, X) = \frac{N}{\sqrt{2\pi}\sigma} e^{\frac{-(X-X_0)^2}{2\sigma^2}} \tag{5.1}$$

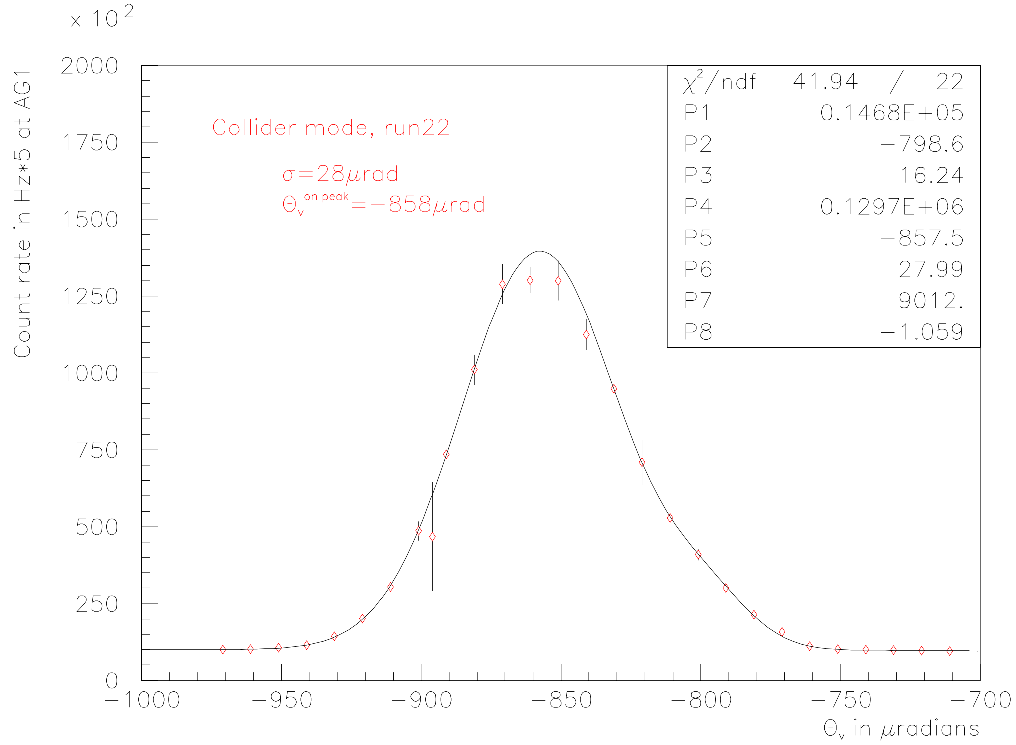

Figure 5.1: The $\theta_v$ scan data is fit to a sum of two gaussians and a polynomial. In this run the peak fits a sum of two gaussians quite well. Errors are estimated for each data point separately yielding a good chisquare for the fit. This was the only run where a broadening of the $\theta_v$ curve was observed for smaller values in the vertical angle (right hand side of the peak).

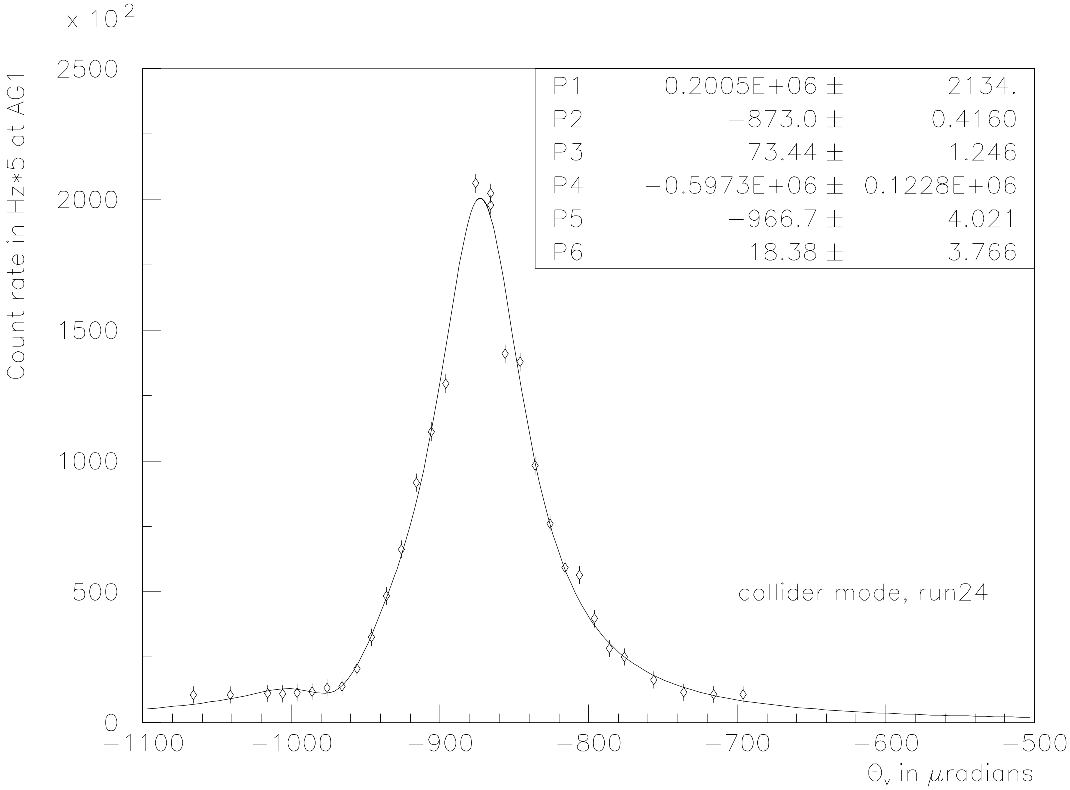

Figure 5.2: The fit is a sum of a Breit-Wigner and Gaussian. The peak fits a Breit-Wigner quite well. The Gaussian helps in fitting the tail on the negative $\theta_v$ side better. The peak is centered at $-873$ $\mu radians$ with a $\sigma = 36.7$ $\mu radians$. All data points are assigned similar errors.

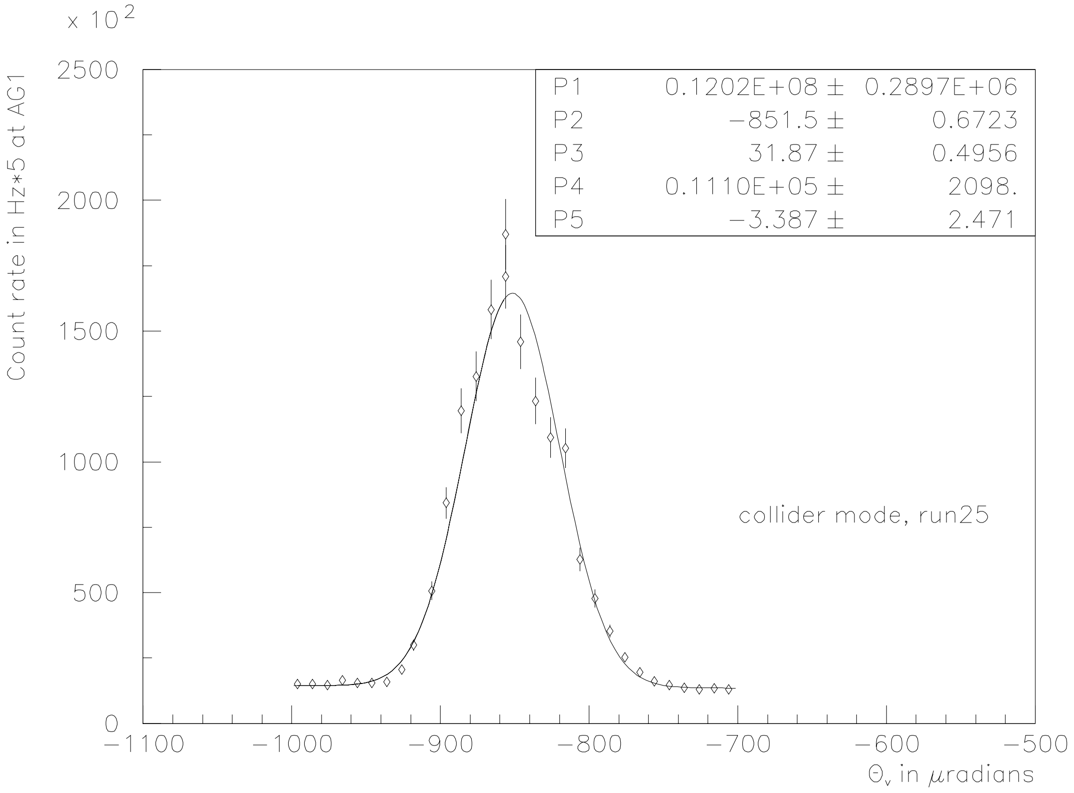

Figure 5.3: The fit is a sum of a Gaussian and a polynomial functional form. The error estimated for the AG1 rates is 7.17% of the coincidence rates added in quadrature to the statistical error. The error was estimated from a region where conditions such as $\theta_v$ were stable.

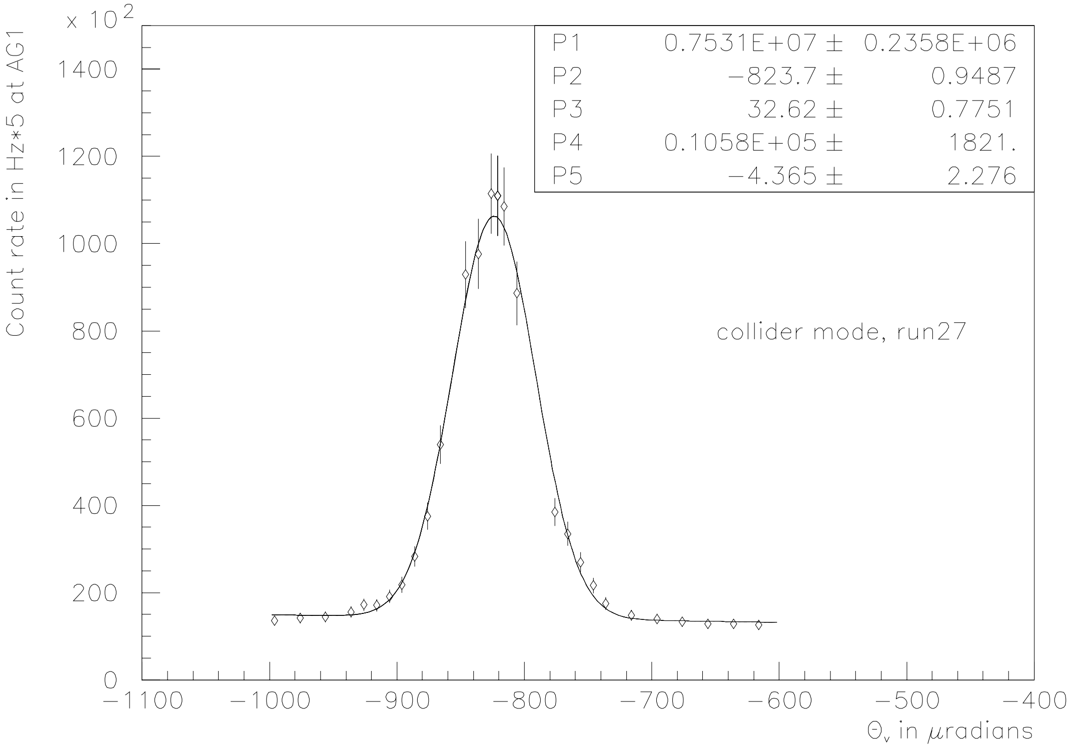

Figure 5.4: The fit is a sum of a Gaussian and a polynomial. The error estimated for the AG1 rates is 8.24% of the coincidence rates added in quadrature to the statistical error. The estimate for the error was done in this case using rates from a constant $\theta_v$ condition outside of scan time.

and in the case of a Breit-Wigner is given by,

$$BW(N, X_0, , X) = N \frac{\frac{\Gamma^2}{4}}{(X - X_0)^2 + \frac{\Gamma^2}{4}} \tag{5.2}$$

As is evident $X_0$ gives the position of the peak in both cases and N is the normalisation for the peak value. , is the full width at half maximum and is roughly equivalent to $2 \times \sigma$ for the case of a Gaussian. The measured widths are summarised along with the distance of the beam centroid from the crystal edge for these runs.

| run no. | $\sigma_{\theta_v}$ | $X - X_{Gon}$ |
|---|---|---|
| 22 | 28 $\mu rad$ | 4800 microns |
| 24 | 36.7 $\mu rad$ | 3500 microns |
| 25 | 31.9 $\mu rad$ | 2950 microns |
| 27 | 32.6 $\mu rad$ | 2050 microns |

Table 5.1: $\theta_v$ widths across runs.

The errors in the width for all of the above runs except in run30 is not more than 2%. The mean value for the beam width in $\theta_v$ has a fairly constant value around 30 $\mu radians$. Note, that the intrinsic beam divergence in the Tevatron is 11.5 $\mu radians$. In the diffusion mode channeling occurs over many turns. Those paricles that are not within the acceptance angle for channeling will suffer multiple scattering and can be extracted during their next encounter with the crystal. This multiple scattering has the effect of increasing the $\sigma_{y'}$ value for the beam (growing the beam). Biryukov [13] quotes this value to be approximately 30 $\mu$rad from his simulation for the E853 case.

## 5.2 Beam profile/Finger scan

It is interesting to study the beam profile after extraction by the crystal for different run conditions. The extracted beam shape is affected by the limited acceptance for channeling in one projection (which happens to be in the y direction in our case) and the optics between the extraction point and the location of the Finger counter. It has a point to parallel focus in the vertical plane. Figures are included for the Y-finger (counter width of 1/32 in) scans performed for various runs.

To make a realistic estimate for the errors in absence of multiple data points we use the r.m.s. fluctuation as seen in the AG1 coincidence rates as a measure of the scatter due to the incident beam fluctuations. We use the ratio of this scatter to the average value of AG1 under stable conditions to scale down the error to the value for the rates recorded with the Y-finger counter in coincidence with AG1.

For those cases where we took multiple data points at each position of the Y-finger counter we have a more exact estimate for the error and did not involve the technique mentioned above.

The data were then fit for most of the runs with a Breit-Wigner form over a constant background and in the case of run 28, a product of a Breit-Wigner and a Gaussian shape was used. Run18 was a proton only store. Before taking data in the diffusion mode we had operated under kick mode conditions. Hence, the beam emittance had grown to almost three times the normal value. Due to the nature of the optics in the extraction line, as discussed earlier this change in $\sigma_{y'}$ for the beam gets translated to a larger $\sigma_y$ for the extracted beam at the air gaps.

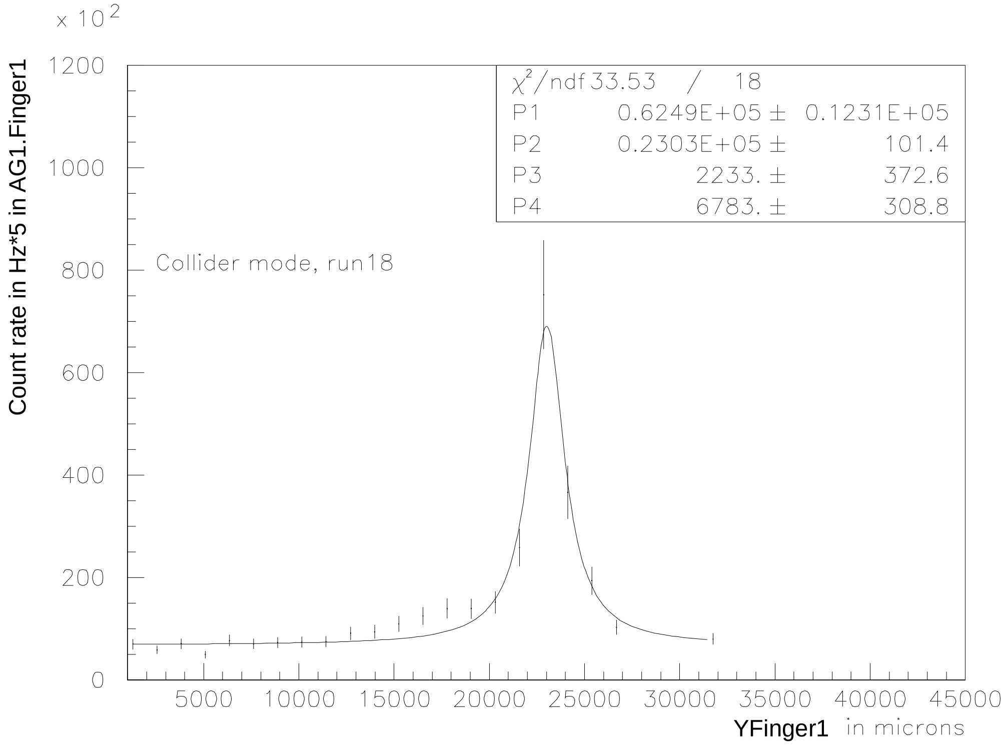

Figure 5.5: The fit is of a Breit-Wigner over a constant. The errors were estimated to be 14.15 % from the AG1 rates with the crystal parked at $X_{gon} = -250$ *microns* and the $\theta_v$ angle set at $-920$ $\mu$*radians* and were then scaled down appropriately for lower values of AG1.finger1. The shoulder on the left side of the curve which corresponds to smaller values of the $Y_{fing1}$ position shows a local rise which is the effect of the tail in the extracted beam due to partial channeling, as these particles see a smaller effective bend due to the crystal.

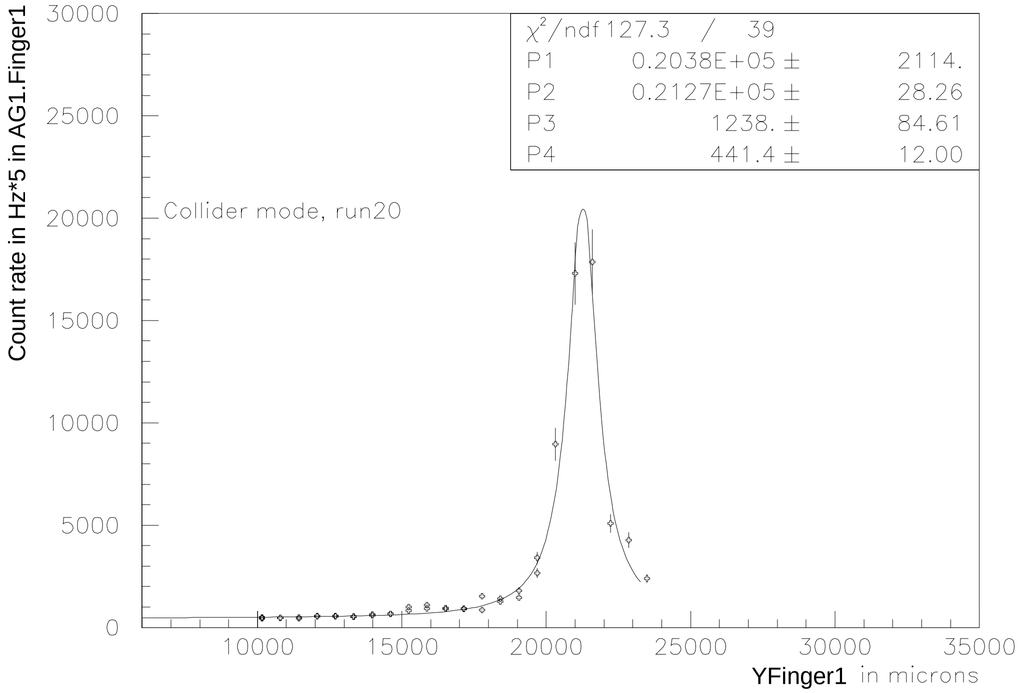

Figure 5.6: The error is estimated at 8.85 % at the peak value for $\theta_v = -836$ $\mu radian$ with the $X_{gon}$ set at 1700 microns. The fit is again a Breit-Wigner over a constant. The tail is less visible in this data compared with the previous run and the beam is 55% narrower than in run18.

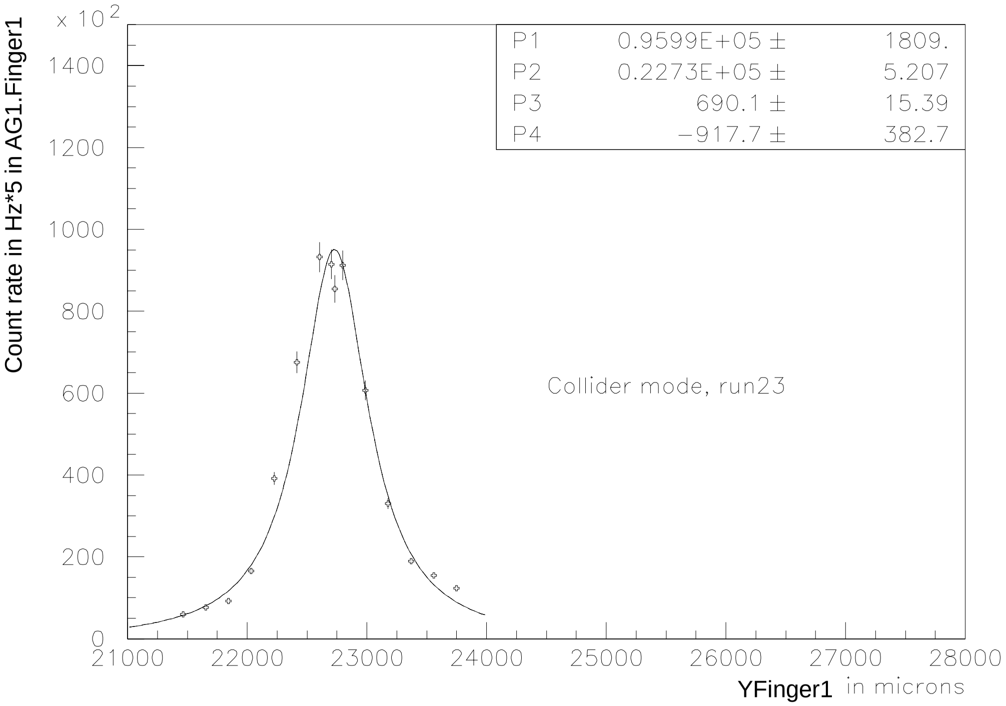

Figure 5.7: The fit is a Breit-Wigner and a constant. The error is estimated from the fluctuation seen at peak value in $\theta_v = -841$ $\mu radian$ with $X_{gon}$ @ -2500 microns. The error was estimated as 3.94 %.

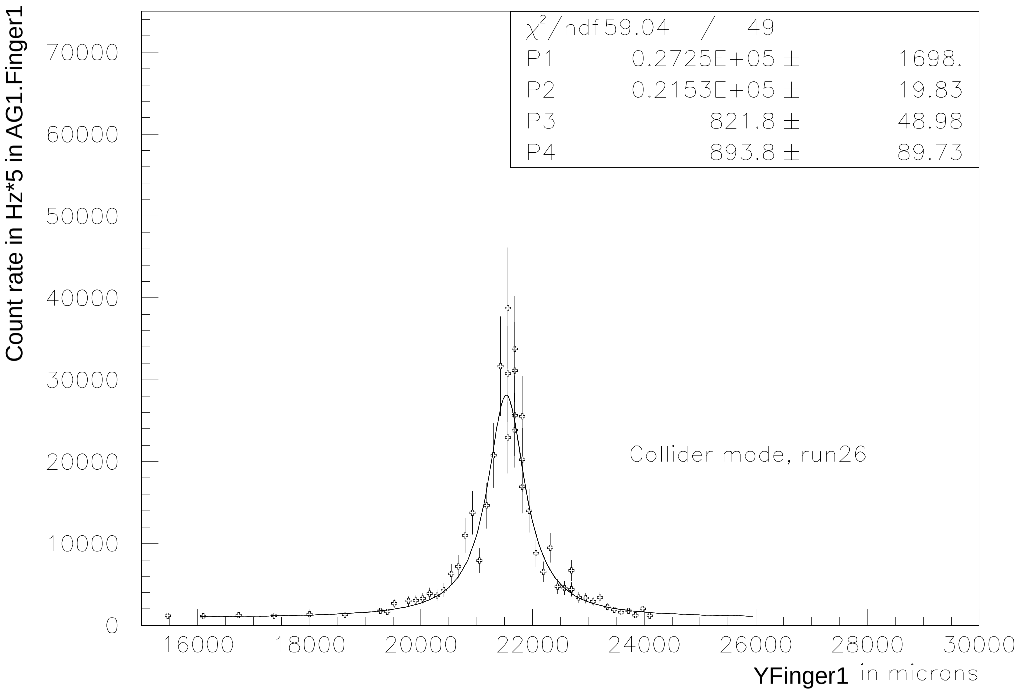

Figure 5.8: The fit is a Breit-Wigner and a constant. The error is estimated at 19.1 % for this run. Data from the on peak value at $-866$ *μradian* yielded a 6.74% error which gives a larger chisquare per degree of freedom for the fit. This reflects the fact the error was being underestimated.

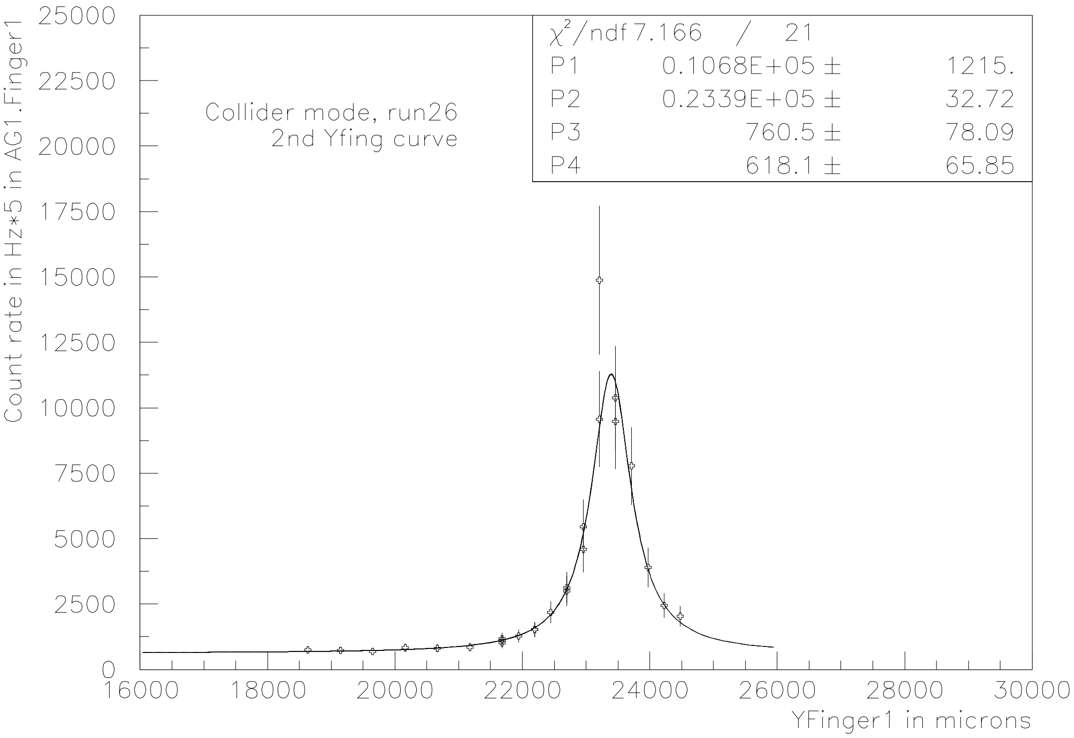

Figure 5.9: After a visual inspection, some of the data points were found to have been wrongly assigned $Y_{Fing1}$ values making the data impossible to fit to a single curve. After taking care of this systematic error by removing the data points which correspond to this region the fit yields a reasonable chisquare and beam width consistent with that from data from the same run. See previous plot. The error here is the same as in the case before at 19.1 %.

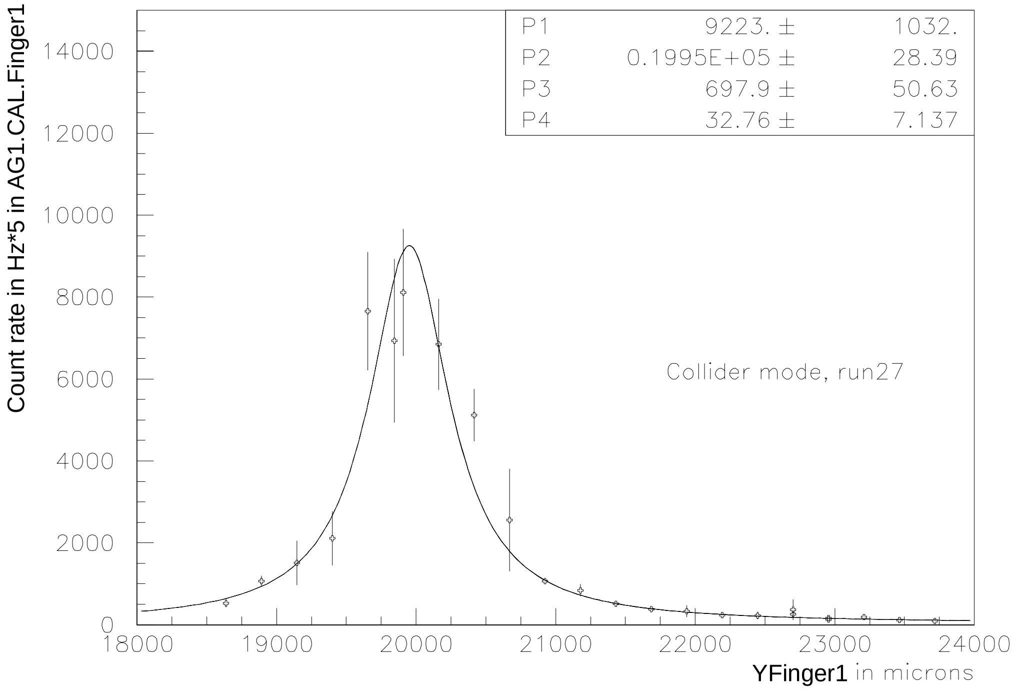

Figure 5.10: In this run we used a triple coincidence containing the Finger1 and the CAL counter which was located in the second air gap. The fit has the same functional form as for the previous runs. We use the fluctuation seen in the above coincidence for each $Y_{fing1}$ position to assign errors.

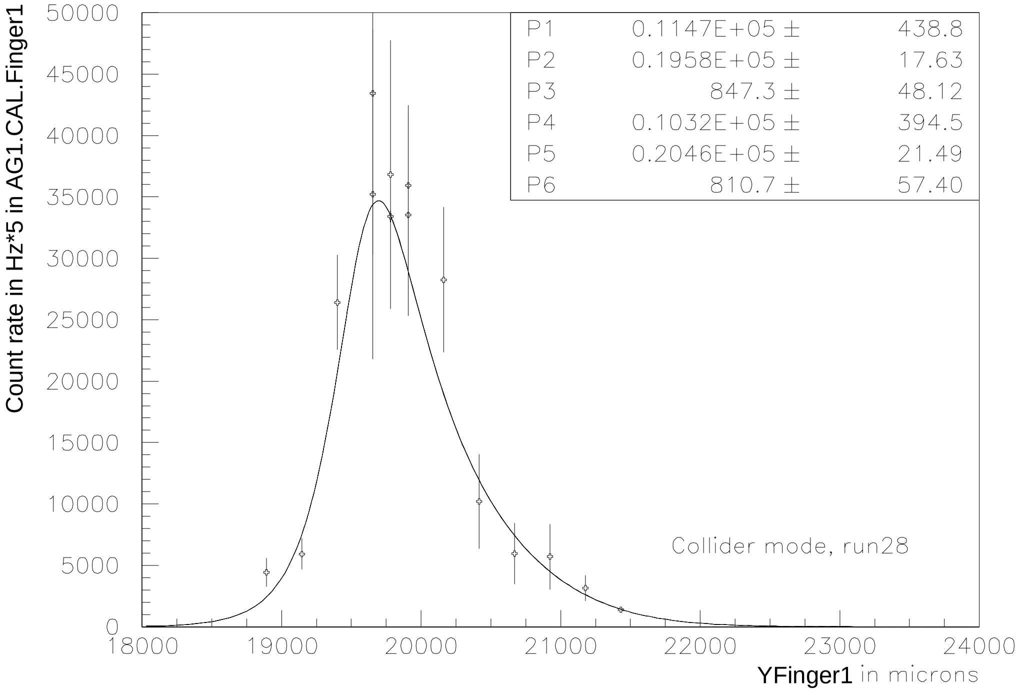

Figure 5.11: In this run multiple data points were taken for each $Y_{fing1}$ value and the errors were assigned from the fluctuation seen for the triple coincidence rates. The fit here is a product of a Breit-Wigner with a Gaussian function. The lack of data points on the lower edge of the $Y_{gon}$ curve results in the asymmetry in the shape.

| run no. | $\sigma_{Y fing}$ in mm | $\sigma_Y^{beam}$ (after correction) | $X - X_{Gon}$ |
|---|---|---|---|
| 18 | $2.233 \pm 0.373$ | $2.221 \pm .373$ | $-250\ \mu m$ |
| 20 | $1.238 \pm 0.085$ | $1.217 \pm 0.085$ | $-1700\ \mu m$ |
| 23 | $0.690 \pm 0.015$ | $0.651 \pm 0.015$ | $-2500\ \mu m$ |
| 26-1 | $0.822 \pm 0.049$ | $0.789 \pm 0.049$ | $-2550\ \mu m$ |
| 26-2 | $0.761 \pm 0.078$ | $0.725 \pm 0.078$ | $-2550\ \mu m$ |
| 27 | $0.698 \pm 0.051$ | $0.659 \pm 0.051$ | $-2050\ \mu m$ |
| 28 | $0.847 \pm 0.048$ | $0.815 \pm 0.048$ | $-3400\ \mu m$ |

Table 5.2: Vertical beam widths across runs.

Another effect that needs to be folded out of the beam widths in y, is the finite width of the Finger1 counter. The smearing due to this finite width is given by $\sigma_{Finger1} = width/\sqrt{12}$ which in the case of the Finger1 is 229 microns. The optics between the crystal and the air gap corresponds to a point-to-parallel geometry. Using the fact that a 640$\mu$radian angle at the crystal translates to a 2.54 cm displacement in the vertical plane, we can estimate the corresponding displacement for an angle of 5$\mu$radian which corresponds to the critical angle. The beam width at the first air gap should be around 0.2mm. Run 18 and 20 the alignment of the Finger1 counter was in progress. In the case of the other runs we are still off by a factor of 3 at least from the expected value. The singular explanation for this is a misalignment of the counter. Any rotation about the length of the counter changes the effective width exposed to the beam by a significant amount as the thickness of the counter is 1/4 inch compared to the width, which is only 1/32 inch.

## 5.3 Channeling Efficiency

### 5.3.1 On-off Peak Analysis

One way to measure the channeling efficiency is to use the inelastic interaction counters (henceforth to be called *U* counters) situated half a meter downstream of the crystal position. These counters measure the interaction rate of the beam with the crystal. When the crystal is aligned perfectly we expect the interaction rate to drop as most particles now do get channeled in the crystal. From the observed dip in the coincidence rates of the two *U* counters, with the crystal perfectly aligned with respect to the beam, we can estimate the channeling efficiency. Data was taken for various values of off-peak and on-peak (where peak refers to the peak of the $\theta_v$ curve) positions during the last three runs. The off-peak data was taken on either side of the on-peak value to take care of the asymmetry in the tail of the *U* curve. A weighted average of the separate off-peak positions is used in the measurement of the dip for each setting.

The off-peak *U* counter rates are from nuclear interaction of the proton beam with the silicon crystal. When the crystal is aligned to the beam the *U* rates should drop because a fraction of the protons which hit the crystal face channel. The ratio of this change in loss rates to the loss rate when the crystal is completely misaligned gives a measure of an upper limit on our beam extraction efficiency due to channeling. It is an upper limit for the extraction effficiency as not all of the particles that enter the channel get bent by the full bend (640 $\mu$rad). Some may exit the crystal before travelling the full length and be lost from the aperture of the machine. The on peak/off peak data was taken many times for each position and the crystal angle was moved quickly from on peak to off peak positions to avoid any long time dependences in the observed rates due to the changing conditions in the Tevatron.

All of the above rates need to be background subtracted. As we move the crystal into the beam halo the large mass of the crystal holder encounters the beam. We see this increase in the count rates with increasing $X_{gon}$ values as we push the crystal closer to the beam during the begining of each run. The background readings for the U-counter is determined by using the rates observed when the crystal is far away from the beam and no measurable beam is being channelled and all run conditions are stable. These data correspond to times when AG1 rates are low. In runs where there was insufficient data to estimate an error on the background values, the error was inferred from data taken later in the run under constant conditions. The error $U_{rms}/\sqrt{N-1}$, where N is the number of points used in the average, is then scaled by the ratio of $U^{later}_{average}/U^{later}_{backgd}$ to get the error on background rates.

The channeling efficiency is determined using background subtracted values for the coincidence rates for U1.U2 during a 5 second time interval:

$$\epsilon^{12}_{dip} = \frac{U^{12}_{off-peak} - U^{12}_{on-peak}}{U^{12}_{off-peak}} \tag{5.3}$$

The associated error is given by,

$$\delta\epsilon_{dip} = \frac{U_{on}}{U_{off}}\sqrt{(\frac{\delta U_{off}}{U_{off}})^2 + (\frac{\delta U_{on}}{U_{on}})^2} \tag{5.4}$$

A summary of the channeling efficiency for the various run conditions is in the table given below.

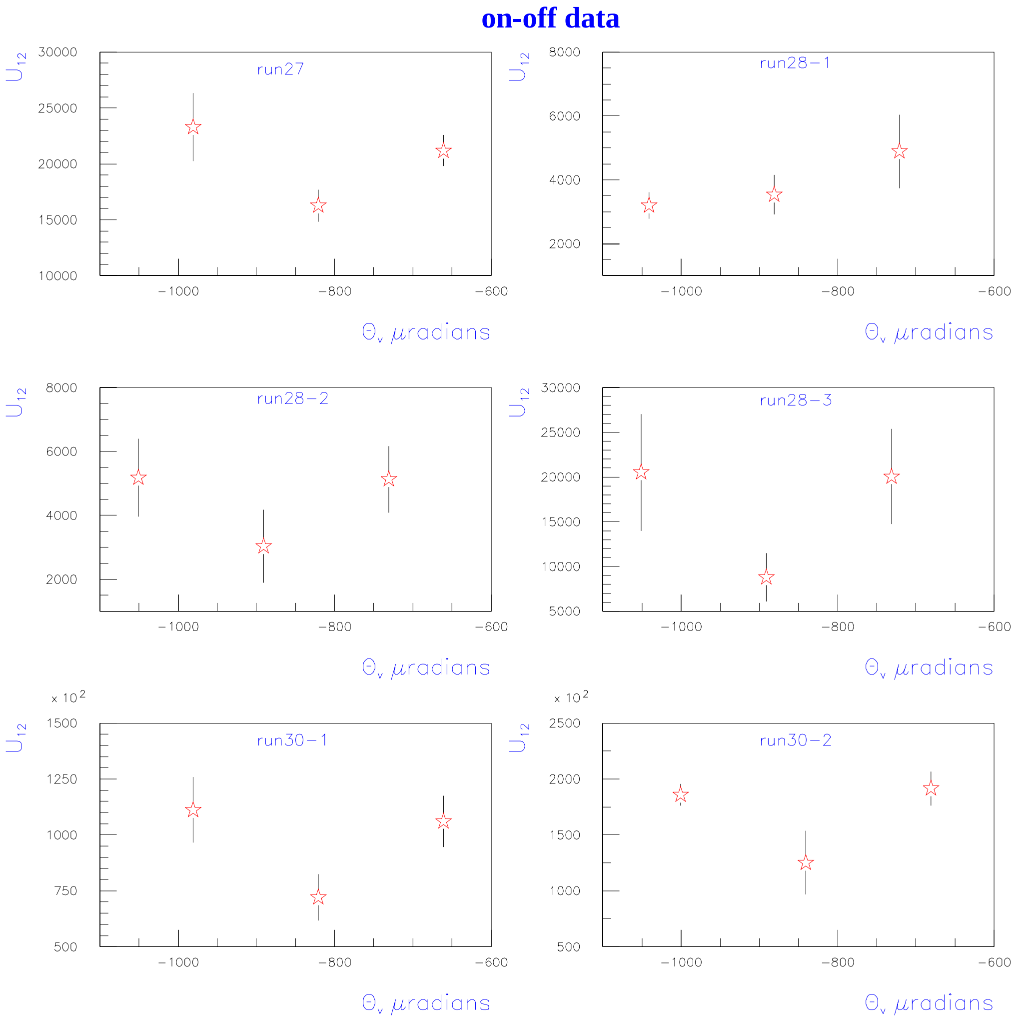

Figure 5.12: U-dip from on-off data taken in runs no. 27, 28 and 30. The vertical axis in each plot corresponds to the coincidence rates recorded over 5 seconds in the U1 and U2 counters. These are background subtracted. The error bars are different from point to point, as the amount of the fluctuation in the incident beam varies with time.

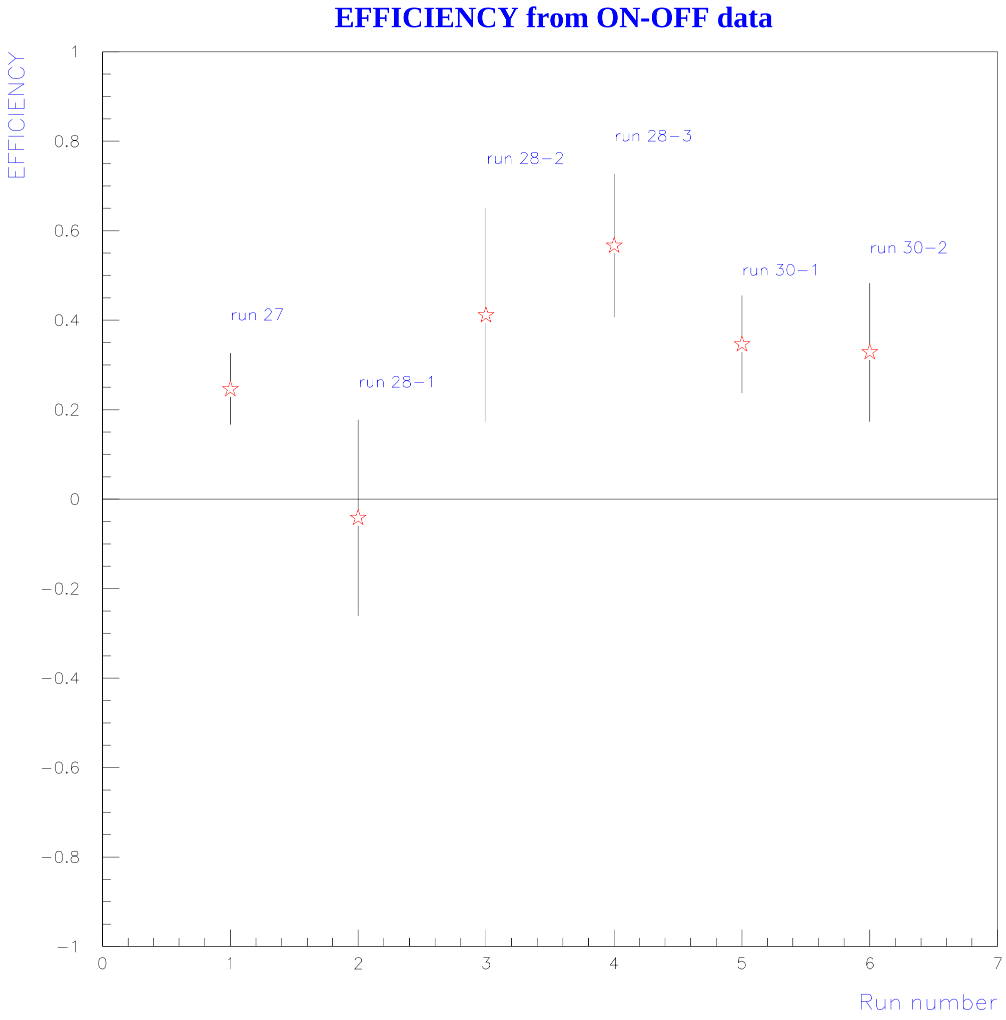

Figure 5.13: Summary of efficiency measured from the background subtracted on peak-off peak rates recorded by the inelastic interaction counter located downstream of the crystal. The large errors are indicative of the incident beam fluctuations.

| run no. | channeling efficiency |
|---|---|
| 27-1 | $0.246 \pm 0.080$ |
| 28-1 | $-0.042 \pm 0.219$ |
| 28-2 | $0.411 \pm 0.239$ |
| 28-3 | $0.567 \pm 0.160$ |
| 30-1 | $0.346 \pm 0.109$ |
| 30-2 | $0.328 \pm 0.155$ |

Table 5.3: channeling efficiency measured using on-off peak data

### 5.3.2 $\Theta_{vert}$ Data

A similar analysis can be done using the counter rates recorded during the $\theta_v$ scans. For this purpose the counters of interest will be the interaction counters U1 and U2 mentioned earlier, and the coincidence rates seen in the air-gap 1 counters. By looking at the shape of the $\theta_v$ curve as seen in the air-gap 1 counters one can select the appropriate regions of the scan to be designated as on-peak data and off-peak data on both sides of the central region. Table 5.4 lists the $\theta_v$ cuts used for different runs to mark the on-peak region and off-peak regions of the scan data. Then an average of the Interaction counter rates in each of these three regions is calculated, to be used in the measurement of the channeling efficiency in the crystal. The formula used is identical to that of the last section on on-off peak data. The error is taken as the $rms/\sqrt{N-1}$ of each of these 3 averages. The off-peak $U$ rate is then the weighted average of the averages taken on the left and right tail of the $U$ distribution.

For those runs where there is insufficient data on one side of the $\theta_v$ peak, we use the data available on that side as a good estimate of the other off-peak region. All the data is background subtracted. The background rates are measured from the conditions when the crystal is parked outside of the 8 mm to 12 mm away from the ideal central orbit location at B48. The background rates are due to the beam interactions with the crystal holder mass as discussed before.

| run no. | $\theta_{left}^{off-peak}$ | $\theta_{left}^{on-peak}$ | $\theta_{right}^{on-peak}$ | $\theta_{right}^{off-peak}$ |
|---|---|---|---|---|
| 16 | -1080 | -990 | -960 | -860 |
| 20 | -890 | -840 | -830 | -800 |
| 22 | -940 | -880 | -850 | -750 |
| 23 | -940 | -870 | -840 | -720 |
| 24 | -970 | -880 | -860 | -760 |
| 25 | -920 | -870 | -850 | -780 |
| 26 | -940 | -880 | -850 | -800 |
| 27 | -920 | -840 | -810 | -750 |
| 28-2 | -975 | -895 | -870 | -825 |
| 30-3 | -960 | -880 | -840 | -730 |

Table 5.4: Table of $\theta_v$ cuts used for different runs. The first and the last columns contain the cut used to mark the tail (off-peak) of the $\theta_v$scan data. The second and third column marks the on-peak region.

| run no. | channeling efficiency |
|---|---|
| 16 | $0.316 \pm 0.202$ |
| 18 | $0.637 \pm 0.155$ |
| 20 | $0.273 \pm 0.288$ |
| 22 | $0.307 \pm 0.075$ |
| 23 | $0.146 \pm 0.099$ |
| 24 | $0.193 \pm 0.186$ |
| 25 | $0.309 \pm 0.166$ |
| 27 | $0.081 \pm 0.456$ |
| 28-2 | $0.069 \pm 0.293$ |
| 30-3 | $0.467 \pm 0.071$ |

Table 5.5: channeling efficiency measured using data taken during the $\theta_v$ scans for various runs

## 5.4 Extraction Efficiency

The extraction efficiency is defined as the fraction of the beam extracted out into the abort line to what was incident on the crystal face. However, this fails since we

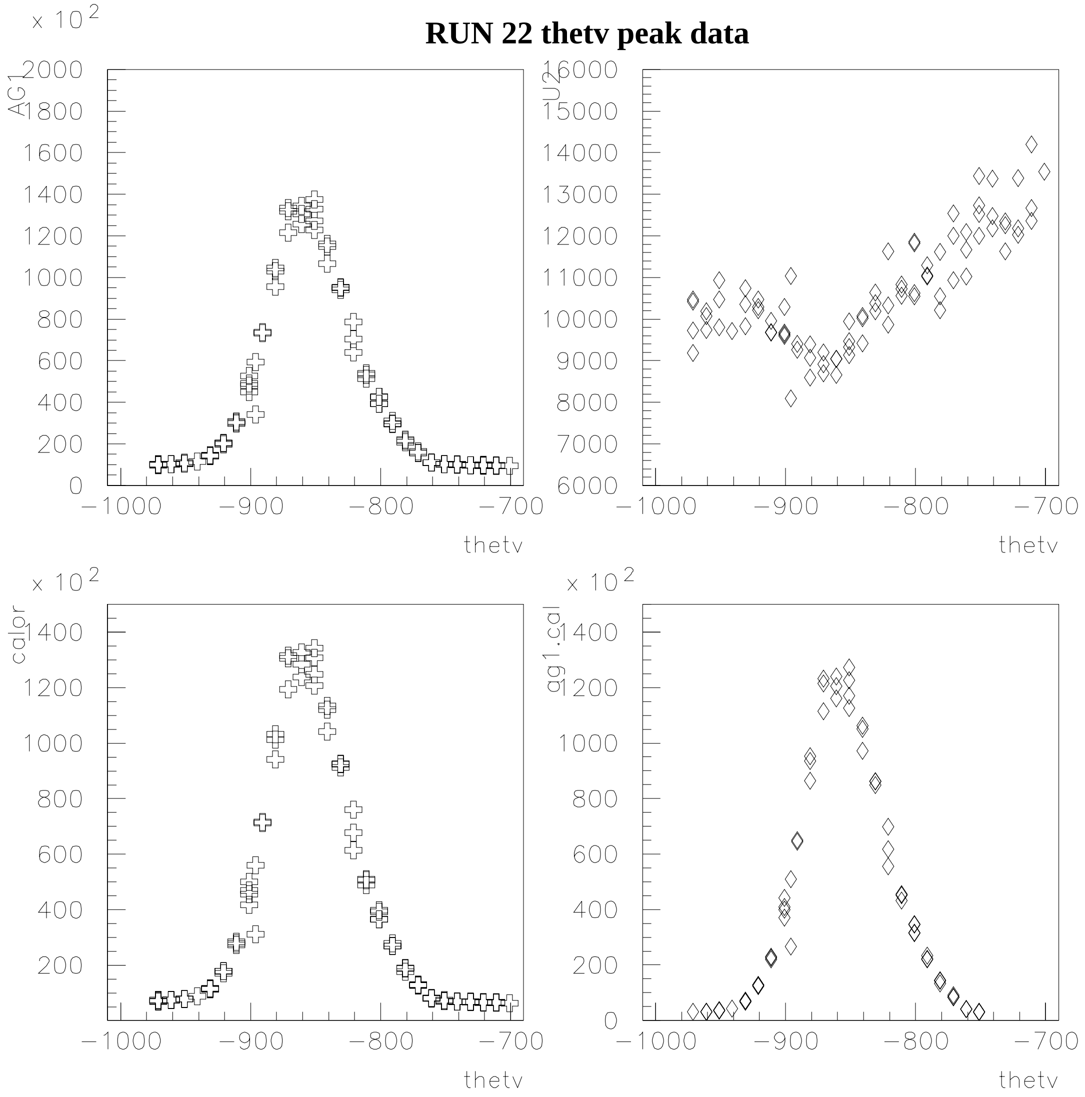

Figure 5.14: run22 scan data; from top clockwise: AG1, U2, CAL, AG1.CAL rates over a 5 second period. The strong correlation between the dip seen in the U2 rates and the peak in the AG1 and CAL counters at the optimal alignment in $\theta_{vert}$ angle is shown. The horizontal axis is in $\mu radians$. The rise in the average rate in U2 with increasing $\theta_{vert}$ values signifies the varying nature of the beam in the Tevatron even within the course of a single run. The time dependent effects are more stronger in the efficiency measured from these data sets than from the on-off peak sample.

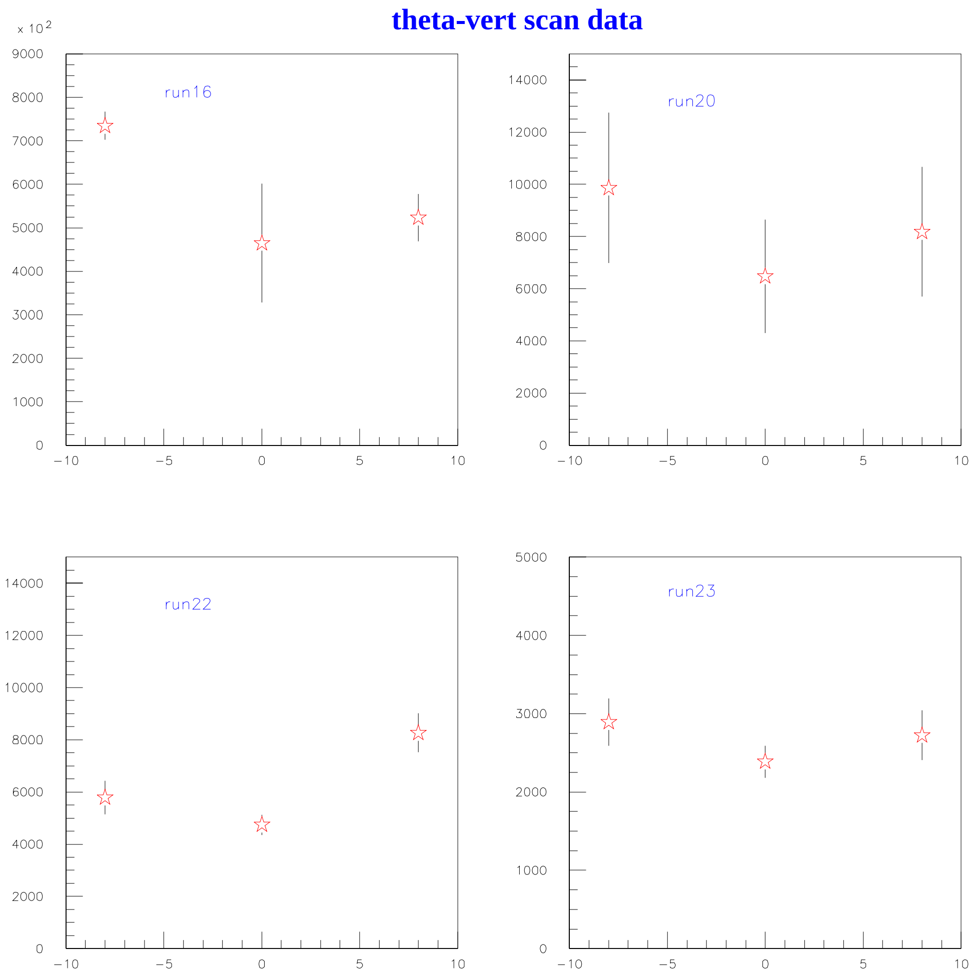

Figure 5.15: The vertical axis in each plot is the U1.U2 rate observed over a 5 second interval after subtracting the background rate. Along the x-axis is the $\theta_v$ on and off peak positions(refer table 5.4). The "0" corresponds to the on peak position. The absolute values for $\theta_v^{on-peak}$ can vary from run to run. The "non-zero" position corresponds to off-peak values for U1.U2 rate.

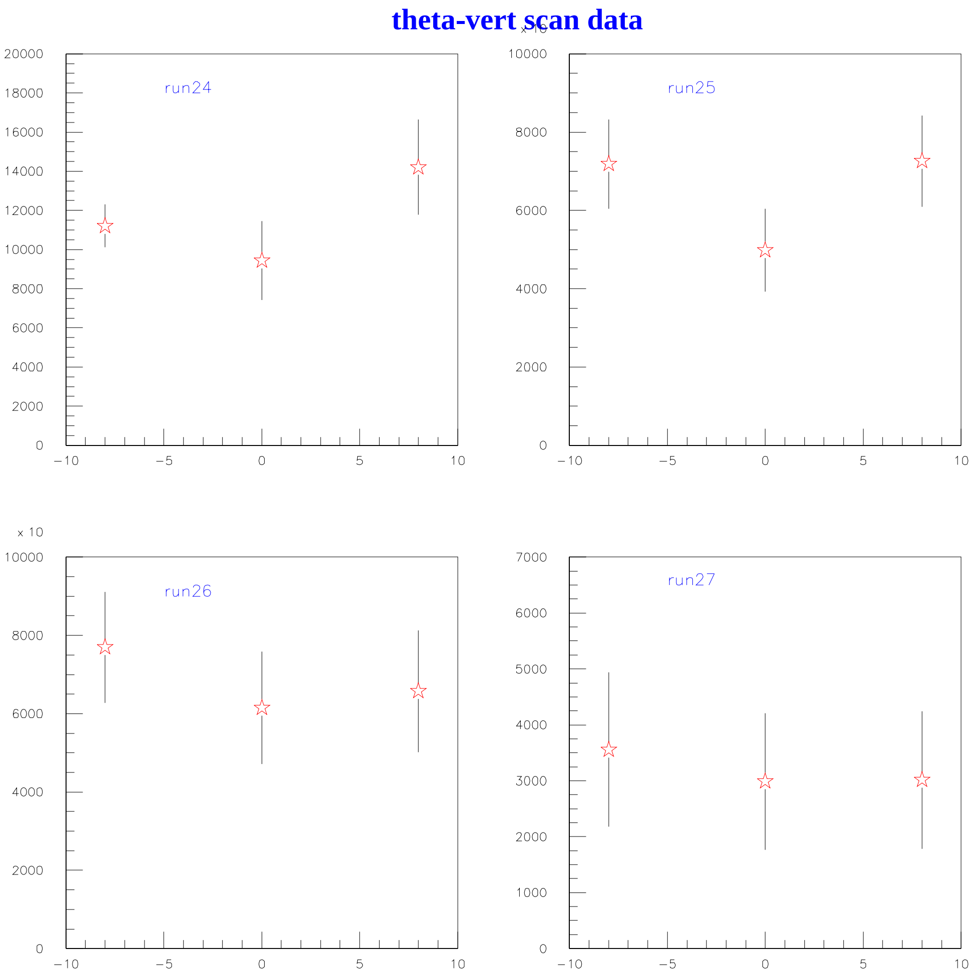

Figure 5.16: The vertical axis in each plot is the U1.U2 rate observed over a 5 second interval after subtracting the background rates. Along the x-axis is the $\theta_v$ on and off peak positions(refer table 5.4). The "0" corresponds to the on peak position. The absolute values for $\theta_v^{on-peak}$ can vary from run to run. The "non-zero" position corresponds to off-peak values for U1.U2 rate.

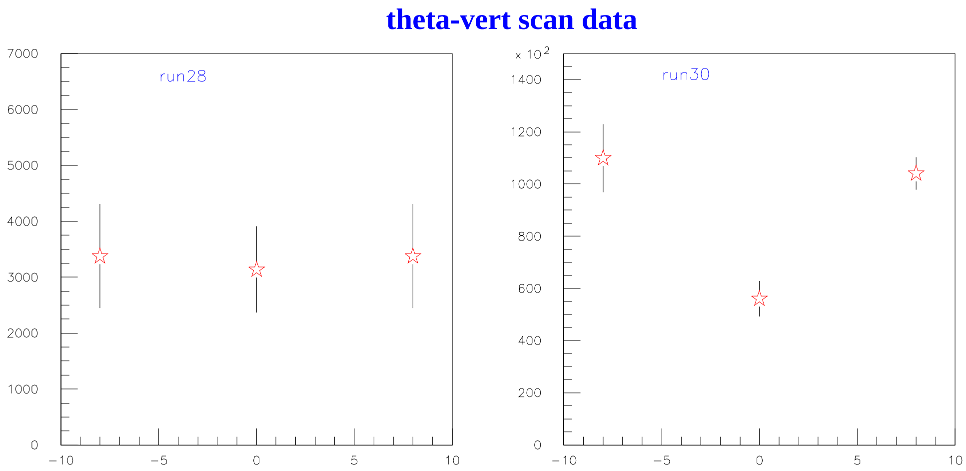

Figure 5.17: The vertical axis in each plot is the U1.U2 rate observed over a 5 second interval after subtracting the background rates. Along the x-axis is the $\theta_v$ on and off peak positions(refer table 5.4). The “0” corresponds to the on peak position. The absolute values for $\theta_v^{on-peak}$ can vary from run to run. The “non-zero” position corresponds to off-peak values for U1.U2 rate.

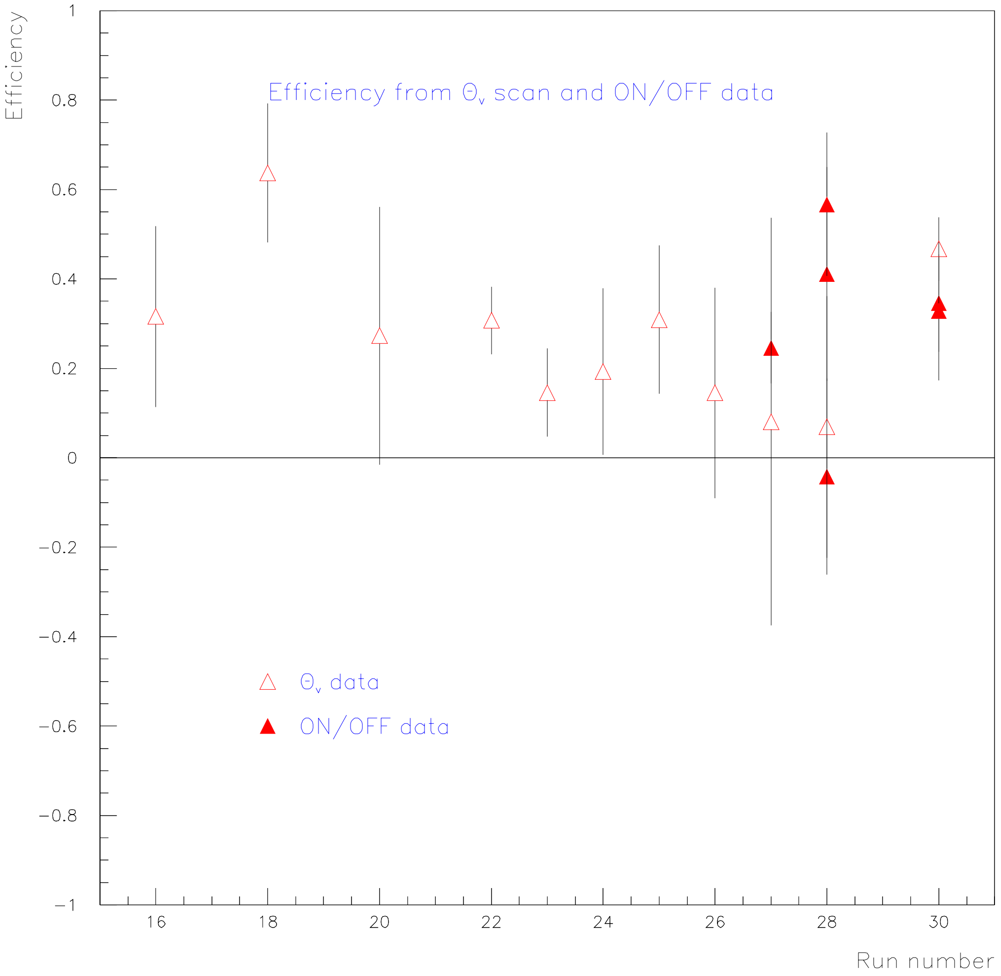

Figure 5.18: A summary of all efficiency measurements using the Dip seen in the inelastic interaction counters. Open triangles are from the $\theta_v$ scans and the solid triangles represent the on/off peak data. In the case of run number 27, 28 and 30 the values are in agreement within errors for the two different data samples.

did not have a direct measurement of the beam flux that falls on the crystal face. One could instead use the observed changes in the number of circulating protons in the Tevatron as we move the crystal into the beam halo. The difference in the loss rate before the crystal went in, to the loss rate after the crystal was moved into the beam halo gives a measure of the circulating beam lost due to the crystal alone. However, this depends also on the absolute value of the loss rate with the crystal out condition. There could be other sources of a large loss of the circulating protons in the Tevatron during the crystal out condition and then this method will fail, as was the case in a few of the runs.

### 5.4.1 Beam Loss measurements

Data extracted from ACNET on SBPSUM (sum of 6 bunches averaged over many turns) which monitors the amount of the circulating beam in the Tevatron was split into two or more sets depending on whether it corresponded to the time when the crystal was in the beam or not. Each data set was then fit to an exponential given by,

$$N_t = N_{t_0} e^{-\frac{t-t_0}{\tau}} \tag{5.5}$$

where $t_0$ is chosen to be roughly half-way of the time-span for the given data set. $N_{t_0}$ and $\tau$ are extracted from the fit. The loss rate is given by the derivative of the number of circulating protons which is,

$$N_t' = \frac{dN_t}{dt} = -\frac{N_t}{\tau} \tag{5.6}$$

and the associated error is given by,

$$\delta N_t^{'} = N_t^{'} \sqrt{(\frac{\delta N_{t_0}}{N_{t_0}})^2 + (\frac{\delta(1/\tau)}{1/(t - t_0 - \tau)})^2} \tag{5.7}$$

where $\delta N_t^{'}$ and $\delta(1/\tau)$ are the errors on the parameters used in the fit.

| run no. | xtal out | xtal in | change in slope |
|---|---|---|---|
| 16 | $(5.16 \pm 4.40) \times 10^5$ | $(4.18 \pm 0.73) \times 10^5$<br>$(1.37 \pm 0.05) \times 10^6$<br>$(10.66 \pm 0.41) \times 10^5$ | $(5.5 \pm 4.42) \times 10^5$ |
| 18 | $(0.88 \pm 0.40) \times 10^5$ | $(1.49 \pm 1.15) \times 10^5$<br>$(4.28 \pm 0.70) \times 10^5$<br>$(3.53 \pm 0.60) \times 10^5$ | $(2.65 \pm 0.72) \times 10^5$ |
| 20 | $(3.20 \pm 0.03) \times 10^6$ | $(3.99 \pm 0.14) \times 10^6$ | $(0.79 \pm 0.14) \times 10^6$ |
| 21 | $(4.35 \pm 0.09) \times 10^6$ | $(4.74 \pm 0.06) \times 10^6$ | $(0.39 \pm 0.11) \times 10^6$ |
| 22 | $(3.69 \pm 0.07) \times 10^6$<br>$(3.83 \pm 0.02) \times 10^6$<br>$(3.82 \pm 0.02) \times 10^6$ | $(3.74 \pm 0.13) \times 10^6$ | $(-0.08 \pm 0.13) \times 10^6$ |
| 23 | $(4.04 \pm 0.08) \times 10^6$ | $(4.30 \pm 0.03) \times 10^6$ | $(0.26 \pm 0.09) \times 10^6$ |
| 24 | $(4.45 \pm 0.02) \times 10^6$ | $(4.64 \pm 0.21) \times 10^6$ | $(0.19 \pm 0.21) \times 10^6$ |
| 25 | $(4.32 \pm 0.03) \times 10^6$ | $(4.54 \pm 0.05) \times 10^6$ | $(0.22 \pm 0.06) \times 10^6$ |
| 26 | $(4.65 \pm 0.01) \times 10^6$ | $(4.95 \pm 0.01) \times 10^6$ | $(0.30 \pm 0.01) \times 10^6$ |
| 27 | $(4.69 \pm 0.01) \times 10^6$<br>$(4.82 \pm 0.05) \times 10^6$<br>$(4.70 \pm 0.01) \times 10^6$ | $(4.89 \pm 0.04) \times 10^6$<br>$(4.77 \pm 0.02) \times 10^6$<br>$(4.79 \pm 0.02) \times 10^6$ | $(0.30 \pm 0.01) \times 10^6$ |
| 28 | $(4.39 \pm 0.04) \times 10^6$<br>$(4.64 \pm 0.06) \times 10^6$<br>$(4.47 \pm 0.03) \times 10^6$ | $(4.51 \pm 0.01) \times 10^6$ | $(0.04 \pm 0.03) \times 10^6$ |

Table 5.6: Beam loss measurements using exponential fits

### 5.4.2 Beam Lifetime

The fits to the beam loss rate done in the previous section can be represented also in terms of a familiar quantity the beam lifetime in the machine. The numbers for

| | | | |
|---|---|---|---|
| 30-1 | $(1.778 \pm 0.0244) \times 10^5$<br>$(1.8521 \pm 0.0254) \times 10^5$ | $(4.153 \pm 0.0038) \times 10^6$ | $(39.68 \pm 0.05) \times 10^5$ |
| 30-2 | $(1.8521 \pm 0.0254) \times 10^5$ | $(6.136 \pm 0.058) \times 10^5$ | $(4.284 \pm 0.063) \times 10^5$ |
| 30-3 | $(4.402 \pm 0.0604) \times 10^5$ | $(2.43 \pm 0.0023) \times 10^6$ | $(19.898 \pm 0.065) \times 10^5$ |
| 30-4 | $(4.402 \pm 0.0604) \times 10^5$<br>$(3.88 \pm 0.0699) \times 10^5$ | $(4.2 \pm 0.03) \times 10^5$ | $(0.32 \pm 0.076) \times 10^5$ |

Table 5.7: Run 30 loss rates

the various runs can then be compared with the characteristic Luminosity lifetime for the Tevatron during collider operations. What we do observe is that the lifetime is not adversely affected by our use of the crystal to extract $10^{-7}$ of the circulating protons. A summary of these numbers are given in the table below.

### 5.4.3 Efficiency Analysis

A practical definition for the efficiency would be,

$$\epsilon_{extraction} = \frac{AG1\ rate}{change\ in\ loss\ rate\ of\ circulating\ protons} \tag{5.8}$$

The AG1 rate has to be corrected for the background contribution (very small) to its rate and the effect of the multiple bucket occupancy. There is a correction to the AG1 rates due to the 95% efficiency of the AG1-1 and AG1-2 counters. These efficiencies were measured using cosmic rays as well as beam gas scatter events that travel down the beam pipe into the abort line. Since AG1 is defined as a coincidence of the two the net efficiency for AG1 is 90%. The background rate at AG1, due to cosmics and radioactivity from the beam pipe region is roughly 10% of the AG1 count for all runs. The counter efficiency and the background corrections cancel each other out. Hence, the significant correction to the AG1 rates is the multiple occupancy effect.

| Run no. | Xtal Status | Lifetime (in hours) | remarks |
|---|---|---|---|
| 16 | out | 106 | |
| | in | 128.7 | Xgon @ 50 $\mu m$ moving |
| | in | 28 | Xgon @ -1450 $\mu m$ |
| 18 | in Noise Off | 432 | |
| | in Noise On | 254 | Xgon @ -250 $\mu m$ |
| | in Noise On | 88 | Xgon @ -500 $\mu m$ |
| 20 | out | 102 | |
| | in | 79.6 | Xgon @ 1700 $\mu m$ |
| 21 | out | 77.2 | |
| | in | 68.9 | Xgon @ 2250 $\mu m$ |
| 22 | out | 82.98 | |
| | out | 80.45 | |
| | in | 80.84 | Xgon @ 4800 $\mu m$ |
| 23 | out | 81.2 | |
| | in | 74.3 | Xgon @ 2775 $\mu m$ |
| 24 | out | 73.85 | |
| | in | 68.63 | Xgon @ 3500 $\mu m$ |
| 25 | out | 63.1 | |
| | in | 58.2 | Xgon @ 3400 $\mu m$ |
| 26 | out | 66 | |
| | out | 56.6 | Xgon @ 2550 $\mu m$ |
| 27 | out | 61.8 | |
| | out | 56.9 | |
| | in | 54.4 | Xgon @ 2050 $\mu m$ |
| | in | 52.7 | Xgon @ 2050 $\mu m$ |
| | in | 47.4 | Xgon @ 3050 $\mu m$ |
| 28 | out | 76.5 | |
| | out | 70.7 | |
| | in | 70.8 | Xgon @ 3400 $\mu m$ |
| 30 | in | 137.5 | Xgon @ 3000-150 $\mu m$ |
| | in | 122 | Xgon @ 150 $\mu m$ |
| | in | 9.32 | Xgon @ 3000-150 $\mu m$ |
| 30 | out | 133 | Xgon @ 8mm |
| | in Noise Off | 121 | Xgon @ 150 $\mu m$ |
| | in Noise On | 9.35 | Xgon @ 150 $\mu m$ |

Table 5.8: Beam Lifetime summary

To study the correction required to the data for AG1 rates due to the possibility of multiple events being counted only once as bucket occupancy increases, we took data with high AG1 rates of the order of 100 KHz with the $AA$ trigger with the Main Ring veto and all other conditions stable. In most runs we had 6 bunches circulating, hence the total number of buckets over a 5 second livetime of the trigger gate would be given by,

$$no.\ of\ buckets/sec = \frac{1\ turn}{20.94\ \mu\ second} \times 6 \tag{5.9}$$

which is 287 buckets/second for the case with 6 bunches. Using the fact that counter efficiency was 90% the average rate per bucket can be calculated as,

$$average\ AG1\ count/bucket = \frac{raw\ AG1\ rate}{0.90 \times 287} \tag{5.10}$$

The multiple occupancy problem can be treated as a Poissonian distribution given by,

$$P(U,n) = \frac{e^{-U}\ U^n}{n!} \tag{5.11}$$

where $U$ is the average number of particles per bucket, and $n$ is the number of particles in a given bucket which can run from 0,1,2,3,...etc with decreasing probability for larger occupancy. The error for P(U,0) is given by,

$$\sqrt{\frac{P\ (1-P)}{N_{tot}}} \tag{5.12}$$

where $N_{tot}$ is the total number of events analysed from the $AA$ trigger data. The $AA$ trigger data can now be fit to this model for bucket occupancy and the fit results extracted to give the true value for the average which we call $U^{fit}$. This can then be used in turn to calculate $P(U^{fit}, n = 0)$ which we call $P_0$ for brevity. The correction to the AG1 rate is then simply given by,

$$\frac{U^{fit}}{1 - P_0} \tag{5.13}$$

For a complete account of this correction refer to the internal memo [23] which has all the details. The correction factors for those runs when available are listed in Table 5.9.

| Run no. | AG1 (5 sec) | multiple occupancy correction factor | Extraction Efficiency in % |
|---|---|---|---|
| 16 | $305410 \pm 97071$ | 1.92 | $21.3 \pm 9.6$ |
| 18 | $186698 \pm 13905$ | 1.24 | $17.5 \pm 4.0$ |
| 20 | $138111 \pm 11103$ | 1.05 | $3.7 \pm 0.7$ |
| 21 | $242733 \pm 22579$ | 1.10 | $13.8 \pm 3.7$ |
| 22 | $129741 \pm 5274$ | | $-32.4 \pm 52.7$ |
| 23 | $52492 \pm 1354$ | | $4.0 \pm 1.4$ |
| 24 | $188716 \pm 27081$ | 1.06 | $21.1 \pm 22.1$ |
| 25 | $172000 \pm 14423$ | 1.06 | $16.5 \pm 4.5$ |
| 26 | $163430 \pm 30262$ | | $10.9 \pm 2.1$ |
| 27 | $110273 \pm 19510$ | 1.44 | $35.3 \pm 7.0$ |
| 28 | $168794 \pm 20895$ | 1.16 | $97.9 \pm 64.2$ |
| 30-1 | $777227 \pm 71928$ | 1.0 | $3.9 \pm 0.4$ |
| 30-2 | $425752 \pm 103346$ | 1.0 | $19.9 \pm 4.8$ |
| 30-3 | $843513 \pm 9424$ | 1.06 | $9.0 \pm 0.1$ |
| 30-4 | $44417 \pm 10637$ | 1.0 | $27.8 \pm 9.4$ |

Table 5.9: Extraction efficiency summary

Taking a weighted average of the final efficiency obtained for different runs when the mean value is at least of $3\sigma$ significance, we obtain $8.6 \pm 0.1$ % for the extraction efficiency. We are justified in doing so as the large fluctuations in the SBPSUM losses even within a run can be attributed to effects not directly related to the crystal. The negative numbers for Run 22 is due to the large losses in

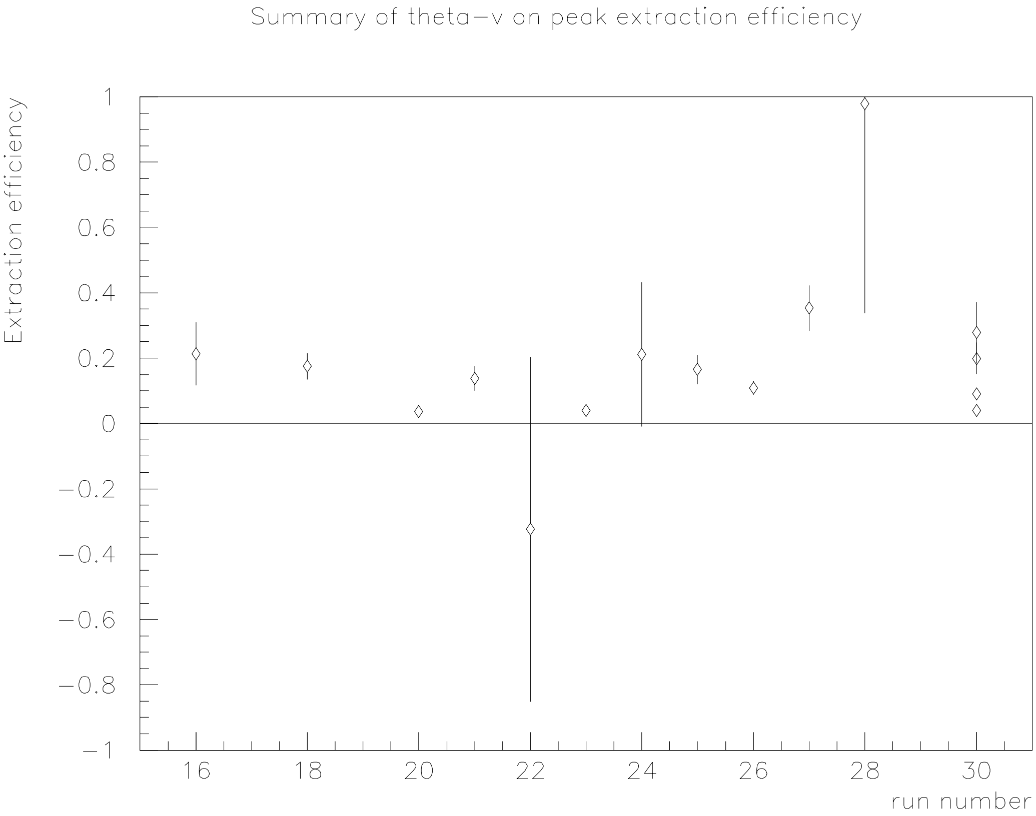

Figure 5.19: A summary of all efficiency measurements using the AG1 rates sitting at $\theta_v$ peak and the beam loss due to the crystal intercepting the beam estimated using SBPSUM monitors for the circulating beam current. In the case of Run 30 IBEAMS information was used instead because the beam was uncoalesced. The large errors indicate the short comings of this method in correctly estimating the amount of beam lost by interactions with the crystal as opposed to other causes of loss in the Tevatron.

the Tevatron long before the crystal was moved close to the beam. It should be noted that the channeling efficiency measured using the dip seen in the interaction counters yielded a weighted average of $34.11 \pm 3.95$ %. Simulation results in the diffusion mode from Biryukov suggests a channeling efficiency of 38% for the case of silicon crystal similar to that used in E853.

### 5.4.4 Extraction Rate

In most runs we achieved peak extraction rates of 100kHz or more. The Table 5.10 lists the extraction rates recorded for different run conditions. We also reached a peak rate of 900 KHz with 36 on 3 bunches very close to our goal of a 1 MHz extraction rate. During this special run the D0 loss was 1.6 times their normal tolerable limit (set for Run I) with the crystal out of the beam. The loss limit went up marginally to 2 times the normally allowed value when the crystal was moved into the beam and the extraction rate was in the 500-900 KHz range.

| store mode/comments | circ. protons | extraction rate |
|---|---|---|
| proton-only, 3 bunches | $10^{11}$ | 60-200 KHz |
| 6 on 6, colliding | $10^{12}$ | 30-150 KHz |
| 36 on 3, D0 Loss = 2 × limit | $3 \times 10^{12}$ | 500-900 KHz |
| proton-only, 84 bunches | $1 \times 10^{11}$ | 95 KHz |
| RF damper noise on | | > 450 |

Table 5.10: Extraction Rates under different run conditions

# PART II

## Measurement of the $b\bar{b}$ production cross section at $\sqrt{s} = 38.8$ GeV

# Chapter 6

# Theoretical Motivation

## 6.1 Standard Model

The Standard Model is a well understood framework which has quite consistently predicted and explained many of the startling experimental measurements made in the field of High-energy physics over last few decades. Experiments continue to be designed and conducted subjecting the Standard Model to stringent tests as we proceed in our efforts to better understand the nature of the laws of physics at the most fundamental level possible.

Since the advent of quantum theory a broad classification of all particle states has been based on their intrinsic spin as these values largely determine their alone behaviour. Thus all integer spin particles (*bosons*) followed a statistics different from that of the half-integer spin ones (*fermions*). The electric charge of all experimentally observed particles could be expressed as integer multiples of the charge of an electron. Particle masses, on the other hand, ranged in values from a few $MeV/c^2$ to hundreds of $GeV/c^2$ without an obvious pattern. In the context of the standard model all matter is composed of fermions and the interactions which gov-

| Field | Number of Carriers | Electric Charge | Mass (GeV) | Spin-(Parity) | Symmetry | Lifetimes (sec) | Force |
|---|---|---|---|---|---|---|---|
| g (gluon) | 8 | 0 | 0 | $1^-$ | SU(3) | $10^{-23}$ | Strong |
| $\gamma$ (photon) | 1 | 0 | 0 | $1^-$ | U(1) | $10^{-20}$ | E-M |
| $W^{\pm}$ | 2 | $\pm1$ | 80.22 | $1^-$ | SU(2) | $10^{-8}$ | Weak |
| $Z^0$ | 1 | 0 | 91.17 | $1^+$ | SU(2) | $10^{-8}$ | Weak |
| G (graviton) | 1 | 0 | 0 | $2^+$ | ? | - | Gravitational |

Table 6.1: Fundamental forces of nature

ern them are mediated by bosons. The four known fundamental forces in nature are classified in the table 6.1. They are gravitational, electromagnetic, strong and the weak interaction. The hypothesised mediator for the gravitational force has not yet been observed in nature, though gravity itself is historically the first force studied by physicists. The electromagnetic interaction is mediated by the photon, which is a massless and chargeless object. The carriers of the weak interaction are the $W^+$, $W^-$ and the $Z^0$ bosons. They all are massive and are then limited in their range in contrast to photons. The strong force carriers consist of eight gluons distinguished by their color charges. These charges can self-couple and this leads to the "strong" nature of this force. The additional feature of the strong force is *asymtotic freedom*: at very small distances the quarks behave almost like free particles, but as the separation distance increases the strong force increases linearly with distance, making it impossible to pull a free quark out of hadrons. The strong force is responsible for the stability of the proton.

Matter is composed of quarks and leptons. Quarks come in six flavors and are classified into three generations based on a mass heirarchy. For each particle, an anti-particle also exists. Leptons also come in three generations each is a doublet. The six quark flavors are up, down, strange, charm, beauty and top. The six leptons are the electron, muon, tau and their corresponding neutrinos. The quark

| | Generations | | | Charge | Spin | Forces Experienced |
|---|---|---|---|---|---|---|
| | $1^{rst}$ | $2^{nd}$ | $3^{rd}$ | | | |
| quarks | u (2-8 MeV) | c (1.0-1.6 GeV) | t ($180 \pm 12$ GeV) | +2/3 | 1/2 | Strong<br>E-M<br>Weak |
| | d (5-15 MeV) | s (100-300 MeV) | b (4.1-4.5 GeV) | -1/3 | 1/2 | |
| leptons | e (0.511 MeV) | $\mu$ (105.7 MeV) | $\tau$ (1.78 GeV) | -1 | 1/2 | E-M<br>Weak |
| | $\nu_e$ (<7.3 eV) | $\nu_\mu$ (<0.27 MeV) | $\nu_\tau$ (<35 MeV) | 0 | 1/2 | Weak |

Table 6.2: Fundamental constituents of matter: Quarks and Leptons. Particle masses from the Particle Properties Data Booklet.

and leptons are also separately listed in table 6.2. Quarks carry fractional electric charges: +2/3 for the upper entry and -1/3 for the lower entry of each doublet. Each quark can come in three color charges which is the equivalent of the electric charge for the strong interaction. Whereas leptons do not carry the color charge and hence do not experience the strong force, which binds the quarks together to form colorless states of 2-quark, 3-quark states called *mesons* and *baryons* respectively, or *Hadrons* in general. Historically, it was the large number of particles discovered that led some theorists to conjecture that hadrons were composed of fundamental units called quarks. The substructure of nucleons was later revealed in deep inelastic scattering experiment performed at SLAC in 1965.

Borrowing ideas from classical mechanics, it is conventional in particle physics to formulate a Lagrangian and from it all observables can be calculated in principle using the rules of quantum field theory. The invariance of the theory under some local transformations dictates the form for the interaction term. Such theories are called "Gauge Theories". It should also be noted that an invariance under a transformation implies also an associated conservation law. Just as translational invariance of the laws of classical physics imply linear momentum conservation and rotational invariance implies angular momentum conservation in real space-time, we also have conservation laws for internal spaces like SU(3) color space and SU(2) electro-weak space as there are transformation laws that apply in each of these spaces. The conservation law maifests itself in the charges in each of these internal-spaces that leads to a new interacton between particles.

For a theory of quarks and leptons which are spin-1/2 particles the appropriate Lagrangian to start with is the one that gives us the Dirac equation,

$$\mathcal{L} = \sum_i \overline{\psi}_i (i\gamma_\mu \partial_\mu - m)\psi_i \tag{6.1}$$

where the $\psi$'s are the doublets for the left-handed fermion fields and singlets for the right-handed fields and $\gamma_\mu$'s are the $4 \times 4$ Dirac matrices. The left-handed fields for the $i^{th}$ fermion family are given by,

$$\psi_i = \begin{pmatrix} \nu_i \\ l_i^- \end{pmatrix} \quad or \quad \begin{pmatrix} u_i \\ d_i^{'} \end{pmatrix} \tag{6.2}$$

where the $d_i^{'}$ is

$$d_i^{'} = \sum_j V_{ij} d_j \tag{6.3}$$

and V is the Cabbibo-Kobayashi-Maskawa mixing matrix.

$$\begin{pmatrix} d^{'} \\ s^{'} \\ b^{'} \end{pmatrix} = \begin{pmatrix} V_{ud} & V_{us} & V_{ub} \\ V_{cd} & V_{cs} & V_{cb} \\ V_{td} & V_{ts} & V_{tb} \end{pmatrix} \begin{pmatrix} d \\ s \\ b \end{pmatrix} \tag{6.4}$$

The origin of the CKM matrix is due to the fact that in the Standard Model the charged weak decays are not flavor conserving, i.e. the weak eigenstates are not the same as the flavor eigenstates, by convention the down-type quarks are rotated to obtain the weak eigenstates. The $3 \times 3$ rotation matrix is called the CKM matrix. As the elements are complex numbers there are 18 parameters to be experimentally determined. Unitarity of the CKM matrix reduces this number to 4 (3 angles and a phase). The phase allows for CP violation within the Standard Model.

The concept of a "covariant derivative" comes from electrodynamics. It essentially redefines the derivative so the Lagrangian, which contains terms consisting of derivatives of the field, remains invariant as a whole for a given transformation of the field itself. The full covariant derivative for describing all interactions in the Standard Model of $U(1) \times SU(2) \times SU(3)$ spaces is given by,

$$\mathcal{D}^{\mu} = \partial_{\mu} - ig_1 \frac{Y}{2} B^{\mu} - ig_2 \frac{\tau_i}{2} W_i^{\mu} - ig_3 \frac{\lambda_a}{2} G_a^{\mu} \tag{6.5}$$

the scalar product in SU(2) is for $i = 1, 2, 3$ and the product in SU(3) is for $a = 1, 2, ...8$. The couplings denoted as $g$'s, are all real numbers. The $\tau_i$'s are the $2 \times 2$ Pauli matrices and $\lambda_a$'s are the $3 \times 3$ matrices that are the generators of the SU(3) space. The spin-one gauge fields $B^{\mu}$, $W_i^{\mu}$'s and $G_a^{\mu}$'s must exist. The first two terms are singlets, the third is a 2-dimensional matrix in SU(2) and the last one a 3-dimensional matrix in SU(3) space. When the above relation is used instead of the $\partial_{\mu}$ in the Lagrangian, it gives us the full theory of the Standard Model.

In order to explain the masses of the gauge bosons and for fermions a new spin-zero field, the Higgs field is postulated. The Lagrangian for this field has the form,

$$\mathcal{L}_{\phi} = (\partial_{\mu}\phi)^{\dagger}(\partial^{\mu}\phi) - \mu^2 \phi^{\dagger}\phi - \lambda(\phi^{\dagger}\phi)^2 \tag{6.6}$$

where $\phi$ is,

$$\phi = \begin{pmatrix} \phi^+ \\ \phi^0 \end{pmatrix} \tag{6.7}$$

and $\phi^+$ and $\phi^0$ are each complex fields,

$$\phi^+ = \frac{\phi_1 + i\phi_2}{\sqrt{2}} \tag{6.8}$$

$$\phi^0 = \frac{\phi_3 + i\phi_4}{\sqrt{2}} \tag{6.9}$$

From the Lagrangian the potential term $V(\phi)$, which is the the last two terms of the Lagrangian in eqn 6.6 has a minimum for $\mu^2 < 0$ at

$$\phi^\dagger\phi = \frac{-\mu^2}{2\lambda} \tag{6.10}$$

Since,

$$\phi^\dagger\phi = \frac{(\phi_1^2 + \phi_2^2 + \phi_3^2 + \phi_4^2}{2}) \tag{6.11}$$

there are multiple ways in which equation 6.10 can be satisfied. Choosing a direction in SU(2) space and expanding around that minimum will lead to different results, thereby breaking the symmetry of the vacuum. With the choice $\phi_3 = v, \phi_1 = \phi_2 = \phi_4 = 0$ the vacuum $\phi_0$ is,

$$\phi_0 = \tfrac{1}{\sqrt{2}} \begin{pmatrix} 0 \\ v \end{pmatrix} \tag{6.12}$$

It should be noted that the potential $V(\phi)$ is invariant under the local gauge transformation

$$\phi(x) \to \phi^{'}(x) = e^{i\vec{\alpha}(x).\vec{\tau}/2}\phi(x) \tag{6.13}$$

To also make the Lagrangian invariant under this transformation it is necessary to replace $\partial_\mu$ with $D_\mu$ as shown in eqn 6.5. From the algebra mass terms for the W's and the Z can be identified in terms of the coupling constants and the vacuum expectation value $v$ by,

$$\begin{aligned} M_w &= vg_2/2 \\ M_z &= \tfrac{1}{2}v\sqrt{g_1^2+g_2^2} \\ M_\gamma &= 0 \end{aligned} \tag{6.14}$$

Fermion masses can also be understood by extending the same ideas. We can add an interaction term to the Lagrangian for the leptons,

$$\mathcal{L}_{int} = g_e(\bar{L}\phi e_R^- + \phi^\dagger \bar{e}_R^- L) \tag{6.15}$$

We can now calculate the consequences of adding this term by replacing

$$\phi \longrightarrow \begin{pmatrix} 0 \\ \frac{v+H}{\sqrt{2}} \end{pmatrix} \tag{6.16}$$

the Lagrangian now takes the form,

$$\mathcal{L}_{int} = m_e\bar{e}e + \frac{m_e}{v}\bar{e}eH \tag{6.17}$$

and we get for the lepton mass $m_e = g_e v/\sqrt{2}$.

For quarks an added complication arises from the fact that the right-handed doublet can exist. The complex conjugate of an SU(2) doublet is also a doublet. The most general Lagrangian is then,

$$\mathcal{L}_{int} = g_d\bar{Q}_L\phi d_R + g_u\bar{Q}_L\phi_c u_R + Herm.\ conjugate \tag{6.18}$$

Expanding once again the spectrum around the vacuum gives

$$\mathcal{L}_{int} = m_d \bar{d}d + m_u \bar{u}u + \frac{m_d}{v}\bar{d}dH + \frac{m_u}{v}\bar{u}uH \tag{6.19}$$

This procedure can be extended to the other two quark and lepton families. Note that since all the coupling terms are arbitrary the masses are not determined by the theory and need to be measured.

## 6.2 Parton Model for Hadroproduction

Heavy quark production cross-sections can be calculated based on the QCD improved parton model. The parton model was originally conceived by Feynman to provide a physical picture of a high energy scattering event in a frame in which the hadron is rapidly moving. In the boosted frame of the hadron, parton evolution time has been dilated such that the hard scattering event involving the partons occurs in a much smaller time scale, making it possible to treat the partons as effectively free during the interaction. In this frame the number density of partons of given type within a momentum fraction interval given by a distribution function $f_i(x)$. These functions also known as structure functions are independently measured in deep inelastic scattering experiments with point particles (electrons or muons) consituting the beam and protons and neutrons the targets. For heavy quarks the cross section can be calculated as a perturbation series in the strong QCD running coupling constant $\alpha_s$, which is evaluated at the mass of the heavy quark.

In the QCD parton model the cross section $\sigma$ for a hard scattering with mo-

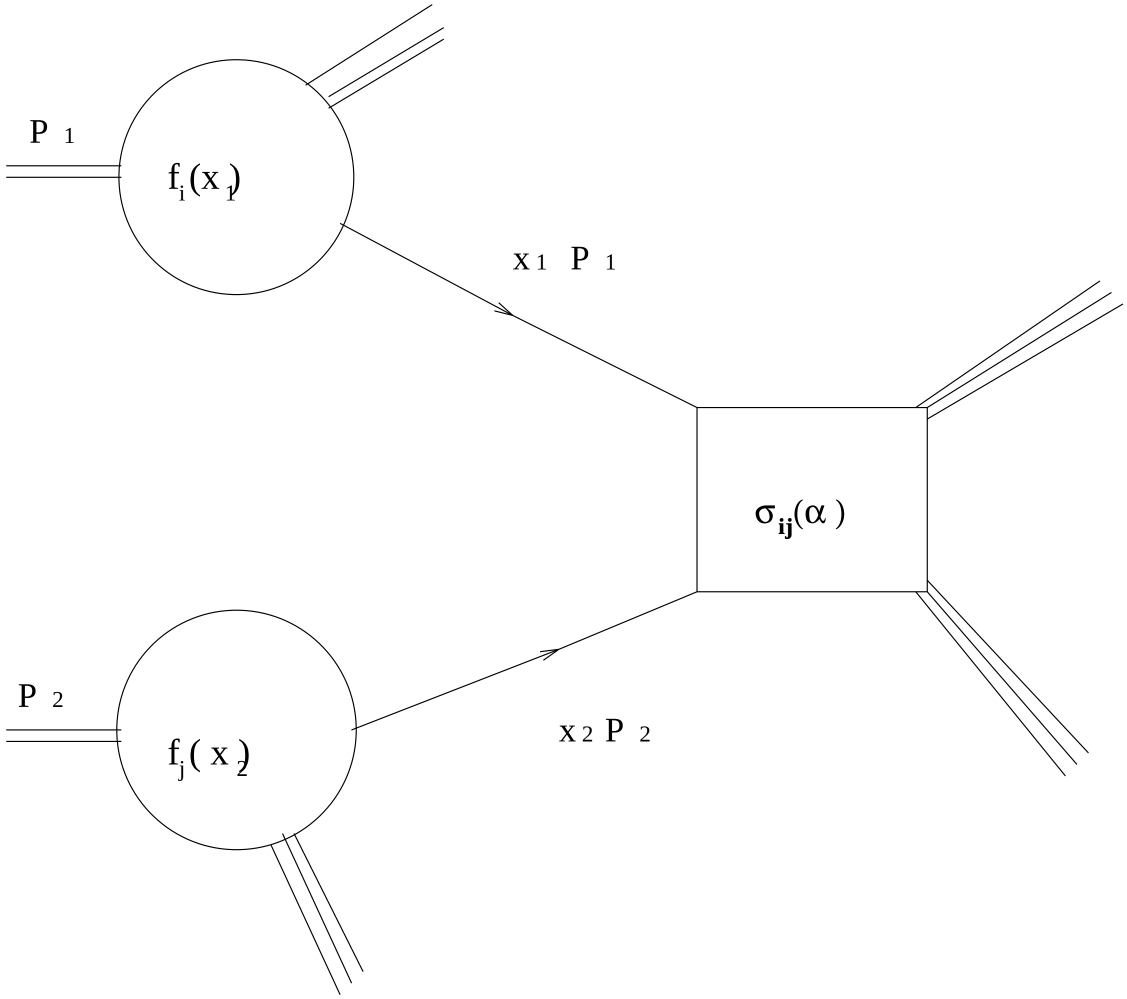

Figure 6.1: Parton model picture for High-energy scattering

mentum scale Q is given by,

$$\sigma(P_1, P_2) = \sum_{i,j} \int dx_1 dx_2 f_i(x_1, \mu) f_j(x_2, \mu) \hat{\sigma}_{ij}(\alpha_s(\mu), x_1 P_1, x_2 P_2) \tag{6.20}$$

The sum on $i$ and $j$ runs over the light quarks, anti-quarks and gluons. $\mu$ is an arbitrary scale chosen to be of the order of the mass of the heavy quark. $\hat{\sigma}_{ij}$ denotes the short-distance cross section for the partons. The final result is limited by the uncertainities in our knowledge of the gluon structure functions.

The dominant processes leading to production of heavy quarks are,

$$q(p_1) + \bar{q}(p_2) \rightarrow Q(p_3) + \bar{Q}(p_4) \tag{6.21}$$

$$g(p_1) + \bar{g}(p_2) \rightarrow Q(p_3) + \bar{Q}(p_4) \tag{6.22}$$

and the diagrams contributing at this level to these processes are shown in figs. 6.2.

In consideringheavy flavor production in their paper P. Nason et.al. [29] express the short distance cross section as,

$$\hat{\sigma}_{ij} = \frac{\alpha_s^2(\mu^2)}{m^2} f_{ij}(\rho, \frac{\mu^2}{m^2}) \tag{6.23}$$

with $\rho = 4m^2/s$, $s$ is the square of the partonic centre of mass energy, and $\mu$ is the renormalisation and factorisation scale. Their calculation also includes next-to-leading order contributions through $O(\alpha_s^3)$. A more recent work by Kidonakis & Smith [26] includes the large logarithms that arise from imperfect cancellation of the soft-plus-virtual terms in the perturbation expansion. They have reexamined all the

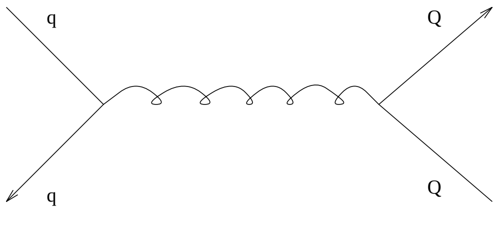

Fig a

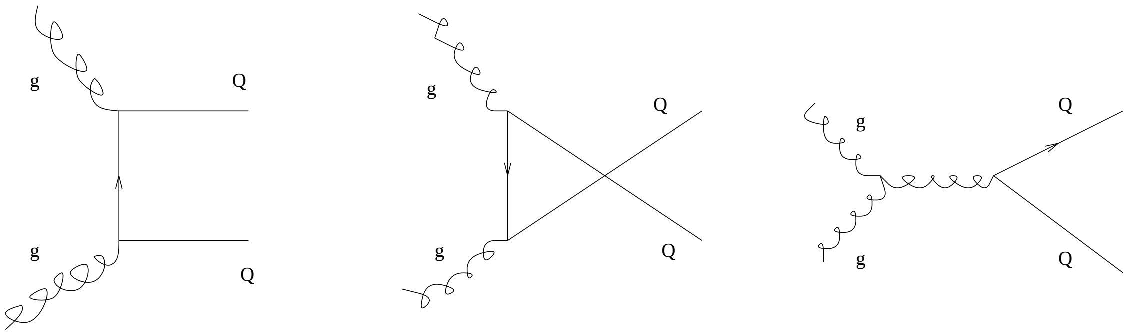

Fig b

Figure 6.2: Lowest level Feynman Diagrams for Heavy-Quark Production

corrections near threshold, which is the case for fixed target b-quark experiments, where the gluon-gluon channel dominate.

## 6.3 Beauty Physics at Fixed Target

Historically, the b-quark system was seen first at a fixed target experiment at Fermilab by Lederman *etal.* in 1977 [25]. It was a resonance named later as $\Upsilon$. Though in the fixed target mode the center-of-mass energy grows much slower than in a collider mode the Luminosities achieved can be much higher ($\approx 10^{34} cm^{-2} s^{-1}$). In practice Fixed Target experiments are limited by spectrometer, data acquisition and other considerations. In the previous Fixed Target cycle till 1992 at Fermilab the experiments E653, E771, E789 and E672 attempted B-physics programs. All of these experiments have been successful in reconstructing only a handful of B events so far.

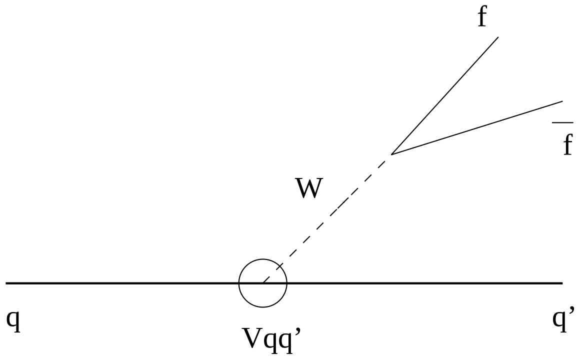

Figure 6.3: CKM matrix elements from weak decays

There are several reasons for the increasing interest in the study of the B mesons, in the context of the Standard Model, both in terms of the production processes as well as the decay schemes. Since, Beauty mesons decay weakly they constitute an excellent system to measure the various CKM matrix elements. The relatively heavier mass of the b quarks with respect to the lighter flavors makes it a better testing ground for perturbative calculations of its decay and production processes. From an experimental standpoint, the heavier mass also leads to larger amount of energy released in its decay to charm quarks resulting in associated leptons having significant transverse momentum which can serve as a decay signature.

A measurement of all the CKM matrix elements will provide a definitive test of the origins of CP violation being in the phase term or due to new physics outside of the Standard Model. The various decay schemes as illustrated in the figures 6.3 makes it possible to measure the CKM elements $V_{ub}$, $V_{cb}$, $V_{td}$ and $V_{ts}$.

Understanding the production mechanisms for heavy quarks in the Collider and Fixed Target programs are complementary to each other. In fact in the specific case of b-quark production described previously, at the parton level the contributions in the next-to-leading order (NLO) are dominated by logarithmic terms that become significant near the threshold region. Until recently the calculations at the NLO level did not take into account these terms for the gluon-gluon channel as this specific mode does not contribute significantly to the cross section in the collider mode, where the quark-antiquark contribution is dominant. This is mainly due to the fact that the parton densities involved in the cross section calculations are much different in collider $p\bar{p}$ and Fixed Target $pp$ collisions. In the latter the the sea-quark densities are much smaller than the valence quark densities. The $K$ factor, defined by $K = (\sigma^{(0)} + \sigma^{(1)}|_{exact})/\sigma^{(0)}$, where $\sigma^{(0)}$ is the Born term and $\sigma^{(1)}|_{exact}$ is the exact first order correction. The $K$ factor is large for the $gg$ channel. It is also shown in [26] that for $\eta = (\frac{s}{4m^2} - 1)$, between 0.1 and 1 the cross section rises sharply indicating that the threshold region is very important, and then plateaus for $s >> 4m^2$.

Another important point to note is the scale dependence of the NLO results. Kidonakis et al. [26] show how the Born term, the exact first-order correction and the total $O(\alpha_s^3)$ cross section, varies with the change of the factorisation scale for $q\bar{q}$ and $gg$ channels. As the scale decreases, the Born term increases without bound and the exact first order correction decreases faster making the NLO cross setion peak at a value for the scale close to half the mass of the bottom quark and then it falls for decreasing values of the scale. For the $q\bar{q}$ channel the NLO cross section is flat. But for $gg$ case the peak is very sharp and the scale dependence greater and is reflected in the total cross section.

# Chapter 7

# E771 Detector

The E771 experiment was designed to study, among other things, the production of B mesons identified by their decay into final states containing muons. The experiment ran for about a month towards the end of the 1991-1992 Fixed Target run at $2 \times 10^6$ interactions per second with a 800 GeV/c proton beam on a set of silicon targets. The experiment took data at the highest rates possible consistent with the data acquisition capacity. The interaction rates and the beam size were set so as to collect the maximum amount of data given the shortness of the run and the limited instrumentation of the silicon tracker planes. A total of 150 million dimuon triggers and 70 million single muon triggers were written to tape during the run. Only those detector systems relevant to this analysis will be described in what follows. A more complete discussion can be found in [45].

## 7.1 Beam

To deliver 800 GeV/c protons to the experiment hall, located at the High Intensity Lab, some modifications had to be made to the intermediate beamline elements. The secondary beam portions of the beamline enclosures PW6, PW7 and PW8 had to be upgraded to handle the primary beam. To reduce the the $10^{11}$ protons per pulse delivered by the switchyard to $4 \times 10^9$ or less, two collimators were added at PW2 and PW5. Each collimator had three holes, each with a square cross section, so as to provide a wide range of attenuation factors. The quadrupoles in PW6 and PW7 were used to focus the beam down to $6mm$ diameter circular spot on the target foils. The target foils represented in total 5.2% of an interaction length. The non-interacting protons passed through the deadend region of the wire chambers and were absorbed in the tungsten and steel central portion of the muon spectrometer region. Since the trigger was based on muons it was necessary to veto those events where the muons did not originate in the target. A veto system comprised of 49 scintillator counters was positioned upstream of the target region. In principle all charged tracks outside of the $5cm$ diameter beam hole would cause the rejection of events due to the presence of beam halo.

## 7.2 Silicon System

### 7.2.1 Target

The target system consisted of 12 foils of pure silicon, each $2mm$ thick and spaced $4mm$ apart leading to a total of $6.4cm$ for the target region 7.2. This corresponds to an interaction length of 5.2%. The additional material of the silicon tracker ($4.2mm$) is not considered in this analysis. Events with the primary vertex outside

Figure 7.1: E771 spectrometer

of the foil region were not retained for further analysis by the primary vertex quality program offline.

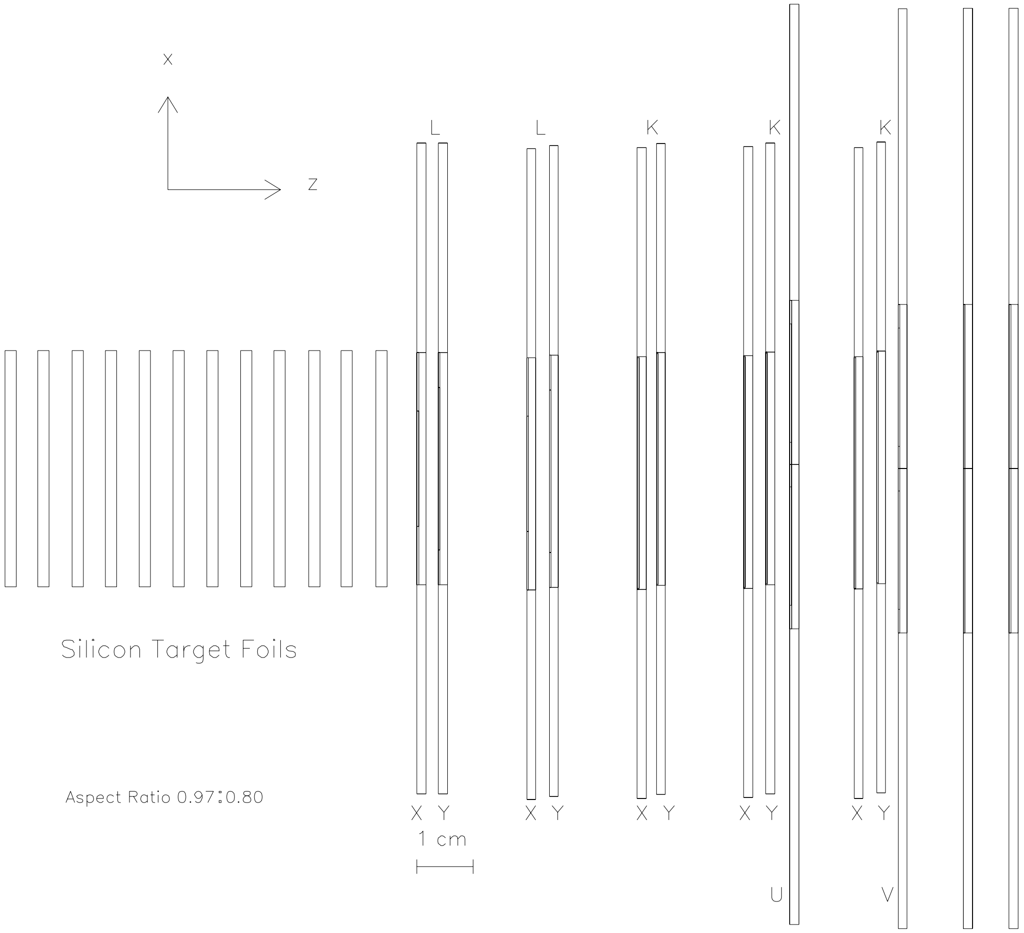

Figure 7.2: E771 Silicon detector arrangement

### 7.2.2 Vertex Detector

Six silicon strip planes upstream of the spectrometer were used to measure the beam position. The first plane of the silicon tracker was 5*mm* downstream of the

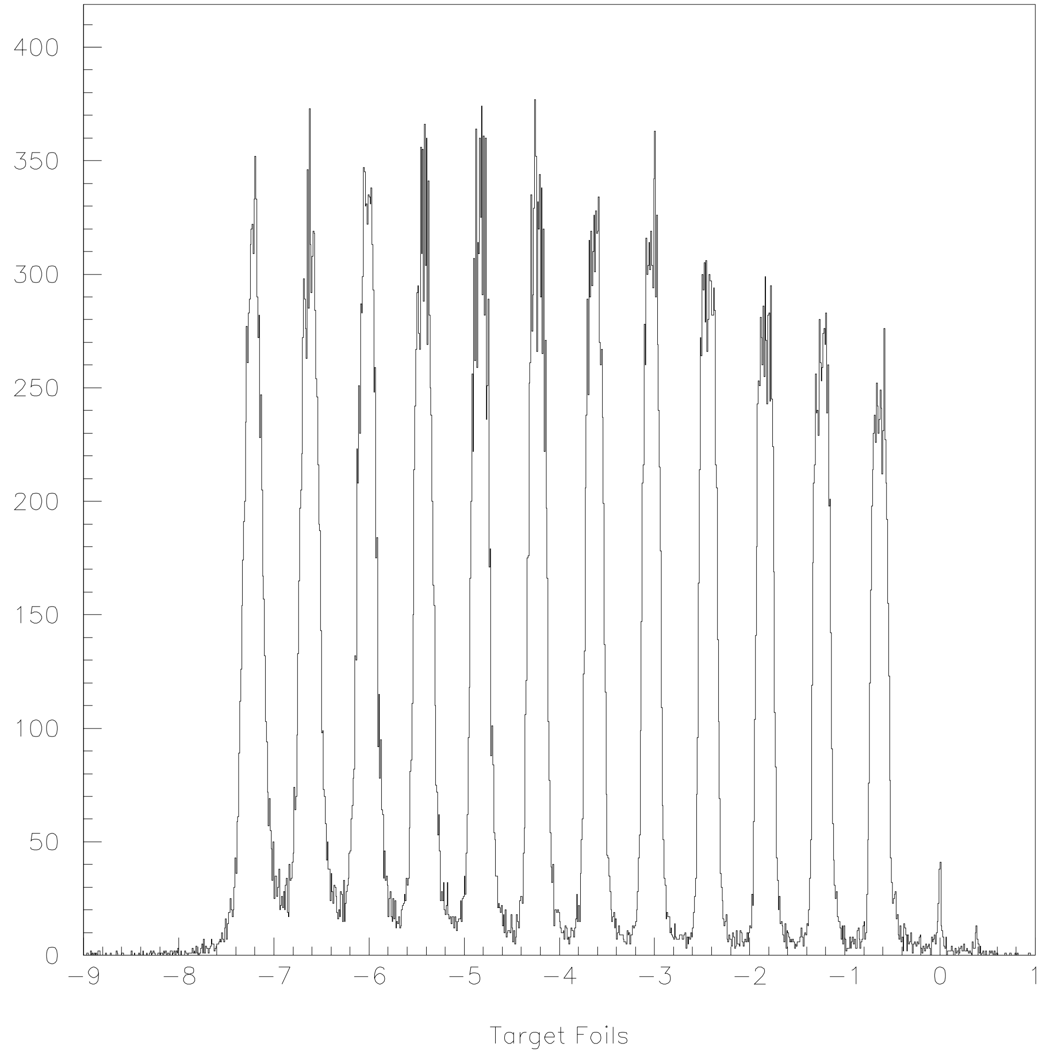

Figure 7.3: Silicon target foils are shown using the distribution of the primary vertex from different events.

last target foil. The SSD system has a total of 12 planes (5X, 5Y, 1U, 1V). The U and V planes were oriented at 45° with respect to the X and Y planes. The SSD system was $10cm$ long and roughly $(5 \times 5)cm^2$ in area. Each tracker station consisted of 2 or 3 planes, $4mm$ apart, and the stations were spaced at $2cm$ interval. The planes were $(300 \pm 5)\mu m$ thick. Details are given in the table 7.1. The survey of the planes was done to an accuracy of $5\mu m$ after installation on a granite frame for mechanical stability. The tracker frame was surrounded by an RF shield which was electrically connected to the pre-amplifiers through Be-Cu fingers built into the gaskets in the RF shield. There was an outer RF shield in addition to the inner one, to provide protection to the adjoining electronics from RF sources in the experimental area. It also doubled as part of a thermal shield, with a water cooled chiller to provide temperature stability for the entire detector.

Detector alignment and performance issues were addressed in an earlier thesis [70]. The radiation damage in the central region during the high intensity data taking is discussed in [48].

The readout for the silicon detector was housed in FASTBUS crates with each crate carrying $12 \times 128$ channels. The analog signal from the pre-amplifier which was housed next to the silicon detector strips, is discriminated by the Postamp/Comparator modules (12 in each crate). The discriminator thresholds varied between 10 to 50 mVolts and could be set for individual or a collection of channels. For every P/C module there was a dedicated Delay Encoder module to which the discriminated signal is transferred via the auxiliary backplane every 18.9 ns. The data were then stored here to a maximum time of 4.8 $\mu$s for a trigger decision. The D/E basically consisted of a ring buffer to which data gets recorded every RF cycle avoiding any deadtime in the system. The Sequencer card for each

Table 7.1: Silicon detector positions and dimensions.

| Chamber | $Z$ Position ($cm$) | $\Delta X$ ($cm$) | $\Delta Y$ ($cm$) | $X$ Offset ($cm$) | $Y$ Offset ($cm$) |
|---|---|---|---|---|---|
| Beam X1 | -696.893 | 1.50 | 1.50 | 0.234 | 0.000 |
| Beam X2 | -696.493 | 1.50 | 1.50 | 0.238 | 0.000 |
| Beam Y1 | -671.573 | 1.50 | 1.50 | 0.000 | 0.213 |
| Beam Y2 | -671.173 | 1.50 | 1.50 | 0.000 | 0.213 |
| Beam X3 | -586.393 | 1.24 | 1.75 | -0.094 | 0.000 |
| Beam Y3 | -585.993 | 1.75 | 1.24 | 0.000 | 0.044 |
| Tracker X1 | -572.580 | 1.24 | 1.75 | 0.000 | 0.000 |
| Tracker Y1 | -572.200 | 1.75 | 1.24 | 0.000 | 0.000 |
| Tracker X2 | -570.630 | 1.24 | 1.75 | -0.114 | 0.000 |
| Tracker Y2 | -570.230 | 1.75 | 1.24 | 0.000 | -0.057 |
| Tracker X3 | -568.670 | 2.48 | 2.50 | -0.096 | 0.000 |
| Tracker Y3 | -568.330 | 2.50 | 2.48 | 0.000 | -0.011 |
| Tracker X4 | -566.780 | 2.48 | 2.50 | -0.070 | 0.000 |
| Tracker Y4 | -566.390 | 2.50 | 2.48 | 0.000 | 0.001 |
| Tracker U1 | -565.960 | 1.76 | 1.76 | 0.063 | 0.063 |
| Tracker X5 | -564.820 | 2.48 | 2.50 | -0.087 | 0.000 |
| Tracker Y5 | -564.420 | 2.50 | 2.48 | 0.000 | 0.018 |
| Tracker V1 | -564.040 | 1.76 | 1.76 | 0.003 | 0.003 |

crate accepted the trigger signal and strobed the data buffer for each D/E card in the crate inititaing a readout of the triggered bucket. The D/E also encodes the hit strip into a 8-bit word and output the hit strip list to the Sequencer over the FASTBUS backplane. A single Master Timing Controller for the entire SSD readout generated the address of the triggering bucket which was then sent to all the Sequencers. The Sequencer transfers the data into a FIFO buffer memory where the 8-bit data words were combined with the 7-bit D/E address and a 1-bit flag to distinguish data from control words to form a 16-bit word. This is finally read out via the FASTBUS Smart Crate Controller into the DAQ.

## 7.3 Momentum Analysis

### 7.3.1 Magnet

The momentum analysis was done using a 150 ton, large aperture dipole magnet. The center of the magnet served as the origin (Z=0) of the spectrometer reference system. The magnet aperture dimensions are $185.5cm$ in width, $91.4cm$ in height and $152.4cm$ in length. The saddle shaped coils each contain 240 turns. The magnet current during the run was $2,400 Amperes$, producing a vertical field of about $1.43 Tesla$. This corresponds to a transverse momentum impulse of $821 MeV/c$. Magnetic field measurements, done using two independent techniques (using ZIPTRACK and Hall probe), agreed to 0.1%.

### 7.3.2 Proportional Wire Chambers

The upstream trajectories of charged particles were determined from 22 planes of multiwire proportional chambers (MWPC) and a plane of drift chamber. Most of the MWPC planes were deadened in the central beam area. There were three large aperture proportional chamber (PC) modules and four small aperture central proportional chamber (PCB) modules mostly to cover the dead PC and Drift Chamber regions.

Each PC module consists of three parallel planes with different stereo angles ( X, U and V views) with a common gas volume. PC1 had an extra plane in X view. All relevant parameters are listed in the table 7.2. The PC chambers were operated with a conventional “Magic Gas” mixture (23% isobutane, 4% methylal, 0.5% freon and the rest was argon). The deadening of the central beam region was done by electroplating copper into a circular area on the wires. A reduction in efficiency by two orders of magnitude was achieved by doubling the wire diameters.

The four PCB modules, which complemented the PC’s and DC’s covered a smaller solid angle and also had a dead region in the center for each plane to reduce the large chamber currents due to the impinging beam. The operational principle was the same as for the PC’s but they had a slightly different gas mixture (25% isobutane, 5% methylal, 0.8% freon and argon).

### 7.3.3 Drift Chambers

The six drift chamber modules (DC), contained 21 wire planes and provided a precise measurement of track positions than the PC’s. DC1, DC2 and DC3 were located upstream of the analysis magnet, while DC4, DC5 and DC6 were downstream. The upstream modules had three wire planes oriented in different stereo angles (X, U and V views), whereas the downstream modules had four planes with an additional X view. Table 7.3 has the details listed. All DC’s operated with a gas mixture of 50% argon and 50% ethane which was bubbled through ethanol at

Table 7.2: Proportional chamber geometry.

| Chamber | View | Views tan $\theta$ | $Z$ Position $(cm)$ | No. Wires | Wire Spacing $(cm)$ | Full Gap $(cm)$ | Wire width $(\mu m)$ | Cathode Planes | Dead Area |
|---|---|---|---|---|---|---|---|---|---|
| PC1B | V | -0.533 | -465.7 | 176 | 0.085 | 0.6 | 12.5 | $25\mu$ kapton foil | 1.5 $\times$1.5 (cm$^2$) |
|  | X | 0.0 | -465.1 |  | 0.075 |  |  |  |  |
|  | U | 0.533 | -464.5 |  | 0.085 |  |  |  |  |
| PC1 | X' | 0.0 | -446.5 | 352 | 0.151 | 1.27 | 20.0 |  | 5.08 cm radius |
|  | V | -0.3 | -445.2 |  | 0.158 |  |  |  |  |
|  | X | 0.0 | -443.9 |  | 0.151 |  |  |  |  |
|  | U | 0.3 | -442.7 |  | 0.158 |  |  |  |  |
| PC2B | V | -0.533 | -424.3 | 160 | 0.113 | 0.6 | 12.5 | $25\mu$ kapton foil | 1.5 $\times$1.5 (cm$^2$) |
|  | X | 0.0 | -423.7 |  | 0.100 |  |  |  |  |
|  | U | 0.533 | -423.1 |  | 0.113 |  |  |  |  |
| PC2 | U | 0.3 | -376.7 | 480 | 0.159 | 1.27 | 20.0 |  | 5.08 cm radius |
|  | X | 0.0 | -375.5 |  | 0.151 |  |  |  |  |
|  | V | -0.3 | -374.2 |  | 0.159 |  |  |  |  |
| PC3 | V | -0.3 | -306.7 | 512 | 0.209 | 1.22 | 20.0 |  | 6.35 cm radius |
|  | X | 0.0 | -305.4 |  | 0.200 |  |  |  |  |
|  | U | 0.3 | -304.2 |  | 0.209 |  |  |  |  |
| PC3B | V | -0.533 | -284.3 | 160 | 0.113 | 0.6 | 12.5 | $25\mu$ kapton foil | 1.5 $\times$1.5 (cm$^2$) |
|  | X | 0.0 | -283.7 |  | 0.100 |  |  |  |  |
|  | U | 0.533 | -283.1 |  | 0.113 |  |  |  |  |
| PC4B | V | -0.533 | -196.9 | 160 | 0.113 | ? | 12.5 | ? | 1.5 $\times$1.5 (cm$^2$) |
|  | X | 0.0 | -196.3 |  | 0.100 |  |  |  |  |
|  | U | 0.533 | -195.7 |  | 0.113 |  |  |  |  |

Table 7.3: Drift chamber geometry.

| Chamber | View | Views tan $\theta$ | $Z$ Position ($cm$) | No. Wires | Wire Spacing ($cm$) | Full Gap ($cm$) | Wire width ($\mu$m) | Cathode Planes | Dead Area |
|---|---|---|---|---|---|---|---|---|---|
| DC1 | U | 0.3 | -256.7 | 192 | 0.600 | 0.6 | 20.0 | $\phi = 63.5$ $s = 0.10$ | 6.35 cm radius |
| | X | 0.0 | -256.1 | | | | | | |
| | V | -0.3 | -255.4 | | | | | | |
| DC2 | V | -0.3 | -235.2 | 92 | 1.270 | 1.27 | 25.4 | 0.025 Al foil | 6.35 cm radius |
| | X | 0.0 | -234.0 | 93 | | | | | |
| | U | 0.3 | -232.7 | 93 | | | | | |
| DC3 | U | 0.3 | -221.3 | 93 | 1.270 | 1.27 | 25.4 | 0.025 Al foil | 6.35 cm radius |
| | X | 0.0 | -220.0 | 92 | | | | | |
| | V | -0.3 | -218.7 | 92 | | | | | |
| DC4 | V | -0.3 | 170.7 | 124 | 1.905 | 1.905 | 25.4 | 0.025 Al foil | 25.72 $\times$11.4 (cm$^2$) |
| | X | 0.0 | 172.6 | 124 | | | | | |
| | U | 0.3 | 174.5 | 123 | | | | | |
| | X' | 0.0 | 176.4 | 123 | | | | | |
| DC5 | X' | 0.0 | 619.6 | 176 | 1.905 | 1.905 | 25.4 | $\phi = 63.5$ $s = 0.19$ | 26.67 $\times$7.62 (cm$^2$) |
| | V | -0.3 | 621.6 | 192 | | | | | |
| | X | 0.0 | 623.5 | 176 | | | | | |
| | U | 0.3 | 625.4 | 192 | | | | | |
| DC6 | X' | 0.0 | 724.4 | 176 | 1.905 | 1.905 | 25.4 | $\phi = 63.5$ $s = 0.19$ | 26.67 $\times$7.62 (cm$^2$) |
| | V | -0.3 | 726.3 | 192 | | | | | |
| | X | 0.0 | 728.2 | 176 | | | | | |
| | U | 0.3 | 730.1 | 192 | | | | | |

$5^0C$. The central dead region of the downstream planes had a rectangular shape to allow for the horizontal bending of the charged tracks by the magnet.

### 7.3.4 Pad Chambers

The Pad chambers [59] were actually drift chambers with additonal pad and stripe readout planes. Six of these chambers, CC1, CC2, CC3, CC4, WC1 and WC2, were located downstream of the magnet. Each chamber module consisted of two sets of anode wires, two sets of stripes and two sets of pads. The wires gave x-position measurements, whereas the stripes and pads gave both X and Y position measurements. Pad signals were also used for an on-line high transverse momentum trigger processor.

Table 7.4: Pad chamber positions and dimensions.

| Chamber | $Z$ Position | $\Delta X$ $(cm)$ | $\Delta Y$ $(cm)$ | $\Delta X$ Hole $(cm)$ | $\Delta Y$ Hole $(cm)$ |
|---|---|---|---|---|---|
| CC1 | 230.1 | 179.2 | 102.4 | 19.2 | 9.6 |
| CC2 | 271.0 | 179.2 | 102.4 | 19.2 | 9.6 |
| CC3 | 804.2 | 115.2 | 179.2 | 19.2 | 16.8 |
| CC4 | 823.8 | 115.2 | 179.2 | 19.2 | 16.8 |
| WC1 | 784.3 | 115.2 | 179.2 | 0.0 | 0.0 |
| WC2 | 784.4 | 115.2 | 179.2 | 0.0 | 0.0 |

## 7.4 Muon Identification

The muon detector for E771 [55] consisted of three planes of Resistive Plate Counter modules interspersed with hadron absorbers. RPC's were thin gap gas devices filled with a mixture of 53% argon, 43% butane and 5% freon. The counters operated in the streamer mode in a high and uniform electric field (40 $kV/cm$). The charge produced by the streamer process was picked up by the external copper pads.

The first and second RPC planes consisted of standard modules and two L shaped modules surrounding the beam dump. Overlapping of modules was necessary to avoid dead zones along the perimeter. Nine ($2 \times 1m^2$) modules were assembled to form the third detector plane. The pad cells had dimensions ($6 \times 6\ cm^2$) for central modules and ($12 \times 12\ cm^2$) for the outer region.

## 7.5 Online Triggers

The Beam trigger which signals the passage of a beam particle into the spectrometer was defined as a coincidence of the RF from the accelerator, the absence of a signal from the veto wall for halo particles and the presence of two beam silicon planes hits in x-projection to give,

$$B_V = RF \cdot BSX \cdot \overline{VETO} \tag{7.1}$$

The interaction trigger was also based on the silicon system and it used the third tracking plane in x-projection called X3. As the target had a 5.2% interaction length a further reduction of unwanted events can be achieved with selecting only those events that have the primary interaction in the target material. A hit multiplicity cutoff in the X3 plane was used to this end. Using the approriate set of discriminator threshold values and logic units to select events where more than 8 but less than 80 hits were recorded in the X3 plane the interaction trigger was defined to be,

$$INT = B_V \cdot X3(>8) \cdot X3(<80) \tag{7.2}$$

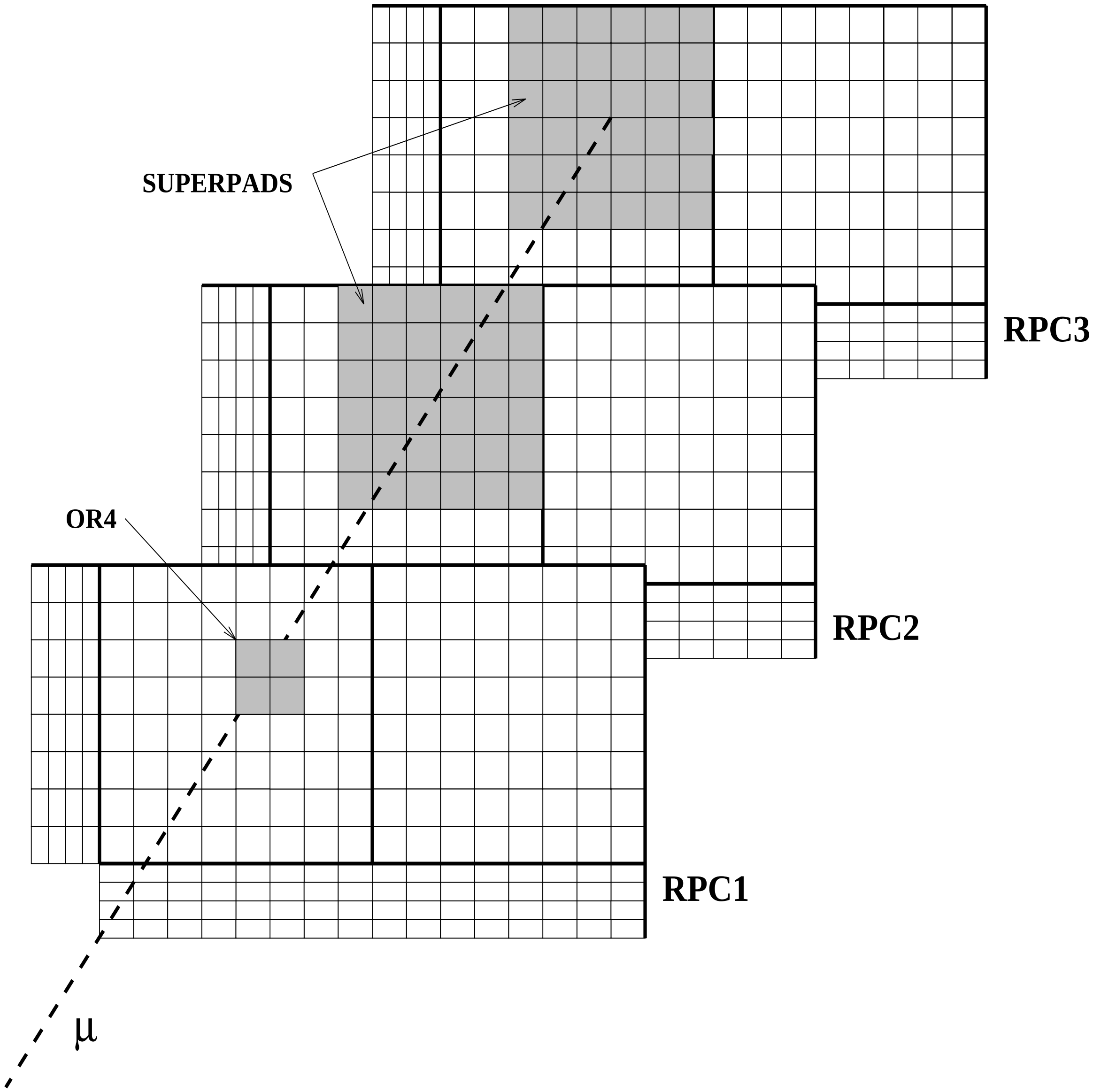

Figure 7.4: E771 Muon detector arrangement for a single quadrant in each plane is shown here. The definiton for the OR4 in the first RPC plane and the superpads in the second and third planes is also illustrated.

The E771 online trigger [76] composed of two levels, 1A and 1B, which were implemented independent of each other and ran in parallel. The level 1A trigger required the detection of at least one muon (energy $\geq 6\ GeV$), while the level 1B required the presence of at least one muon with a $p_t$ above a given threshold. We shall not describe the 1B trigger in any detail as it is not relevant to the data sample used in this analysis.

A pre-defined triple coincidence among a corresponding set of pads in the RPC planes formed the online definition of a muon. The basic unit was an OR of four $(2 \times 2)$ adjacent RPC pads. A 'Superpad' was defined to be an OR of the nine $(3 \times 3)$ OR4's, and muons were defined as the triple coincidence among an OR4 that fired in the first RPC plane and the corresponding superpads from the second and the third RPC planes. The size of the superpads was determined from the spread of muon trajectories due to multiple scattering in the steel. The total number of distinct triple coincidences that defined a muon was a quarter of the number of pads in the first RPC plane ($2048/4 = 512$). The trigger, which was constructed for nearly deadtimeless operation, took a total of $400ns$, out of which only $130ns$ was due to actual electronics processing and the rest due to cable transmission delay. Events were also rejected if adjacent horizontal/vertical SuperORs fired. The dimuon trigger definition can be written in a compact manner as,

$$1A_{2\mu} = (superOR(\geq 2) \cdot \overline{ADJ_H}) \cdot (superOR(\geq 2) \cdot \overline{ADJ_V}) \cdot INT \tag{7.3}$$

where $\overline{ADJ_H}$ and $\overline{ADJ_V}$ means the horizontal and vertical adjacency suppression.

## 7.6 DAQ

The Data acquisition system [75] was designed to allow processing of up to 600 events per second, averaged over the spill cycle, and assuming an event size of 12,000 bytes. The various FASTBUS and CAMAC crates were daisy chained in six channels, each feeding a single FIFO memory buffer. All six buffers were read in sequence by the ACP processor boards, which constructed complete events. Following this the event were written to one of twelve 8 millimeter Exabyte tape drives. A fraction of these events were also sent to a VAX 3500 workstation for real time monitoring of spectrometer performance.

The central Trigger-OR module accepted inputs from several different sources: Beam trigger, Interaction trigger, Calibration triggers, Single and Dimuon triggers. The Trigger-OR module supplied all of the readout crates with a gate signal to initiate the readout process and also reported readout completion, to allow new triggers to be processed. The CAMAC and FASTBUS controllers allowed a maximum of 2 Mbytes/sec and 40 Mbytes/sec respectively. The FIFO's had either 8 or 12 Mbytes of memory storage and provided a buffer for more than half the data taken during each spill, to accomodate for the slower tape drives and ACP boards.

## 7.7 Resolutions, Efficiency and Alignment

All of these studies to extract the various constants used a common technique dependant on hit redundancy for a given track. To extract the chamber efficiency, tracks were reconstructed without the hit information from the chamber, the efficiency of which was being measured. Then the success rate after a search for a hit in the chamber consistent with the given tracks gives a measure for the chamber efficiency. The procedure is repeated for all the detectors in the spectrometer to determine their individual efficiencies. Some of the details about the silicon efficiency can be found in [70].

The same technique also yields the residuals for the chambers. The residual is defined as the difference between the projected position for each track reconstructed in the chamber and the position of the associated hit found. The alignment of each chamber can be done in an iterative fashion by minimising the residuals. This is achieved by changing the alignment constants and then retracking to determine the residuals again. The procedure is terminated when the measured residual is within 20% of the expected value derived from theoretical considerations due to the finite spacing between individual wires or pads as the case may be. These numbers in turn are recorded in the parameter files for use by tracking and also when the monte-carlo overlay is performed to simulate the signal and background as reconstructed by the tracking program.

# Chapter 8

# Event Reconstruction

Event reconstruction encompassed many different processes such as decoding of the hits in the tracking chambers, pattern recognition of charge particle tracks from the hit information across the detector planes, upstream and downstream track reconstruction and full track matching. The latter process allowed the momentum determination of the charged particle track. Finally, more stringent criteria were imposed to clean up the event reconstruction reducing various sources of background begining with ghost tracks due to the hit multiplicities in the detector planes and road widths chosen to determine hits corresponding to a real track.

For every event, the hits from proportional, pad and drift chambers and the Resistive Plate Counters were decoded into the corresponding wire numbers or pads. These were in turn converted to co-ordinates in several projections of the spectrometer. Detector encoding and alignment constants, used in the conversion process, were stored in parameter files, based on the period of the run. The drift chamber parameter files also contained individual channel time-to-distance calibration constant. An accurate time-to-distance calibration of the TDC's is used for this purpose.

## 8.1 Tracking Algorithm

Pattern recognition and tracking were inextricably linked in the E771 analysis due to an interaction between the two processes. Details of event reconstruction: muon reconstruction, rear track construction, front track construction, silicon tracking and primary vertex determination are described in order.

To maximize muon track reconstruction an iterative procedure using information from the RPC pads, dimuon trigger and the muon counters was used. As explained earlier a pre-determined hit pattern in the three RPC planes used in the software trigger was compared with the latched information to recover missing pads and OR4's in the data. A muon candidate was reconstructed by requiring hits in all RPC planes and at least one corroborating muon counter. This combination was also required to be consistent with the dimuon trigger. The centers of the active pads were then fit to a line using the method of least squares. More candidate muons were added to this list, with hits required in two RPC planes and two muon counters in the second iteration and by requiring one RPC hit and three muon counter hits in the third iteration. At the end of each iteration the used hits were removed from consideration in the subsequent stages. This technique raises the muon reconstruction efficiencies of the algorithm to 99%.

For the purpose of rear tracking, all chambers located between the magnet and the steel in front of the muon chambers are used. Trajectories in this rear chamber set were determined by looping over rear seed planes in the x-projection. In the case of candidate muons, projecting the reconstructed muons onto the seed planes generated a search window for chamber hits. These seed lines were used to determine the slope and intercept at the center of the magnet. Next making the assumption that these tracks originated at the target center, the slope of the front seed line was also determined. The candidate track's momentum was determined using the standard prescription for charged particle deflection with the field in one projection.

In order to improve the quality of the candidate tracks, the remaining rear spectrometer tracking planes were searched for corroborating hits within $\pm 3.0mm$ of the seed line. After all the hits were found the two dimensional hits were refit, and the resulting track momentum is recomputed along with the modified muon slope and intercept parameters determined. For all remaining candidates the three dimensional trajectory was determined by projecting the $x$ position onto $u$ and $v$ planes of the drift chambers and pad chambers and searching for hit wires, strips and pads. Finally, all the hits associated with the candidate track were refit to a three dimensional line, the momentum re-determined, and a check was made for consistency with the muons as defined by the muon detector. The quality of the muon track was defined in terms of its $\chi^2$ per degree of freedom:

$$\chi^2_{dof} = \frac{1}{n-4}\sum_{i=1}^{n}(\frac{X_i - x_i}{\sigma_i})^2 \tag{8.1}$$

where $n$ is the number of hits on the track, $x_i$ is the position of the hit on the $i^{th}$ plane, $\sigma_i$ is the resolution of the $i^{th}$ plane and $X_i$ is the three dimensional intercept at the $i^{th}$ plane. An iterative procedure of dropping hits and recomputing the $\chi^2_{dof}$ was employed to find the best set of hits which passed the maximum $\chi^2_{dof}$ requirement and minimum hit requirement. If a set of hits did not meet this criteria then that candidate track was dropped. Rear tracks satisfying,

- a minimum of 1 pad hit on the track,

- a minimum of 6 hits in the x planes,

- a minimum percentage of hits in the y projection as determined by the maximum number of possible planes the track could have traversed,
- a maximum $|x|$ slope of 200.0 mradians,
- a maxinum $|y|$ slope of 60.0 mradians,
- a maximum $\chi^2/dof$ of 3.0

were saved for further analysis. For hadron tracks the same procedure was used except that the muon match requirement was not required.

Reconstruction of the front track began with an assumed vertex at the center of the target foils and the projection of the rear track on the magnet mid-plane at $z = 0$. A road was defined in the x-z projection around the vertex within $\pm 2.0cm$ and around the projection of the rear track at the magnet center within $\pm 1.0cm$. A seed line was defined within this road and all hits within $2.5\sigma$ of the seed line, where $\sigma$ is the resolution of the plane, were then fit to a line. From the slope and intercept information, three dimensional tracks were formed by projecting onto $u$ and $v$ planes to search for hits within the seed line. A final fit was made in the same manner as the rear tracks using all hits found within the search window and the $\chi^2/dof$ of the front track segment. Front tracks satisfying the following criteria below were saved.

- a minimum of 4 hits in the x projection,
- a minimum of 6 hits in the y projection,
- a maximum of $\chi^2/dof$ of 3.0

Beam tracks, as determined by the hits in the three x and three y beam silicon planes, narrowed down the search for the crude primary vertex. The beam tracks projected on to the silicon targets defined 12 interception points, one for each target foil. A function was defined which characterised the likelihood of a given position to be near to the primary interaction vertex. A line was drawn from the test point to any hit in any one of the silicon planes, and a search for hits in all other silicon planes within a window of the projection of the line on each plane was done in each view. The value of the response function is defined as the ratio of the total number of hits found ($n_{true}$) to the total number of projection points ($n_{considered}$),

$$f(v) = \frac{n_{true}}{n_{considered}} \tag{8.2}$$

The true primary vertex will have a value for the function high compared to the other test points. To determine a more precise estimate for the primary vertex, two dimensional tracks in both x and y projections were determined independently. The search window was 8 mm in both views from the vertex position. The least square fit method was used to fit the 2D tracks, with a minimum of three hits required in each projection. The $\chi^2$ for the precision primary was defined as,

$$\chi^2 = \sum_{j=1}^{n} \frac{\delta_j^2}{\sigma_j^2}, \tag{8.3}$$

where $\delta_j^2$ is the impact parameter of the track with the vertex position and $\delta$ the corresponding error. Tracks with four or more hits were used in this estimate. If the $\chi^2$ value was not acceptable, then the tracks most inconsistent with the vertex position was removed and the process is repeated till it succeeded or no tracks remain. The primary vertex routine was determined to have an efficiency of 80%.

## 8.2 Data Processing

The data processing of raw events took place over different stages in the development of the tracking program. To reduce the data sample to a manageable level, three passes of data processing were done. In the first pass the requirements were:

1. At least two muons were required in the event with one of the muons having a transverse momentum greater than 1 GeV/c.

The initial sample consisted of 150 million triggers and this was reduced by Pass I to approximately 43 million on 300 tapes. All of this processing was done on the Fermilab analysis farms which consisted of several IBM and SGI nodes running in parallel.

Pass II used an improved reconstruction algorithm (V7.3). At the same time the Kinematic requirements were increased:

1. leading muon transverse momentum greater than 1.5 $GeV/c$
2. Invariant mass in projection for muon pair greater than 1 $GeV/c^2$

Pass II reduced the sample by only about 10%. However, due to a better condensation of the data the pass II output was stored on approxiamtely 100 tapes.

The next level of processing included the silicon information. Demands on the quality of the primary vertex found by the silicon tracking and $\chi^2_{link}$ of the front and rear matches were made. The cuts consisted of:

1. Primary vertex within $3\sigma$ of the target foils.
2. $\chi^2_{link} < 100$
3. $10 < P_z < 100\ GeV/c$

4. at least 2 hits in the silicon were required in the x-projection
5. best-match criterion was used to link the front and rear matches for the muons

These cuts reduced the sample to 300,000 events which was output to two DST tapes. All of three passes were performed on the farms.

At about this time a final version of the full tracking program (V8.6) was implemented and this included the complete silicon information. This version also included routines to further clean up the track banks. All 300,000 events were retracked using this new version and additional kinematic cuts were imposed to reduce the backgrounds:

1. individual momentum of the muons forming the pair had to be greater than 15 $GeV/c$
2. invariant mass cut on the two muons, $M_{\mu\mu} > 2.0\ GeV/c^2$

At this point the events were separated into separate disk files on the basis of the charge of the muon candidates, identified as forming the "best" pair. The final result was two disk files containing 13,000 unlike sign muon pair events and 7,000 like sign muon pair events. These two files comprise the basic sample used in all subsequent analysis. Additional cuts were imposed only after studying the background contributions carefully using Monte Carlo generation and full detector reconstruction of the generated events.

# Chapter 9

# Data Analysis

The observed excess of the unlike sign muon pair events over the like sign muon pair events is the basic signal for the production of a $b\bar{b}$ pair and its subsequent decay into dimuon final states. Examples of unlike and like sign dimuon generation include

$$B \rightarrow \mu^+ X \qquad \bar{B} \rightarrow \mu^- X \tag{9.1}$$

$$B \rightarrow \mu^+ \bar{D} \rightarrow \mu^- X \tag{9.2}$$

$$B \rightarrow \mu^+ X \qquad \bar{B} \rightarrow DX \rightarrow \mu^+ X \tag{9.3}$$

$$B \rightarrow J/\psi X \rightarrow \mu^+ \mu^- \tag{9.4}$$

There are other sources that can give rise to a final state containing a $\mu+$ and $\mu-$, and these need to be subtracted from the observed excess. These subtractions require a study of the background processes and their acceptance in the spectrometer. Knowledge of the background sources also suggests cuts on the data to make an estimate of the cross section for $B\bar{B}$ production.

The dominant background events are,

- $D \rightarrow \mu^+ X \bar{D} \rightarrow \mu^- X$

- Drell-Yan production of $\mu^+\mu^-$ pairs

- leakage of $\mu^+\mu^-$ pairs from decay of $J/\psi$ outside of mass window.

- in flight decays of Pions and Kaons

where the last three occur when a false impact parameter for the muon track with respect to the primary vertex was reconstructed.

## 9.1 Monte-Carlo Generation

For the purpose of event generation PYTHIA 5.6 and JETSET 7.3, were used. These are based on the Lund model. GEANT 3.15 was used to propagate MC events through the E771 spectrometer. The various decay channels were passed through the full detector simulation to determine acceptance and efficiency as a function of the analysis cuts.

The full detector simulation does take into account all known processes that occur as the particles produced in the target traverse through the detector elements. The physics processes it addresses are:

- $\gamma \rightarrow e^+e^-$

- Compton scattering

- Photoelectric effect

- Multiple scattering

- Ionization energy loss

- Delta rays production
- Bremstrahlung
- $e^+e^-$ annihilation
- Decays in flight
- Hadronic interactions

The various chamber resolutions are read in from a lookup table and the detector hits are appropriately assigned for a given track, reflecting the chamber efficiencies and resolution. The chamber efficiencies that go into the simulation are determined from data. There existed the option to introduce the effect of the magnetic field as a $p_{tkick} = 0.821\ GeV/c$ or to read in a real field map and to integrate the deflections of the particles in small steps. Studies have shown the differences in the two approaches to be negligible.

In order to simulate the noise associated with chamber hits, Monte-Carlo events were overlaid on to data events. Care was taken to remove the additional RPC hits in the data prior to the overlay. So the muons as defined by the RPC's remain the ones generated by the Monte-Carlo. The overlay technique may have the effect of throwing away events where the overlaid event results in high hit multiplicity (close to the maximum hit rejection limit). Or it may keep an otherwise bad event where the additional hits from the data may help in the survival of a track with lower hits than demanded by the tracking program. Studies showed, however that these effects have a negligible impact on the overall acceptance.

Since all process generation is done in Pythia as a simple $2 \rightarrow 2$ and $2 \rightarrow 1$ hard subprocess, it is necessary to understand how this relates to reality. The structure function $f_i^a(x, Q^2)$ parametrizes the probability to find a parton $i$ with a fraction $x$ of the beam energy in the beam particle $a$ when probed by a hard scattering at the scale $Q^2$. The normalisation condition for which is written as, $\sum_i \int_0^1 dx\ x\ f_i^a(x, Q^2) \equiv 1$.

Various sets of such structure functions are available for nucleons, with the default in PYTHIA set to be the EHLQ (set 1) which has only the leading-order effects. It needs to be noted that only the Born-level matrix elements are used in the program. Hence there is no need to use a higher-order structure function as there is no gain in accuracy in doing so.

Fragmentation is a process that occurs at long distances when QCD becomes strongly interacting and perturbation theory breaks down. In this regime, the colored partons are transformed into the colorless hadrons that we observe. Due to its non-perturbative nature, the fragmentation process is not calculable from first principles in QCD. Various phenomenological models have been developed of which the string fragmentation is one, and this is incorporated in JETSET as part of the 'Lund Model'. In these models the fragmentation process is described in terms of a few simple branchings such as, $jet \rightarrow hadron + remainder - jet\ etc.$, and for each level probabilistic rules are applied for the production of new flavours and the distribution of energy and momentum among the final products.

The generated event information is passed by PYTHIA to GEANT for a spectrometer simulation. Once the event has been propagated through the spectrometer and overlaid on a data event, the standard analysis code is used to reconstruct the event. At the DST level of analysis the cuts were chosen after studying their efficiency in suppressing the background. Some kinematic cuts were applied immediately following the event generation and before the event is passed on to the GEANT detector simulation. This was done to avoid propagating events which in all likelihood would be rejected by the kinematic cuts after passing through a full detector simulation and event reconstruction. Sets of 2000 events were then written out which were then fully tracked by the standard routines for further analysis. The kinematic cuts imposed after the generation on the event were:

- leading muon $P_t > 1.5\ GeV/c$
- invariant mass of the muon pair in the event $> 2.0\ GeV$
- the total momentum of the muons in the pair $P_1, P_2 > 15\ GeV/c$

### 9.1.1 Beauty

PYTHIA was used to generate the beauty quark pairs. This is achieved by setting the approriate switches in the PYTHIA common blocks that control event generation. The hadronisation of the quarks was done by JETSET. In the figure 9.1 we have plotted the $p_t$ distribution for beauty hadrons. A very small fraction ($< 5\%$) of the hadronisation results in baryons. The shape of the $p_t$ spectrum is the same for particle and anti-particle states.

Muons can result in the final state through the first generation semileptonic decays of the produced beauty mesons as well as from the sequential decays. In the Monte-Carlo generation and decay, default decay tables, reflecting the current measurements, were used to randomly select semileptonic decay channels. Figure 9.3 shows the $p_t$ spectrum for the muons from decays of the b hadrons. As is clearly visible the highest $p_t$ muon in the pair on the average has a harder spectrum than the second highest (next leading) muon in the pair. The longitudinal momentum also shows this behaviour.

There is also the phenomenon of mixing in the case of neutral B mesons. The

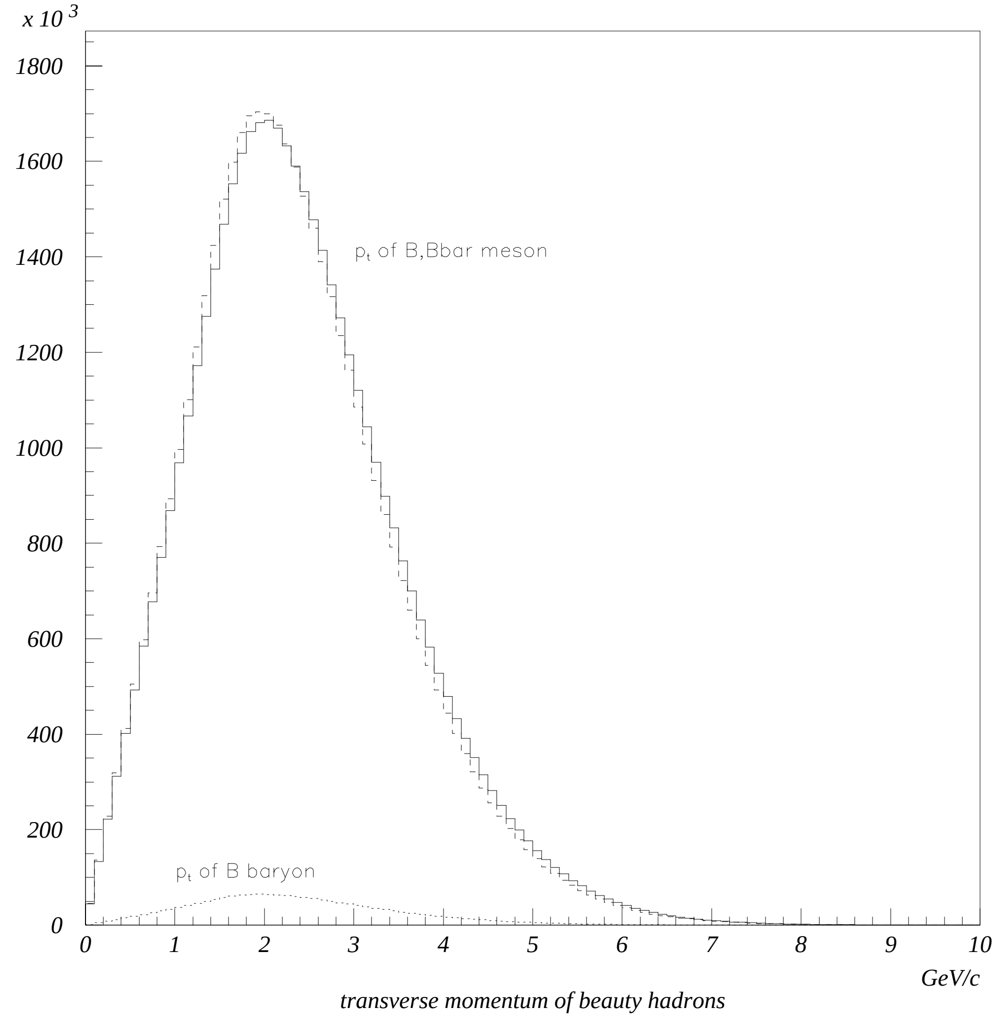

Figure 9.1: Beauty hadron transverse momentum spectrum solid lines are for particle and broken line for anti-particles spectrum for beauty baryons is shown as a dotted line

Momentum correlation at generation

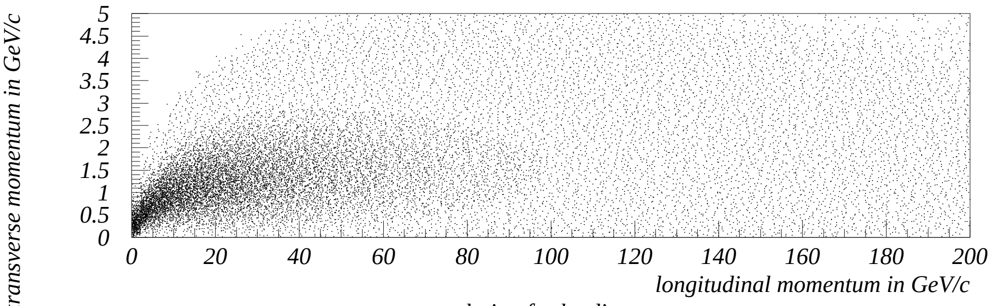

correlation for leading muon

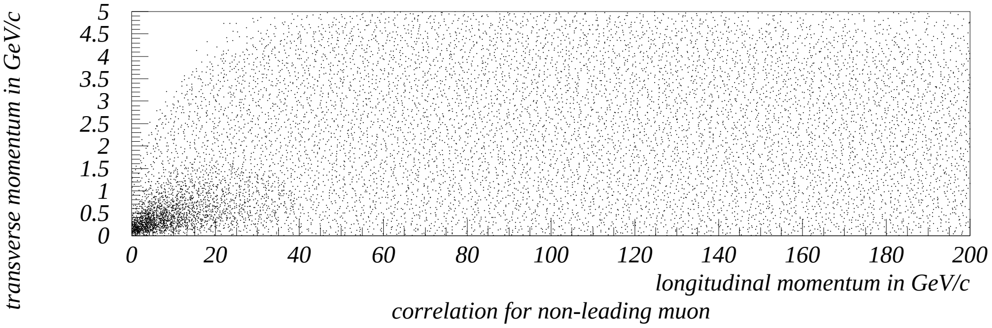

correlation for non-leading muon

Figure 9.2: Correlation plot of $p_t$ and $p_z$ for the muons from semileptonic beauty decays. The scatter plot was made for all events generated before any cuts are applied. The top plot corresponds to the leading muon in the event and the bottom plot for the mext-to-leading muon.

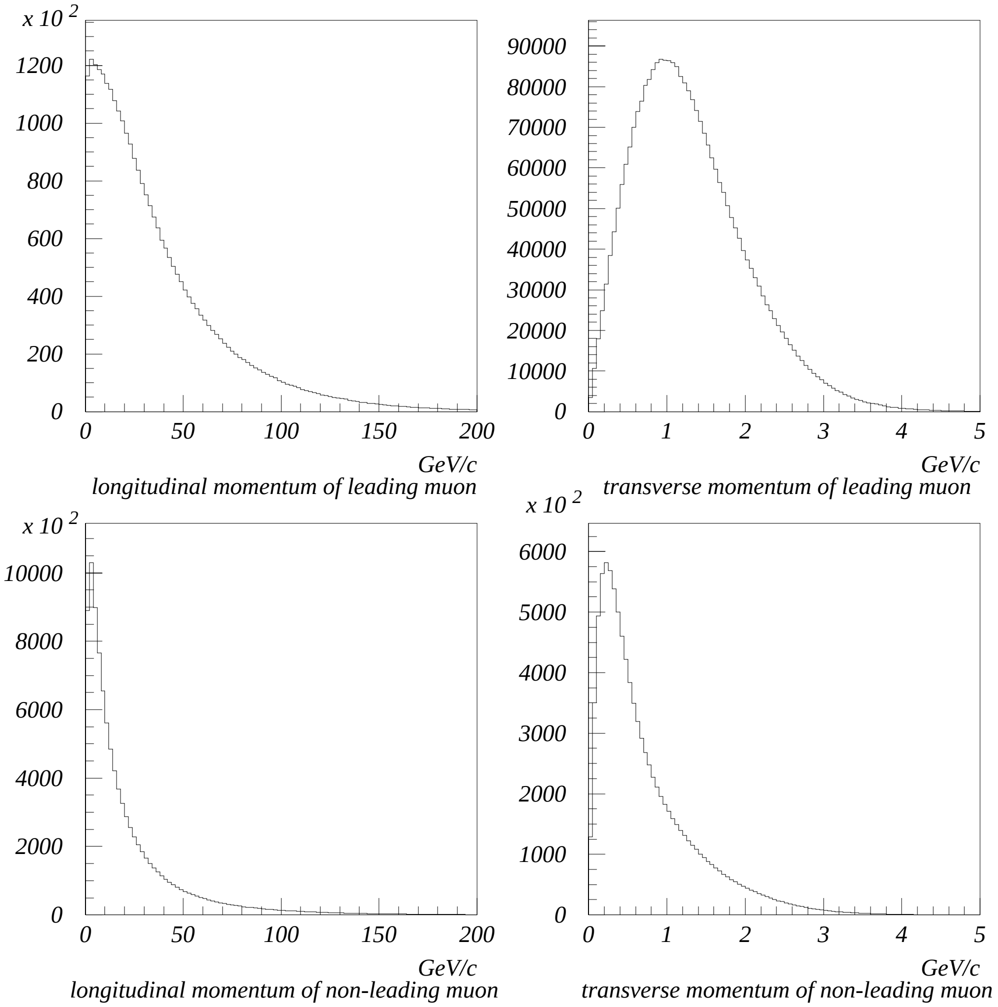

Figure 9.3: Beauty decays resulting in muons. This is a projection of the scatter plot shown in the pervious figure. The muon $p_t$ peaks at 1.5 GeV/c for the leading muon. The longitudinal spectrum indicates that a cut at 100 GeV/c would still retain most the muons from beauty decays.

$B^0$ before its decay may oscillate into a $\bar{B}^0$ and vice-versa. This has been experimentally observed and is usually parameterised in terms of the ratio of the CP-eigenstate mass difference of a $B^0$ and $\bar{B}^0$ to the decay rate , . Mixing has been observed for $B_d^0$ and $B_s^0$.

$$X_{d/s} = \frac{\Delta M}{,} \tag{9.5}$$

This quantity is measured directly from the asymmetry in the decay rates into dileptons for the $B$ and $\bar{B}$, and is found to be 0.7 for $X_d$ and greater than 10 is expected from the standard model for $X_s$. This means that the $B_s$ will mix thoroughly before it decays whereas in the case of the $B_d$ there is a competition between decay and mixing. Due to mixing like sign events can result from the first generation semileptonic decays of both the B's produced. If both of the $B^0$ mixes in the event and they decay semileptonically, then this results in an unlike sign event instead. From the numbers for the first generation decays, mixing occurs at the 20% level counting events in the like sign category. PYTHIA allows for the possibility of mixing.

From the breakdown of events given in figure 9.4 one can see the various sources that make a muon pair with opposite sign or same sign events from $B\bar{B}$ decays. These percentages come from a MC sample of 20,000 events. Approximately 48% of the events have both muons as a direct decay product of the parent beauty hadron. In 36% of the events at least one muon is from a parent charm hadron and in 8% of the cases both the muons have their parent as charm.

The remainder of events are presumabaly cases where at least one muon is as a result of strange decays after the first generation decay of a beauty particle into a kaon. This last sample is not included in the breakdown plots. In the figure 9.4 'bc' indicates that the leading muon originated from a beauty decay and the non-leading

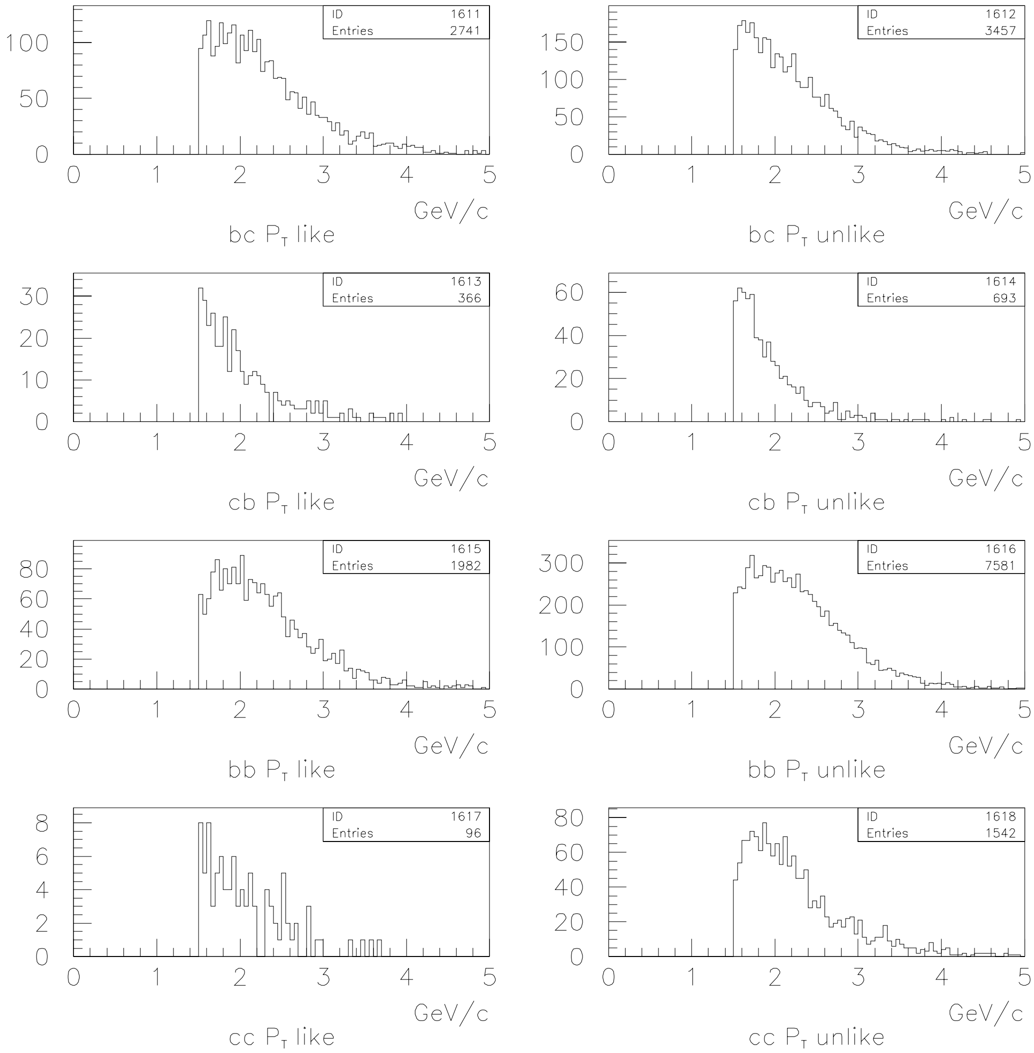

Figure 9.4: Beauty decays breakdown in terms of sign of muon pair. In the nomenclature used here the leading muon's parent is indicated first followed by the next-to-leading muon's parent. All events correspond to a total of 20,000 events accepted by the trigger configuration. Almost half the events that are accepted by the trigger come from direct beauty decays. The rest are from cascade decays of the beauty to charm and a subsequent semileptonic decay.

muon came from a charm decay.

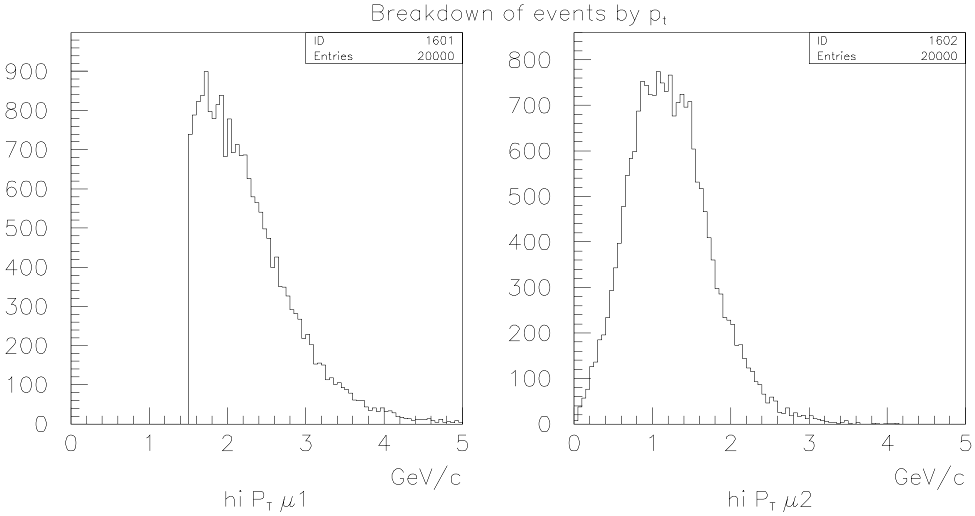

Figure 9.5: Beauty decays in terms of lead pt of the muon pair. The first plot is for the leading muon and the second one is for the non-leading muon. These muons have been accepted by the trigger but reconstruction efficiencies are not yet folded in at this point. A full breakdown of these events is presented in the next figure.

### 9.1.2 Charm

In the case of the charm Monte-Carlo, after the generation of the $d\bar{d}$ pair and the subsequent hadronisation of the quarks, the charm pairs are forced to decay semileptonically:

$$D \rightarrow \mu^+ X \qquad \bar{D} \rightarrow \mu^- X \tag{9.6}$$

The average (over neutral and charged D's) semimuonic branching ratio is around 10%.

To date the cross-section measurements for charm production in high energy

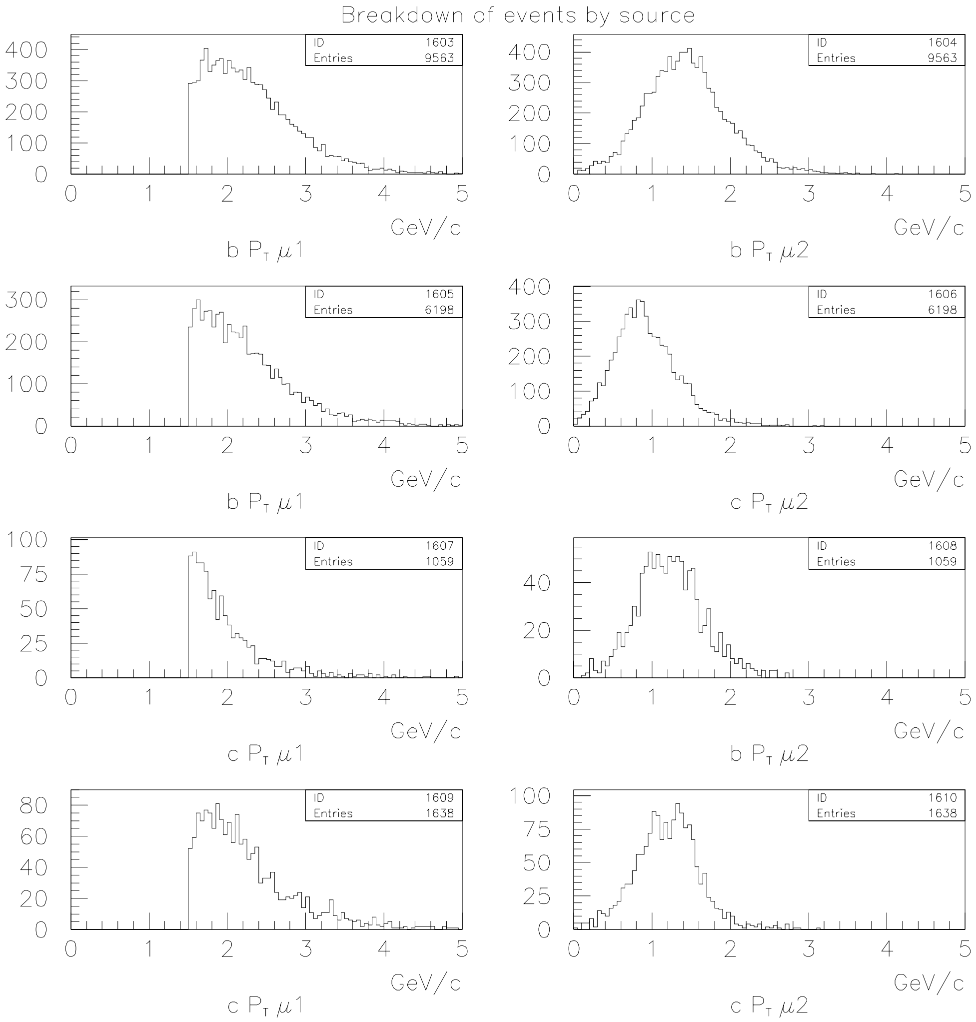

Figure 9.6: Beauty decays breakdown in terms of the leading($\mu 1$) and non-leading($\mu 2$) $p_t$ muon in the pair. The parent of the muon is also indicated in each case. The first row corresponds to the case where both the muons are from direct beauty decays. The last row shows the distribution when both muons in the pair originate in charm which is the immediate daughter of the beauty decay.

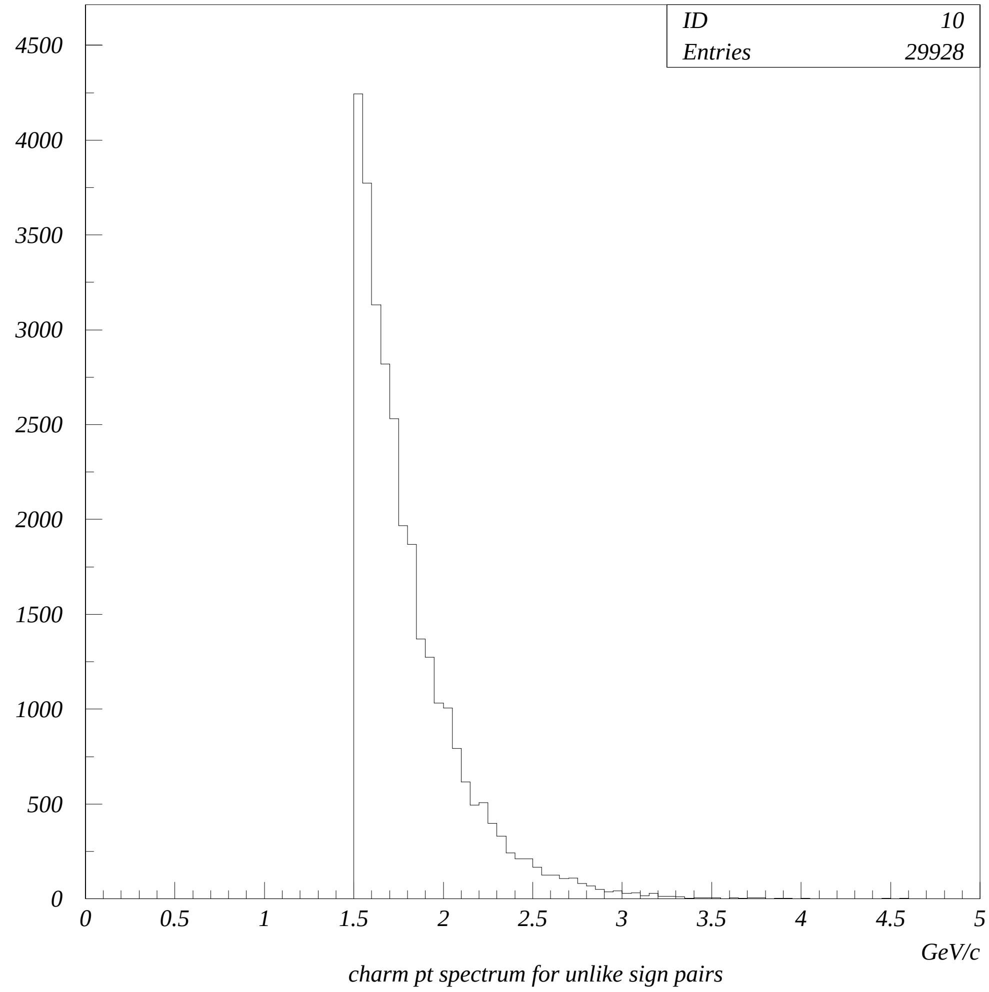

Figure 9.7: Direct production of charm and its semileptonic decay is our most dominant background. The $p_t$ spectrum of the leading muon for unlike sign pairs is shown here. There is a long tail even beyond 2 $GeV/c$.

| decay mode | branching ratio |
|---|---|
| $D^+ \rightarrow \bar{K}^0 \mu^+ \nu_\mu$ | $(7.0^{+3.0}_{-2.0})\%$ |
| $D^+ \rightarrow K^- \pi^+ \mu^+ \nu_\mu$ | $(3.2 \pm 1.7)\%$ |
| $D^+ \rightarrow \bar{K}^{*0} \mu^+ \nu_\mu$ | $(3.0 \pm 0.4)\%$ |
| charged D total<br>$D^+ \rightarrow \mu^+ \ X$ | $(10.2 \pm 3.5)\%$ |
| neutral D<br>$D^0 \rightarrow \mu^+ \ X$ | $(10.0 \pm 2.6)\%$ |
| inclusive D decay<br>(semileptonic)<br>$D \rightarrow \mu^+ \ X$ | $(10.1 \pm 4.4)\%$ |

Table 9.1: Summary of semileptonic D decay branching ratio used from Phys. Rev. D, Vol.50 Number 3, Review of Particle Properties

| experiment | cross-section/nucleon |
|---|---|
| E653 | $(38 \pm 3 \pm 13)\mu barn$ |
| E743 | $(22^{+9}_{-7} \pm 5.5)\mu barn$ |
| E789 | $(17.7 \pm 0.9 \pm 3.4)\mu barn$ |

Table 9.2: $D^0\bar{D}^0$ cross-section measurements with 900 $GeV/c$ proton beam from Phys. Rev. Letters Vol. 72 Number 16, Page 2542

hadronic interactions suffer from low statistics and large sytematic errors. Very early measurements are characterised by order-of-magnitude discrepancies. It needs to be noted that our analysis is sensitive to the value of the cross section. We chose to use the E653 value as the measured value in their case is over a larger acceptance region than was the case with E789. Taking the value as quoted by Mangano et. al. [27] $\sigma(pN \rightarrow D\bar{D}) = 38 \pm 10$ $\mu barns/nucleon$.

### 9.1.3 $J/\psi$

In the data we exclude the $J/\psi$ by imposing a dimuon mass cut in the region $2.9 < mass < 3.3$ $GeV/c^2$. This is done for both the unlike sign sample as well as the like sign sample. In principle the directly produced $J/\psi$'s should have zero impact parameter with respect to the primary vertex. However the data includes a significant number of $J/\psi$'s with non-zero impact parameter, and this number seems higher than what one would expect for $J/\psi$ from beauty decays. Given the questionable impact parameter (even after retaining only those tracks which have a $10\sigma$ significance for the impact parameter) it is also important to consider the possibility of mismeasured $J/\psi$'s outside of the mass window - surviving in the final signal sample.

To estimate this leakage outside of the mass window the data in this mass region were fit to a double gaussian of widths 42 $GeV/c^2$ and 86 $GeV/c^2$. Based on these experimetally determined widths, the amount of the $J/\psi$'s outside of the mass window was estimated:

$$M_{\mu\mu} > 2\ GeV/c^2 \quad : \quad 223.6\ events \tag{9.7}$$

$$2.9 < M_{\mu\mu} < 3.3\ GeV/c^2 \quad : \quad 222.0\ events \tag{9.8}$$

Hence, the correction for $J/\psi$ is given as $\frac{1.6}{223.6}$ which results in a small value of 0.007 for the fraction of the total events in the $J/\psi$ region contributing to the background. The fit values are given in figure 9.8

### 9.1.4 Drell-Yan

To estimate the contribution from Drell-Yan a Monte Carlo generator, based on the E772 measurement [1] was adapted for use with the E771 spectrometer (GEANT) simulation. The idea is to use the differential cross-section measurement made by E772 integrated for the $x_f$ region $(0.1-0.3)$, for 1 $GeV/c^2$ wide mass bins in the

---

[1] Private Communication, Chuck Brown

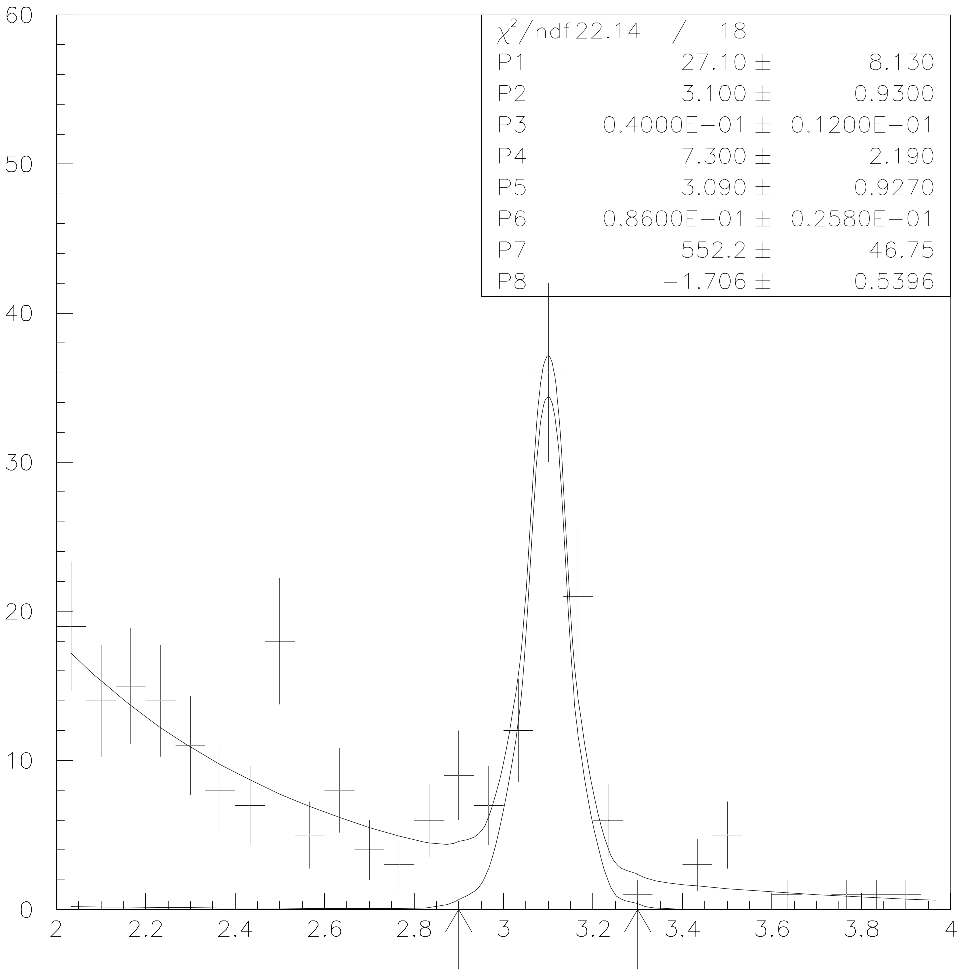

Figure 9.8: Mass spectrum fit in the $J/\psi$ region. The peak region is fit to a sum of two gaussians with sigmas of 40 MeV and 86 MeV. The arrows indicate the mass window used to define the $J/\psi$ region. The background is fit to a polynomial. The gaussian fit is used to estimate the leakage of $J/\psi$ events outside of the mass window after reconstruction of the muon tracks due to smearing. This background contribution is much smaller than that from charm decays.

region (5.5−14.5) $GeV/c^2$ and $p_t$ bins of 0.250 GeV/c in the window (0.125−3.875). The values were integrated for all $p_t$ and mass bins to get the cross-section in this limited region. From the E771 measured value and using their parameterisation the total cross-section for all kinematically allowed $x_f$, mass and $p_t$ is inferred by comparing the Monte Carlo distribution with the measured values. Based on the knowledge of the beam flux for the E771 data sample and the cross-section as predicted by the normalised Monte Carlo value, the number of produced Drell-Yan events can be estimated. The trigger and the geometric acceptance fractions were determined from a full GEANT simulation. The reconstruction efficiencies are applied when the MC events were overlaid with data, and later the analysis cuts were applied to the reconstructed Drell-Yan events. The weighted number of events surviving these cuts yielded the contamination in the unlike sign sample due to the Drell-Yan production.

The Drell-Yan program throws events using a flat distribution in the mass range 1.0 GeV/c$^2$ to 16.0 GeV/c$^2$. For the dimuon production distribution, the Moreno, McGaughey et al. [2] measurement was used.

$$f(\theta) = sin\theta \; (1 + cos^2\theta) \tag{9.9}$$

For the $x_f$ distribution a Gaussian with a slight offset of 0.5 was used, shown in figure 9.9. From the value for the $x_f$ $x_1$ and $x_2$ are calculated:

$$x_1 = 0.5x_f + \sqrt{0.25x_f^2 + \tau} \tag{9.10}$$

---

[2] McGaughey et.al. Phys.Rev.D Vol 50, No 5, Sept. 1994, 3038

where

$$\tau = \frac{M_{\mu+\mu-}{}^2}{(2m_{proton}{}^2 + 2m_{proton}\sqrt{p_{proton}{}^2 + m_{proton}{}^2})} \tag{9.11}$$

The distribution in $p_t$ is given by the Kaplan formula,

$$p_t = 3\sqrt{\frac{1}{(ran)^{0.2}} - 1} \tag{9.12}$$

where *ran* is a pseudo-random number over the range $[0,1]$. For each muon pair generated flat in the mass, a weight is calculated using the lowest tree-level contribution to the Drell-Yan cross-section calculated from first principles and convoluting it with the parton distributions for the colliding protons. The MRSD0 set of structure functions were used in the generator, although a different set could have been chaosen via the PDFLIB set of library call.

The Drell-Yan cross-section is given by,

$$M^3\frac{d^2\sigma}{dMdx_f} = K\frac{8\pi\alpha^2}{9}\frac{x_1x_2}{x_1+x_2}\sum_i e_i{}^2[q_i(x_1)\overline{q_i}(x_2) + \overline{q_i}(x_1)q_i(x_2)] \tag{9.13}$$

where K is 0.39 $GeV^2$ mbarn.

To calculate the final weight for each event, the initial $x_f$ gaussian distribution that was unweighted as the cross-section formula already has the correct $x_f$ distribution included in it.

### 9.1.5 Drell-Yan Cross Section

From the E772 data sample [91] the cross-section in the region $0.1 < x_f < 0.3$ , $5.5 < M_{\mu+\mu-} < 14.5$ and for the transverse momentum $0.125 < p_t < 3.875$ can be

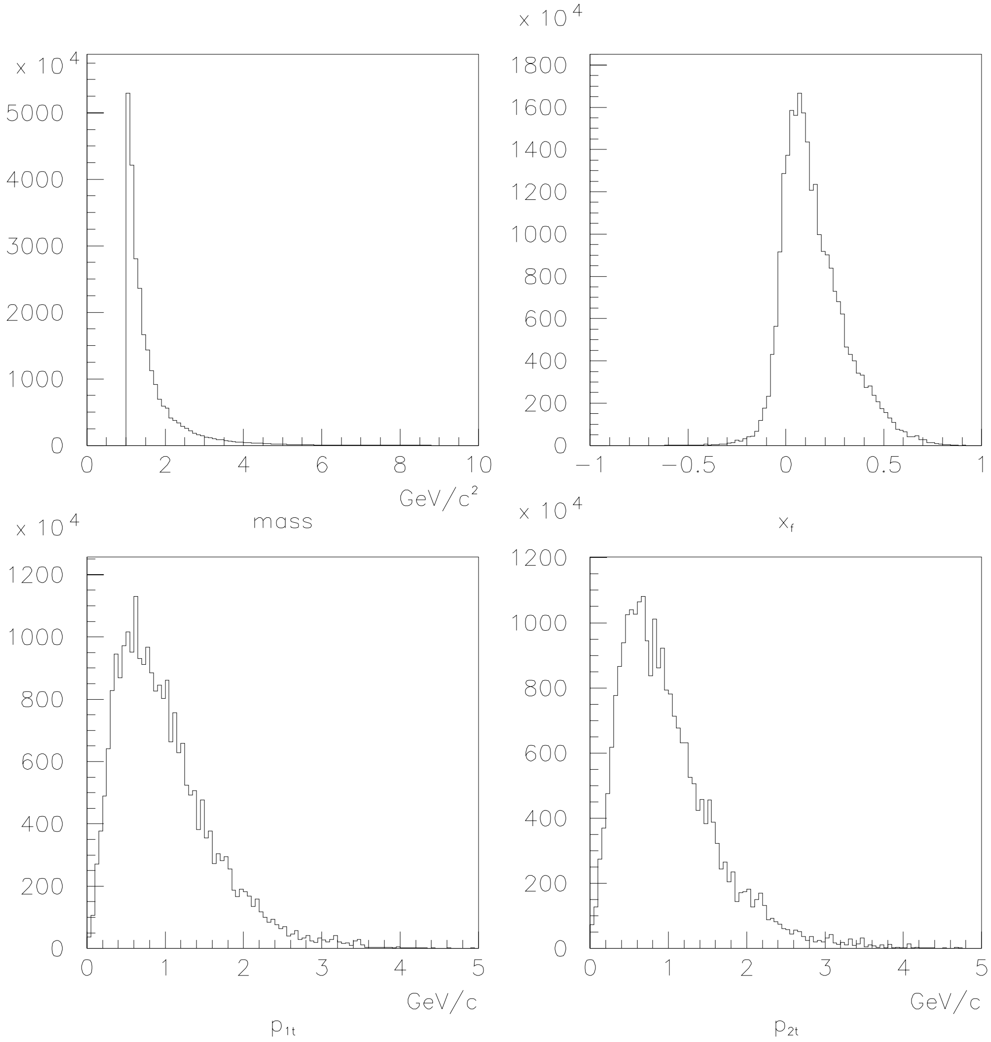

Figure 9.9: Drell Yan production distributions used in the Monte-Carlo. The distribution are all weighted by the cross-section as described inthe text. trigger acceptance and reconstruction efficiencies have not yet been applied. Again, here $p_{1t}$ and $p_{2t}$ indicates the leading and next-to-leading muon in the event.

summarised as a differential cross section:

$$M^3_{\mu^+\mu^-}\frac{d^2\sigma}{dM_{\mu^+\mu^-}dx_f} \tag{9.14}$$

with mass bins 1 $GeV/c^2$ wide, $p_t$ bins 0.125 GeV/c wide. After removing the $M^3$ dependence and doing the sums correctly, one obtains for the cross section per nucleon, $\Delta\sigma = (64.20 \pm 1.09)$ $pbarn$ in the restricted region described above.

The Monte-Carlo used to generate Drell-Yan events employed the following cuts:

$$\begin{aligned} P_L(1,2) &> 10\ GeV/c && (9.15)\\ x_1 &< 0.99 && (9.16)\\ x_2 &> 0.005 && (9.17)\\ 1.0 &< M_{\mu^+\mu^-} < 16.0\ GeV/c^2 && (9.18)\end{aligned}$$

where $P_L(1,2)$ refers to the longitudinal momentum of either muons. The number of events (N) with these restrictions was determined by summing all weights for events generated in this region. The same procedure done led to another number $\Delta N$ which satisfied the cuts in $p_t$, $M_{\mu^+\mu^-}$ and $x_f$. The cross section was then determined for Drell-Yan events generated by the relation given below,

$$\frac{\Delta N}{N} = \frac{\Delta\sigma}{\sigma} \tag{9.19}$$

Hence the cross section in the generated region is

$$\sigma_{Drell-Yan} = (13.66 \pm 0.23)\ nanobarn/nucleon \tag{9.20}$$

### 9.1.6 Production Rates

Table 9.1.6 summarises the expected number of events for the various physics processes after the application of the initial kinematic cuts and also takes into account the detector acceptance. The trigger acceptance is also folded in this number. The only efficiency not included at this point is the reconstruction efficiency from tracking, and this will be addressed shortly. Included in the table is a correction factor for the number of events expected after all the cuts are applied to the sample of monte-carlo events. This factor normalises the events reconstructed to the number of events of each type produced in E771, given the cross section for the process.

The number of events expected on tape is calculated from,

$$live\ Beam \times interaction\ length \times \frac{\sigma \times A}{\sigma(pN \to all) \times A^{0.72}} \times Acceptance \tag{9.21}$$

If the events are generated such that all the subsequent decays are forced to a particular mode then the branching ratio needs to be removed in order to predict the number of events on tape.

| | |
|---|---|
| $\sigma(pN \rightarrow all)$ | $= 40\ millibarns/nucleon$ |
| Live Beam | $= 1.23 \times 10^{13}\ protons$ |

| process | $B\bar{B}$ | $D\bar{D}$ | Drell-Yan |
|---|---|---|---|
| $\sigma/nucleon$ | $10\ nbarns$ | $38 \pm 10\ \mu barns$ | $(13.66 \pm 0.23)\ nbarns$ |
| $\frac{\sigma \times A}{\sigma(pN \rightarrow all) \times A^{0.72}}$ | $6.35 \times 10^{-7}$ | $2.543 \times 10^{-3}$ | $0.056 \times 10^{7}$ |
| events produced | $4.06 \times 10^{5}$ | $16.265 \times 10^{8}$ | $0.056 \times 10^{7}$ |
| Acceptance | $(7.52 \pm 0.05) \times 10^{-4}$ | $(1.201 \pm 0.006) \times 10^{-4}$ | 0.00924 |
| events on tape | 305.3 | 3710 | 5174 |
| events generated | 26.6 million | 333.07 million | |
| events reconstructed | 18000 | 30000 | $2.8892 \times 10^{6}$ |
| correction factor | $0.0170 \pm 0.0001$ | $0.124 \pm 0.002$ | 0.0018 |

Table 9.3: Summary of the correction factor that needs to be folded in for Monte Carlo events generated. It is basically a cross section times spectrometer acceptance correction.

## 9.2 Beam Estimate

Analysis was restricted to tapesets in the range from 20238 to 20361 with the exclusion of three tapesets where the DST tapes contain no events. These three tapesets are 20238, 20317 and 20344. Excluding these three tapesets on the assumption that they were inadvertantly omitted during one of the data processing passes, the total live beam that is relevant to our analysis is $1.23 \times 10^{13}$ with a 2.35% error [73]. If the three tapesets had been included in the beam estimate, then the total number would be $1.26 \times 10^{13}$. The beam estimate includes corrections for each tapeset the time dependency of the efficiency of the beam planes as they were used to measure the flux. The average efficiency for the entire run was around 90%. Corrections were also included for lost tapes, incomplete tapes and for cases where there was disagreement between the scaler sum value of the dimuon triggers written to tape and the number of dimuon triggers read from these tapes. A further correction due to the multiplicity cut was also applied. Most of these high multiplicity events were due to events with multiple beam tracks and in all likelihood were triggered by pion decays.

## 9.3 Vertex Efficiency

The overlay technique simply used the primary vertex position from data events. The generated event then has the primary vertex identical to that of the underlying event. This means that when the overlaid event is reconstructed with our tracking program it is guaranteed to have a good primary vertex for every event. However in the actual data the primary vertex finding routine was found to be successful only 80% of the time. This number was more or less stable throughout the run.

Since, the DAC thresholds were changed in course of the run as the silicon efficiency dropped due to radiation damage, a sharp change of the DAC threshold setting is reflected in the vertex efficiency values. The algorithm used to find a vertex is covered extensively in [70].

A large sample of the good dimuon events, which had their invariant mass centered on the $J/\psi$ mass $\pm 200\ MeV/c^2$ was used to measure the primary vertex efficiency. These being mostly direct $J/\psi$'s, they should be associated with a good vertex. The invariant mass of the dimuon pairs in the event was based solely on the rear track information and assuming the center of the target foils. Events classified as $J/\psi$'s were then searched for the primary vertex. The ratio of the number of events that returned a good primary vertex to the total number of $J/\psi$ events processed is a measure of the vertex finding efficiency. Although it is possible that the $J/\psi$ could have come from upstream or downstream of the target foils, detailed investigation of failed events showed that the dominant failure in identifying a primary interaction was due to the presence of multiple interactions.

To estimate the number of beauty events a correction needs to be made for the primary vertex efficiency to all the final numbers of the Monte Carlo sample. This correction is independent of all other cuts and is based on a weighted average $80.9 \pm 0.12\%$ from all tapesets represented in the final DST.

## 9.4 Silicon Efficiency

The silicon efficiency used in the Monte Carlo studies was region dependent as well as tapeset dependent. Each plane was divided into three concentric regions about the beam center. The efficiencies were lowest (10%) in the central region and highest (80%) in the outer region. All the 12 planes of the silicon tracker were analyzed in the same manner. The data was divided into three distinct time periods, to track the time variation of the efficiencies.

It was subsequently discovered that this parameterisation overestimated the true efficiency value. This discovery stemmed from studies in which $J/\psi$'s were reconstructed under the two different tracking schemes. In the first scheme a number $N_{Rear}$ were reconstructed using only the rear tracking chamber information to form the muon pair that makes a $J/\psi$. In the second scheme a number $N_{Si+Rear}$ were reconstructed based on rear and silicon hit information. The average silicon efficiency as measured from the data is thus determined:

$$\epsilon_{Silicon} = \frac{N_{Si+Rear}}{N_{Rear}} \tag{9.22}$$

The ratio of the number of events with a $J/\psi$ in both these schemes for reconstruction gives a measure of the loss incurred in the silicon. This ratio needs to be applied to the MC events as well. These two numbers should be identical if the silicon efficiency parameterisation is close to the real value. We see a difference, and hence this should be applied as a further correction and this is included in the final summary table. The correction is defined as

$$\delta\epsilon = \frac{\epsilon^{Overlay}}{\epsilon^{data}} \tag{9.23}$$

This correction can be determined in two ways depending on how one decides to count the number of reconstructed $J/\psi$'s. When only the rear track information is used to construct the invariant mass the side bands outside the $\pm 200$ $MeV/c^2$ mass region is more prominent than in the case when additional silicon hits are also used to determine the muon tracks. The side band can be used as a measure of the

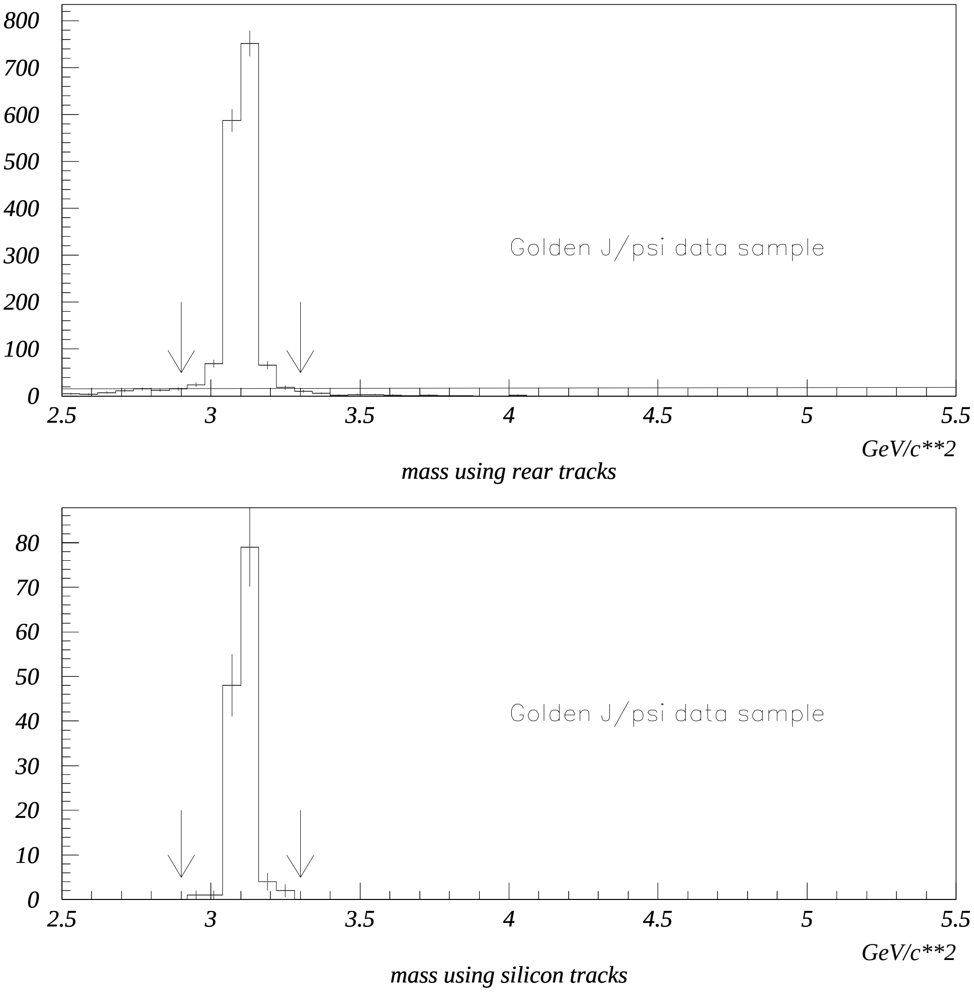

Figure 9.10: Reconstructed $J/\psi$ from the data using tracks without silicon hit information is shown in the top plot. The bottom plot shows the distribution when silicon hits are also used to construct the muon tracks. The arrows indicate the mass window used to define the $J/\psi$ events.

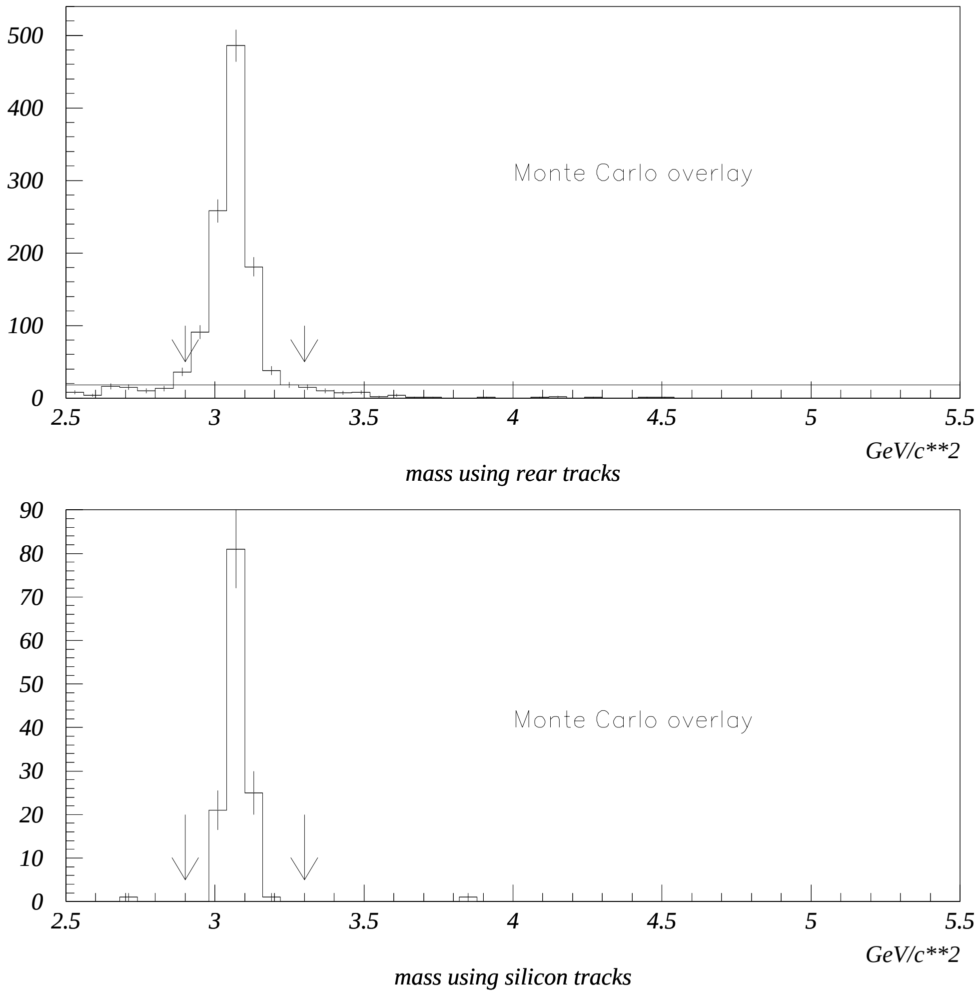

Figure 9.11: Reconstructed $J/\psi$ from the Monte Carlo overlay sample using tracks without silicon hit information is shown in the top plot. The bottom plot has the silicon hits also used to construct the muon tracks. The arrows indicate the mass window used to define the $J/\psi$ events.

|  | $N_{Rear}$ |  |  | $N_{Si+Rear}$ |
|---|---|---|---|---|
|  | Total $J/\psi$ | Bkgrd. | $J/\psi$ above Bkgrd. | $J/\psi$ with Silicon |
| Data | 1515 | 75 | 1440 | 135 |
| $J/\psi$ MC overlay | 1108 | 182 | 926 | 128 |
| $\delta\epsilon_1$ | 1.30 |  |  |  |
| $\delta\epsilon_2$ | 1.47 |  |  |  |
| $\delta\epsilon_{average}$ | $1.39 \pm 0.12$ |  |  |  |

Table 9.4: Silicon efficiency correction summary

background that needs to be subtracted from the peak region. This background is indicated as a horizontal line in the figures 9.11 and 9.10. The peak region is marked by arrows. Table 9.4 below summarises the correction estimate made with and without the background subtraction. This is done to obtain a measure of the spread in the correction to be made, and thus an estimate of the systematic error remaining after the correction is applied.

## 9.5 Selection of Cuts

The list of cuts used in the analysis are :

**cut 1** $2.0 < M_{\mu\mu} < 2.9\ GeV/c^2$ , $M_{\mu\mu} > 3.3\ GeV/c^2$

**cut 2** leading muon in pair $p_t > 1.5\ GeV/c^2$, non-leading muon $p_t > 1.0\ GeV/c^2$

**cut 3** cut on the number of Silicon hits on each muon track in the pair. We require more than 3 hits in each projection x and y for both the tracks in the pair.

**cut 4** require at least 5 hits in x projection in the front chambers for both the tracks and more than 10 hits in the y projection for both the tracks in the pair.

**cut 5** absolute value of the ratio of the impact parameter of the muon tracks with respect to the primary vertex in the x projection and its error must be greater than 3.

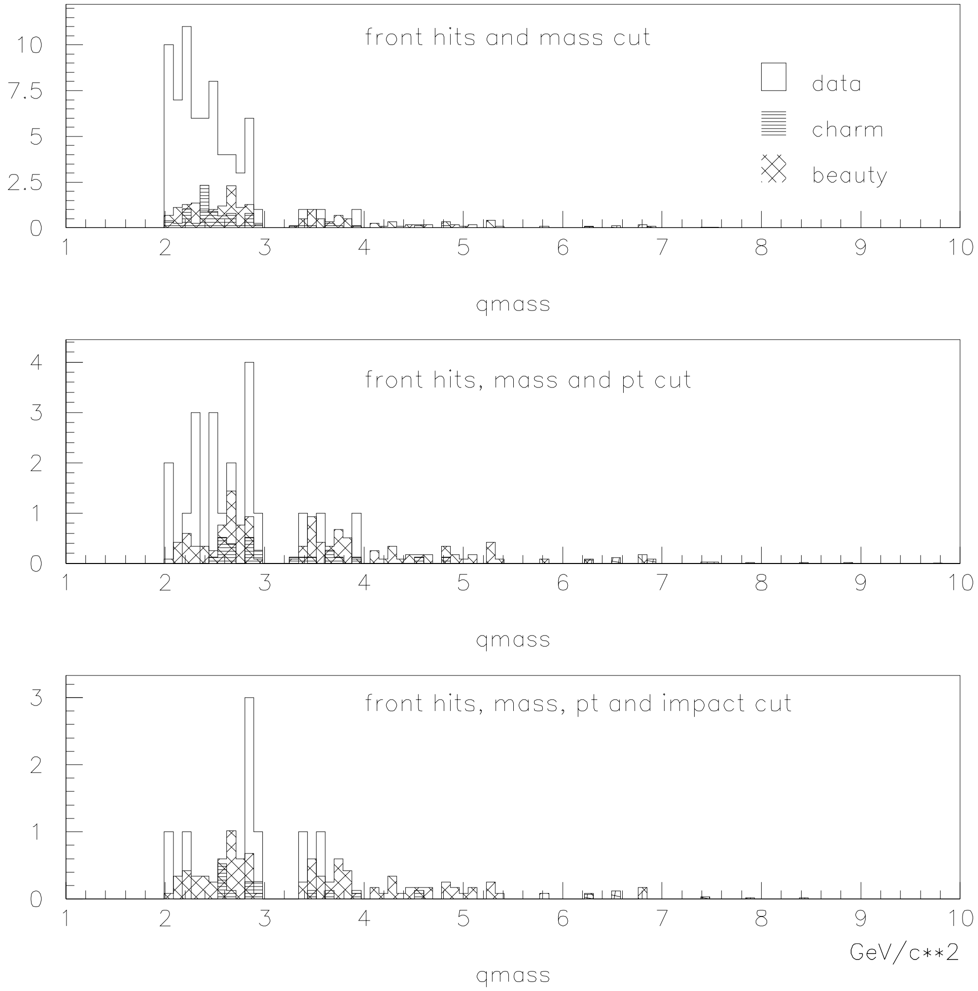

Figure 9.12: Mass distribution for the leading muon pair in a given event. The progression in cuts is indicated in the text for each plot. One can clearly see the effect of increasing the $p_t$ cut on the second muon track.

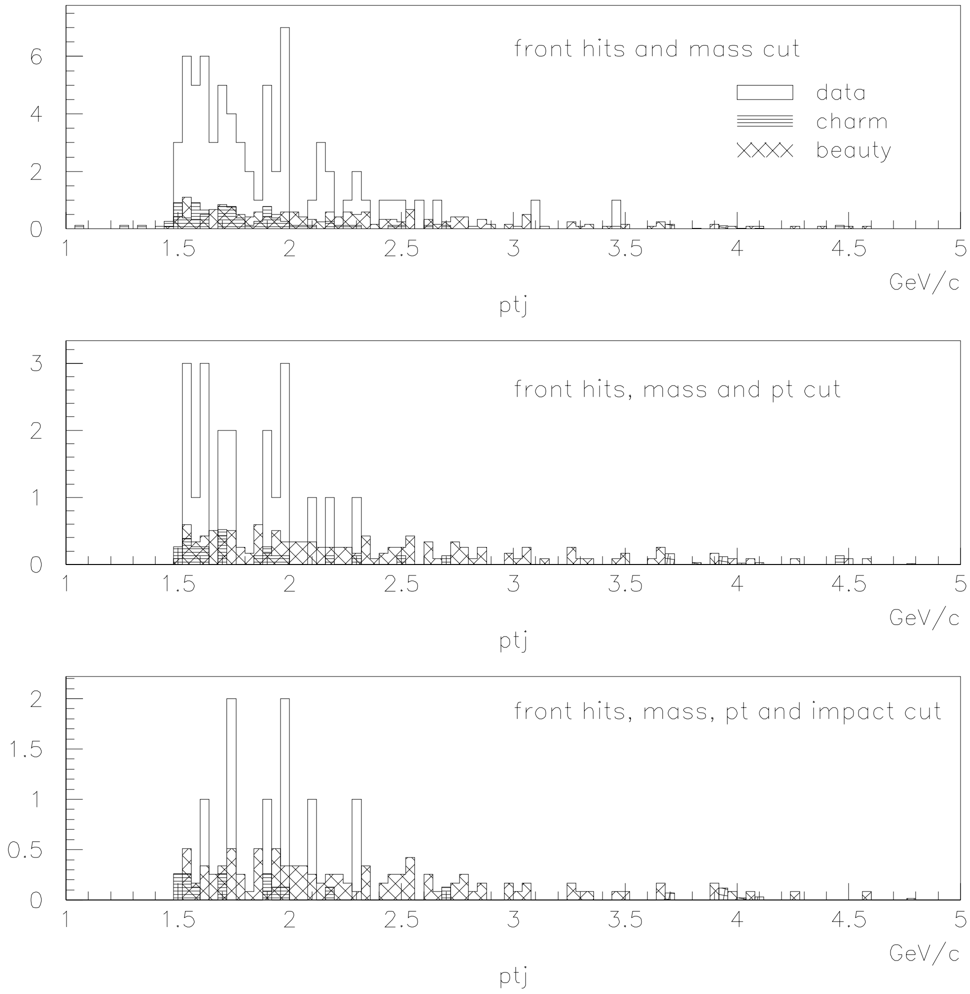

Figure 9.13: The distributin for the highest $p_t$ muon in the pair.

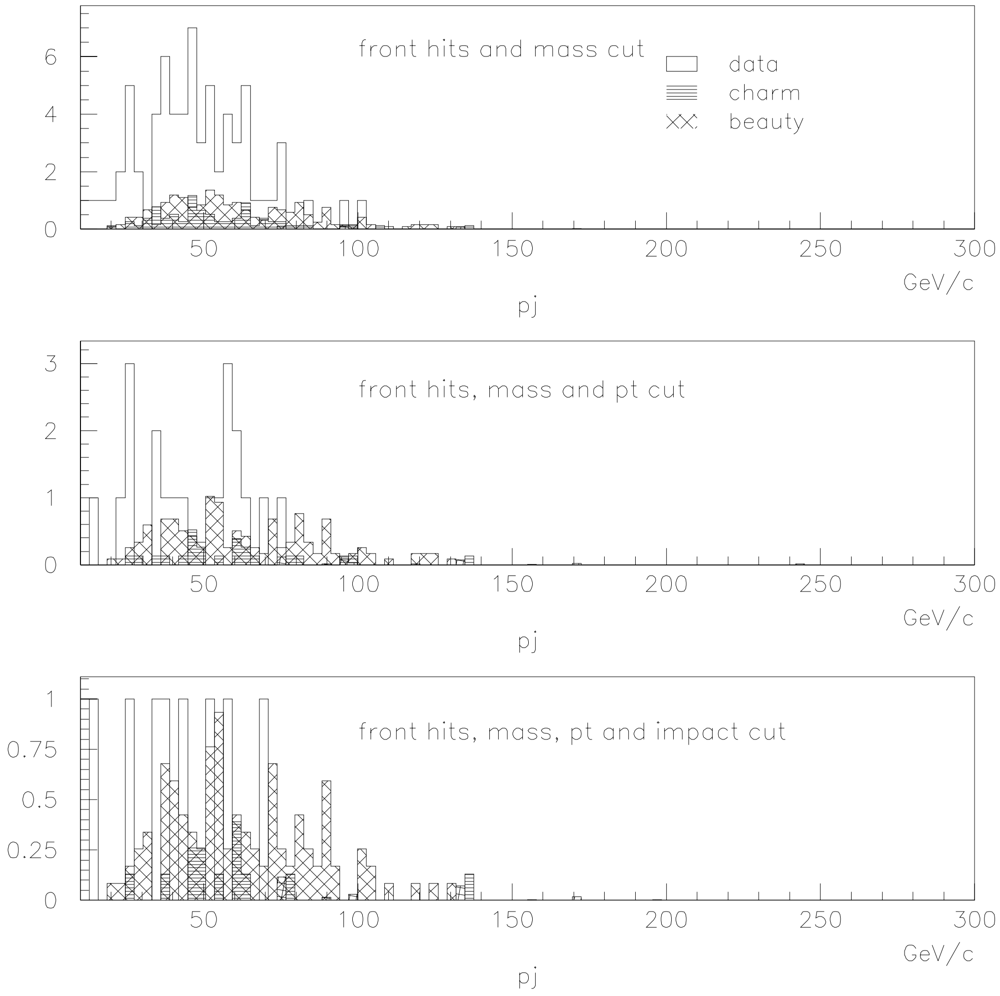

Figure 9.14: Shown here is the distribution for the total momentum of the leading muon in the pair.

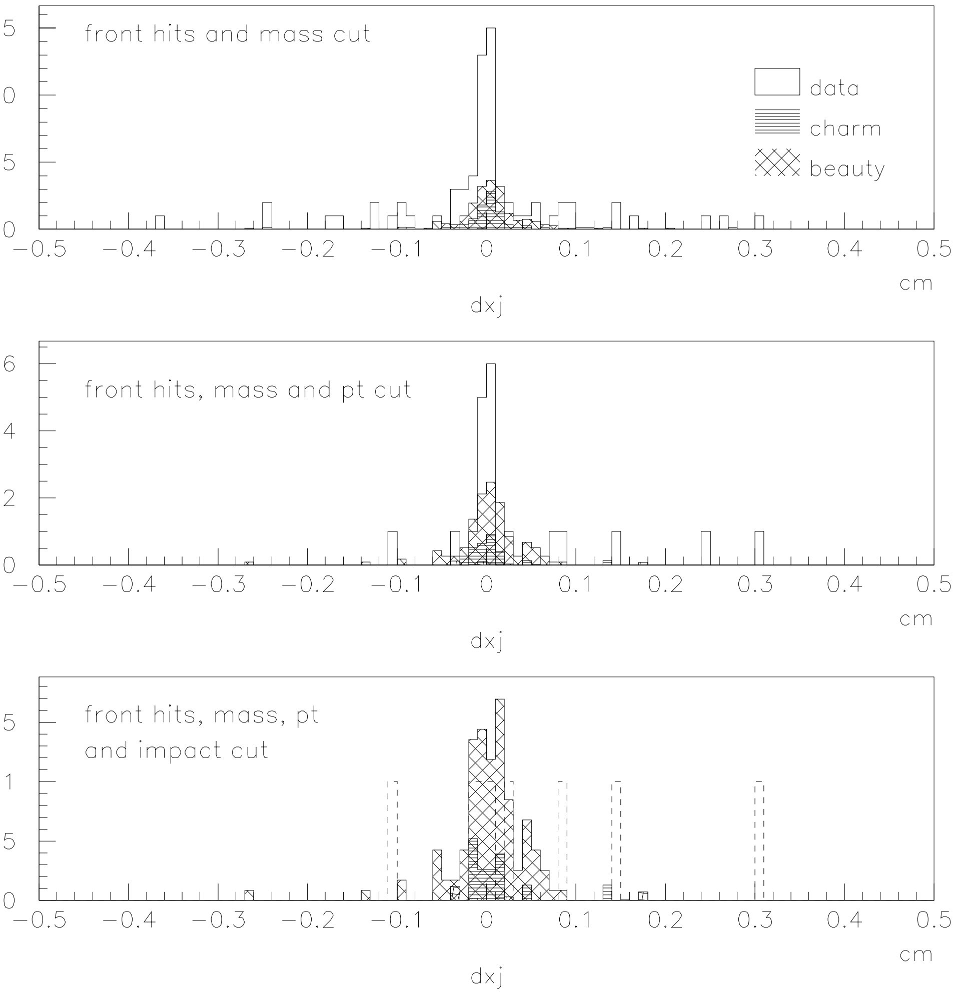

Figure 9.15: Impact parameter in projection x for the leading muon of the selected pair. In the monte-carlo we see that for beauty events the values for the impact parrameter is below 1mm, though in the data we have one event which has a very large impact parameter.

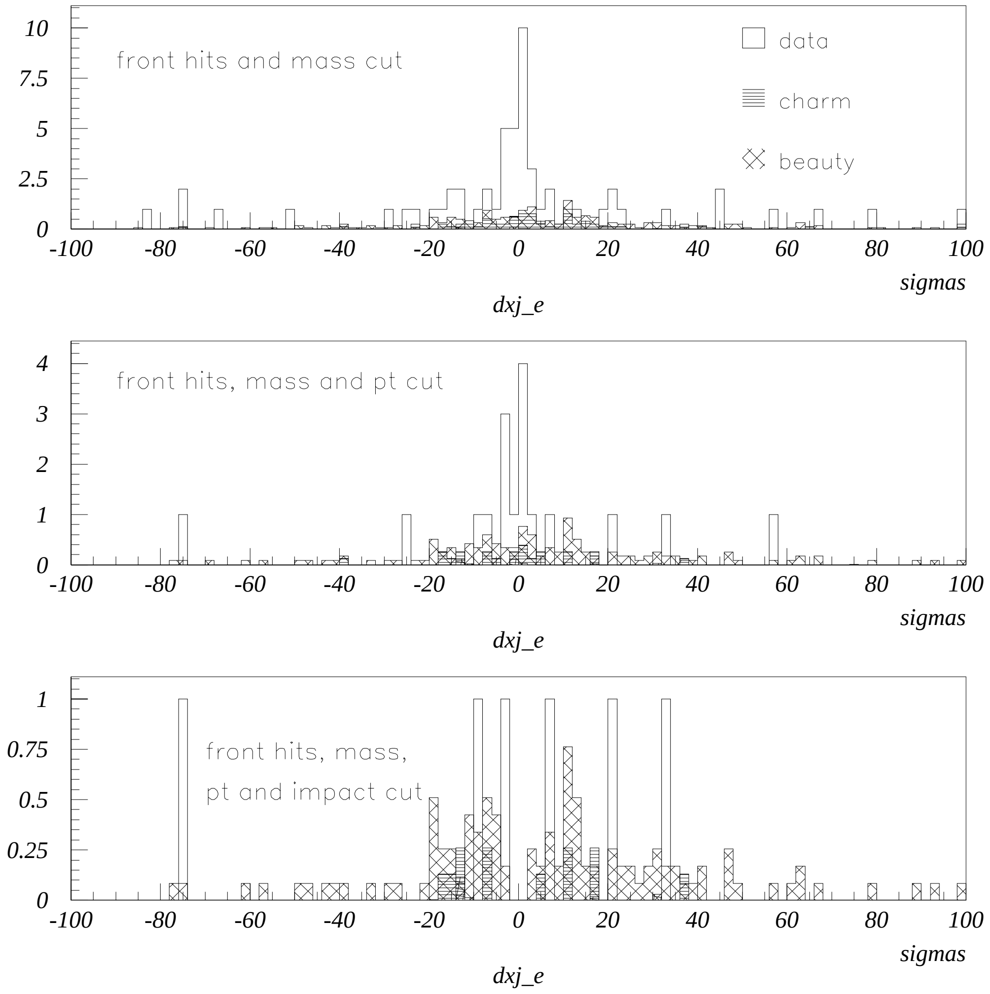

Figure 9.16: Impact parameter distribution in number of sigmas for the leading muon. The $3\sigma$ cut is evident in the last plot.

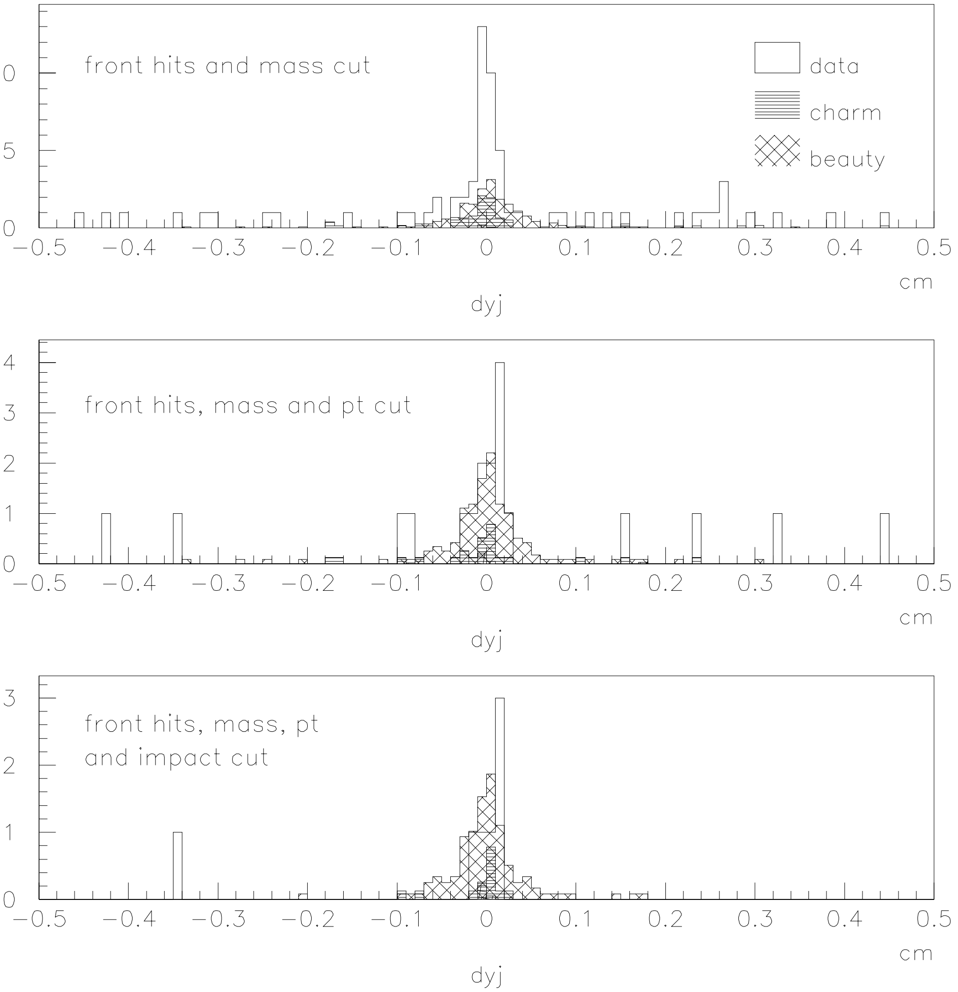

Figure 9.17: Impact parameter distribution for the leading muon in the y projection.

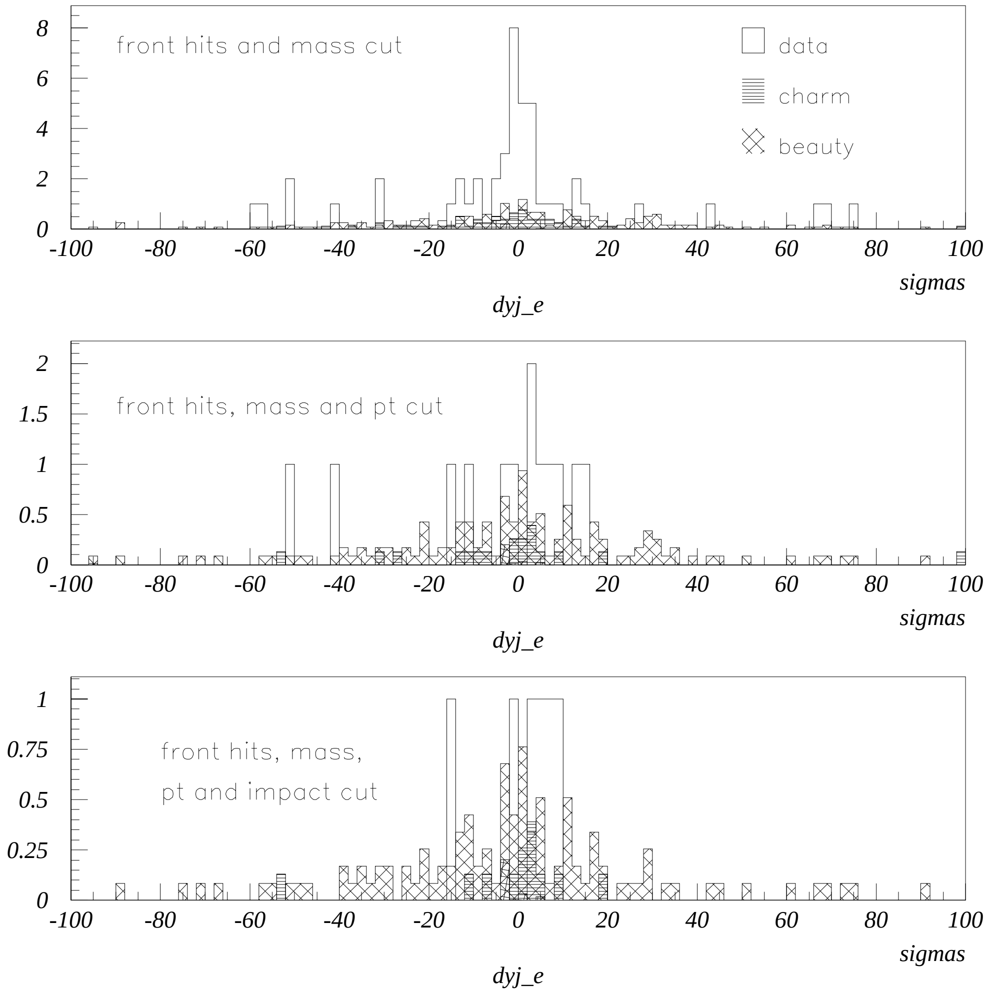

Figure 9.18: Impact parameter distribution for the leading muon in the y projection given in number of sigmas.

| Cuts | Data | | Monte-Carlo | | Backgrounds | | | | |
|---|---|---|---|---|---|---|---|---|---|
| | | | $\sigma_{B\bar{B}}$ $(10nb)$ | | $\sigma_{D\bar{D}}$ $(38\mu b)$ | | $\sigma_{Drell-Yan}$ $(14nb)$ | $J/\psi$ mismeasured | |
| track quality | 252 | 169 | 469 | 243 | 281 | 35 | 25375 | | |
| front hits | 66 | 30 | 239 | 100 | 90 | 6 | 1960 | | |
| mass | 41 | 28 | 160 | 64 | 67 | 2 | 230 | 23 | 2 |
| $p_t$ | 13 | 7 | 109 | 36 | 23 | 0 | 230 | 21 | 2 |
| impact | 7 | 1 | 89 | 27 | 13 | 0 | 147 | 15 | 0 |
| scan | 5 | 1 | all monte-carlo events survive this cut | | | | | | |
| correc. factor | | | 0.0169 $\pm 0.0001$ | | 0.124 $\pm 0.002$ | | $1.75 \times 10^{-3}$ $\pm 2.32 \times 10^{-3}$ | 0.007 | |
| vertex eff. | | | $0.809 \pm 0.0012$ | | | | | | |
| silicon eff. corr. | | | $0.72 \pm 0.06$ | | | | | | |

Table 9.5: Events surviving various cuts: For each set the first column gives the number of unlike sign events and the second column gives the number of like sign events. All the numbers for the monte carlo are unnormalised and correspond to the raw number of reconstructed MC events that survive the cuts.

## 9.6 Cross section Measurement

The cross section for $B\bar{B}$ is then calculated using the expression,

$$\sigma_{B\bar{B}} = \frac{\Delta N^{data} - \Delta N^{MC}_{Drell-Yan} - \Delta N^{MC}_{D\bar{D}} - 0.004 \times \Delta N^{data}_{J/\psi}}{\Delta N^{MC}_{B\bar{B}}} \times 10nb \qquad (9.24)$$

where $\Delta N^{data/MC} = (N_{unlike} - N_{like})$.

Table 9.6 & 9.6 gives the break-down in terms of the unlike and like sign pairs at each level of the cuts for various background and signal events generated. A corresponding column for the data is also present.

A visual scan of all the 8 events that survive the kinematic cuts was done. This

| Cuts | Data | | Monte-Carlo | | Backgrounds | | | | |
|---|---|---|---|---|---|---|---|---|---|
| | | | $\sigma_{B\bar{B}}$ (10$nb$) | | $\sigma_{D\bar{D}}$ (38$\mu b$) | | $\sigma_{Drell-Yan}$ (14$nb$) | $J/\psi$ mismeasured | |
| track + hit | 66 | 30 | 2.34 | 0.98 | 6.48 | 0.43 | 1.96 | | |
| mass | 41 | 28 | 1.57 | 0.63 | 4.82 | 0.14 | 0.23 | 0.16 | 0.01 |
| $p_t$ | 13 | 7 | 1.07 | 0.35 | 1.66 | 0 | 0.23 | 0.15 | 0.01 |
| impact | 7 | 1 | 0.87 | 0.26 | 0.95 | 0 | 0.15 | 0.11 | 0.0 |
| scan | 5 | 1 | all monte-carlo events survive this cut | | | | | | |
| total | 6<br>±2.45 | | 1.15<br>±0.11 | | 0.95<br>±0.26 | | 0.15<br>±0.20 | | 0.11<br>±0.03 |

Table 9.6: Summary of cuts in the data sample and the various monte carlo distributions. The monte carlo numbers are all normalised to the cross section shown in the table.

revealed that 2 out of the 7 events in the unlike sign sample had a misconstructed primary vertex which led to a significant impact parameter for the muon track with respect to the primary vertex. These two events were removed from the final event sample used to measure the cross section. Scanning the overlayed monte carlo beauty events did not show any such feature and had a 100% scanning efficiency. Hence, a correction for the scanning efficiency was not necessary for the monte carlo estimates used in the calculation. The excess left over after subtracting out all of the estimated background is $4.79 \pm 2.47$ events. With the expected rate of 1.15 events per 10 nb cross section for beauty production we measure the cross section as $42 \pm 22(stat)\ nb$.

The various contributions to the systematic errors are listed in the table 9.7. Though there is a large uncertainty associated with the charm cross section and also for the semimuonic branching ratio for charm decays, its effect on the final cross section for $b\bar{b}$ production is not the most dominant as the charm background

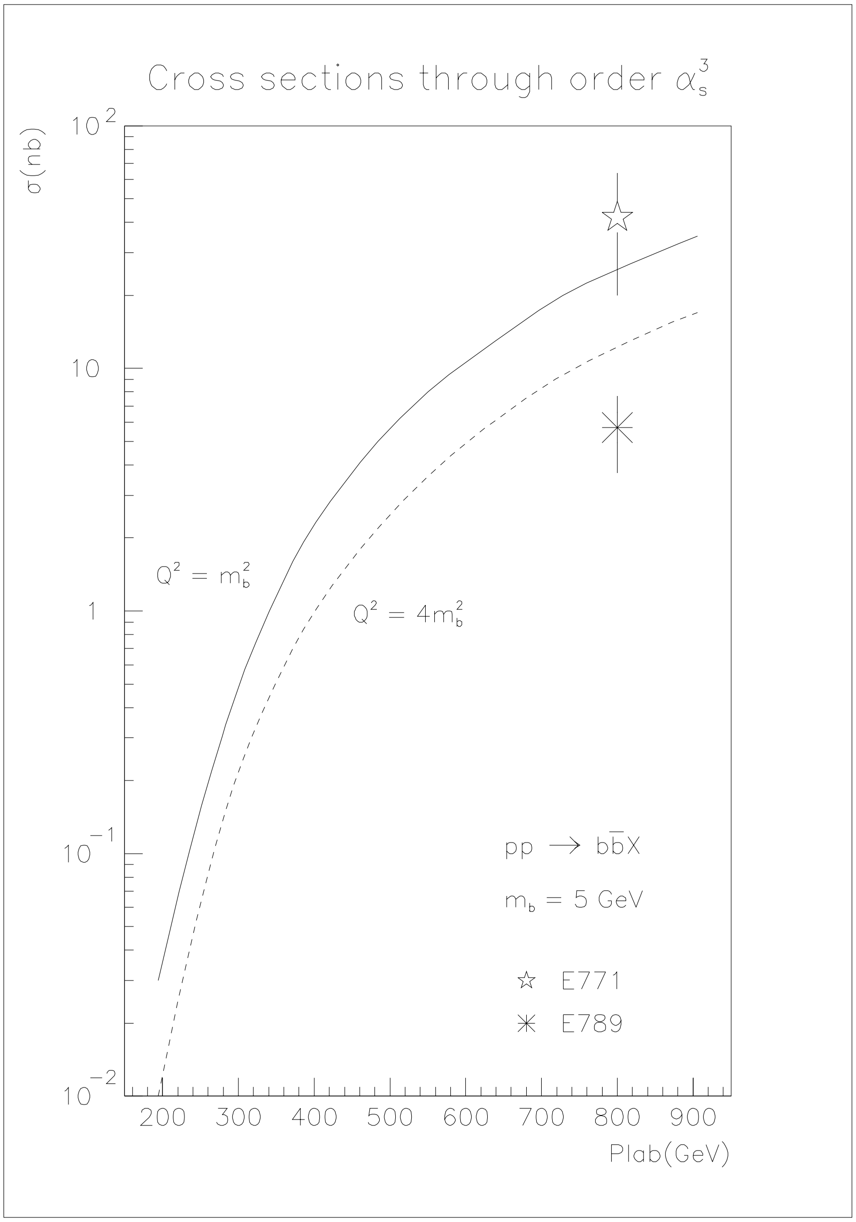

Figure 9.19: Shown in the figure is the theoretical prediction for the proton-Nucleus collisions to produce a $b\bar{b}$ pair. The E771 data point is indicated. The measured value is within errors, in agreement with the theoretical estimate. The uncertainty in the mass of the bottom quark, factorisation and renormalization scales contribute to the theoretical error.

| systematics | % | cross section |
|---|---|---|
| MC simulation | 10 % | 4.3 |
| beam | 5 % | 2.1 |
| silicon eff | 9% | 3.9 |
| D cross section<br>B.R.($D \rightarrow \mu$) | 25 %<br>30 % | 2.4 |
| B.R.($B \rightarrow \mu$) | 7 % | 3.1 |
| total | | 7.3 |

Table 9.7: Systematic errors

has been efficiently reduced by the choice of the kinematic cuts. The monte carlo simulation uncertainty of 10% gives an upper limit due to the choice of the parton distribution functions used by PYTHIA and the implementation of fragmentation in JETSET. The silicon efficiency used has an uncertainty of 9%. This is a result of the method used to estimate the correction factor for the silicon efficiency. The beam normalisation used in the measurement was known to an accuracy of 5%. The table 9.7 has the final total of the sytematic errors on the cross section added in quadrature to give 7.3 $nb$. The final result is

$$\sigma_{b\bar{b}} = 42 \pm 22(stat) \pm 7(syst) nb/nucleon$$

We had all along assumed that the amount of background that contaminates the unlike and like sign sample is essentially the same. Hence, subtracting the like sign events from the unlike sign events should yield the number of beauty events. Since we have such a low yield after all our cuts any effort at improving the statistical significance of the result need to be explored. From the monte carlo we expect to see no like sign events in the background after all the cuts. Hence we could add the unlike and like sign sample at this level to measure the cross section. A visual scan of the final events revealed a strong candidate in the like sign sample

| parameter | value |
|---|---|
| $M_{\mu\mu}$ | 3.36 $GeV/c^2$ |
| $P_t^j$ | 2.01 GeV/c |
| $P_t^k$ | 1.89 GeV/c |
| $dr_j$ | 1.125 $mm$ |
| $dr_k$ | 375 $\mu m$ |
| $n_{js}$ | $5+5+1$ |
| $n_{ks}$ | $5+5+0$ |
| $n_{jc}$ | $7+13$ |
| $n_{kc}$ | $5+12$ |
| $p_j$ | 59 GeV/c |
| $p_k$ | 48.8 GeV/c |
| $Q_j$,$Q_k$ | +1, +1 |
| $dy_j$ | 125$\mu m$ |
| $dx_j$ | $-1.125$ $mm$ |
| $dx_k$ | $-375$ $\mu m$ |
| $dy_k$ | 125 $\mu m$ |

Table 9.8: Candidate event characteristics. $j$ and $k$ are indices used to represent the leading and next to leading muon respectively. $dr$ is used for the 3D impact parameter and dx, dy for the same in projection. $n_{xx}$ is used to denote the front chamber hits. The second subscript denotes the silicon (s) and front wire chambers (c).

which we discuss in more detail. Fig. 9.20 displays this event in x-projection for the full spectrometer. The solid lines represent the muon track. and dashed lines the hadron tracks. The diamond shaped box denotes the primary vertex position estimated by the vertex finding routine. The secondary vertex is clearly visible in both x and y projections. The track numbered 17 has a solid match at the magnet midplane. In case of the other muon track in the event the match with the front track segment is less clear due to the higher track density. The event characteristics are listed in the table 9.8.

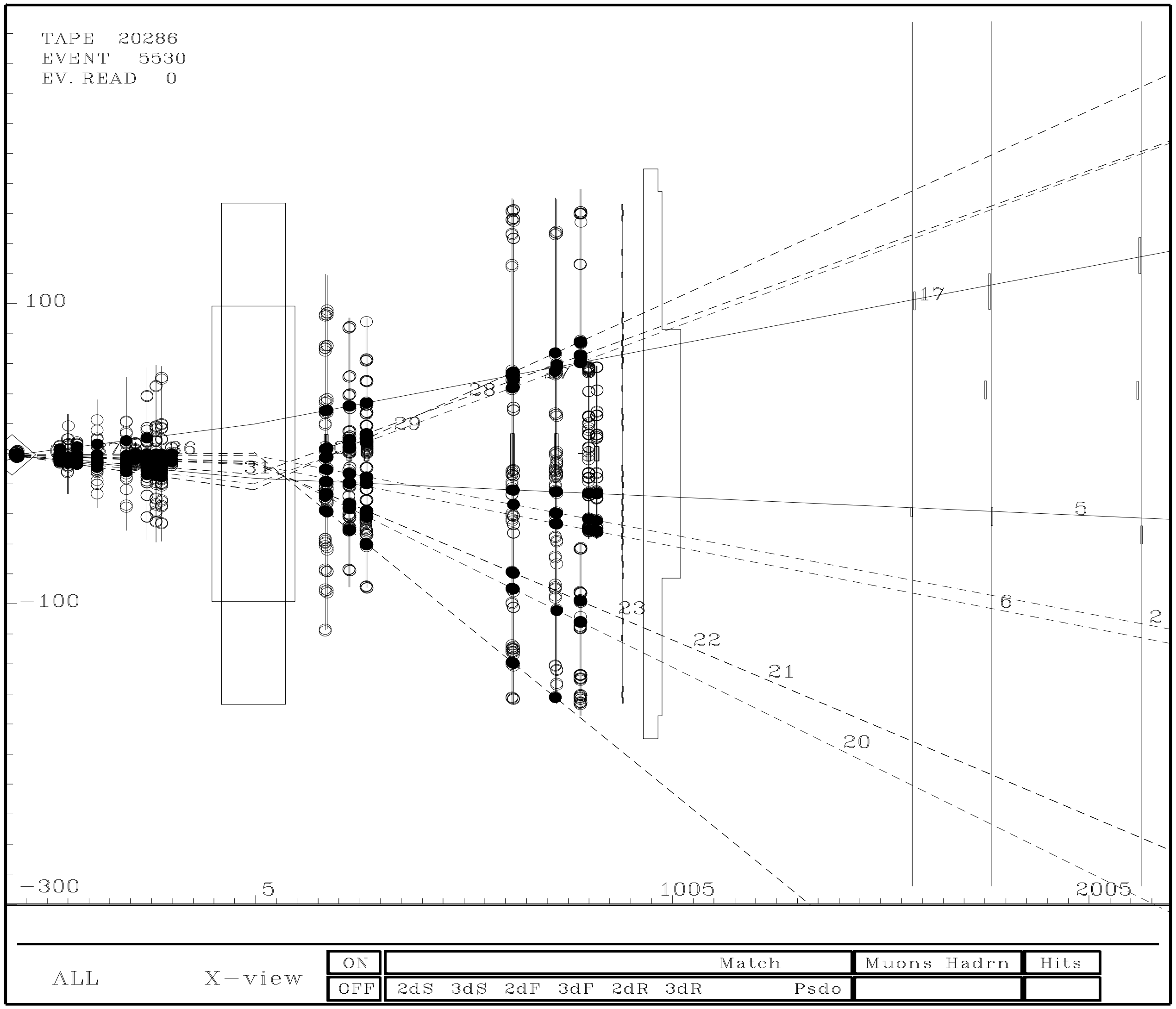

Figure 9.20: The only like sign event that survive all kinematic cuts and after a visual scan of the muon tracks show two good muon tracks with large impact parameter and stiff $p_t$ for the leading muon.

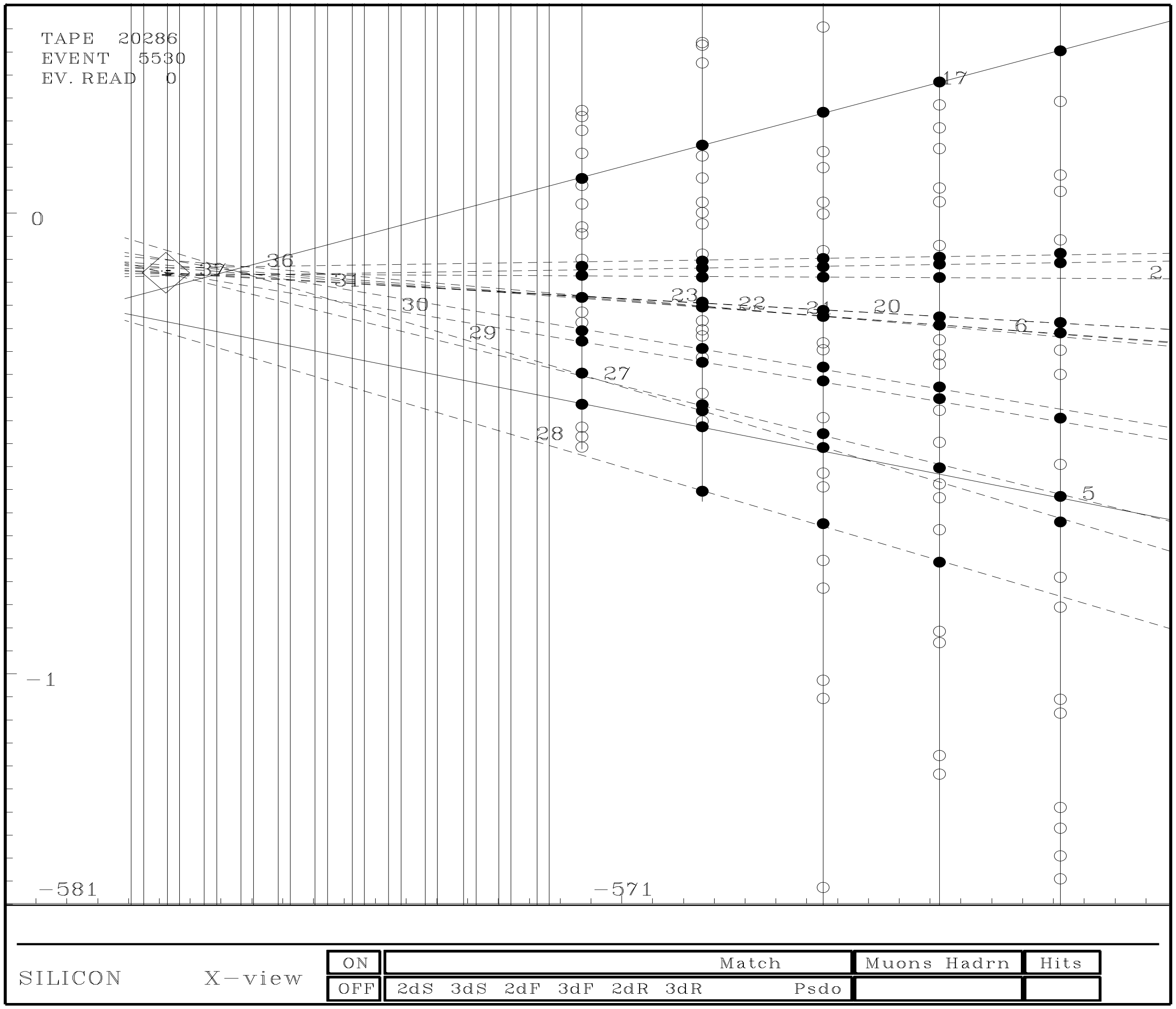

Figure 9.21: The same event discussed in the previous plot is shown with hits in the silicon x planes.

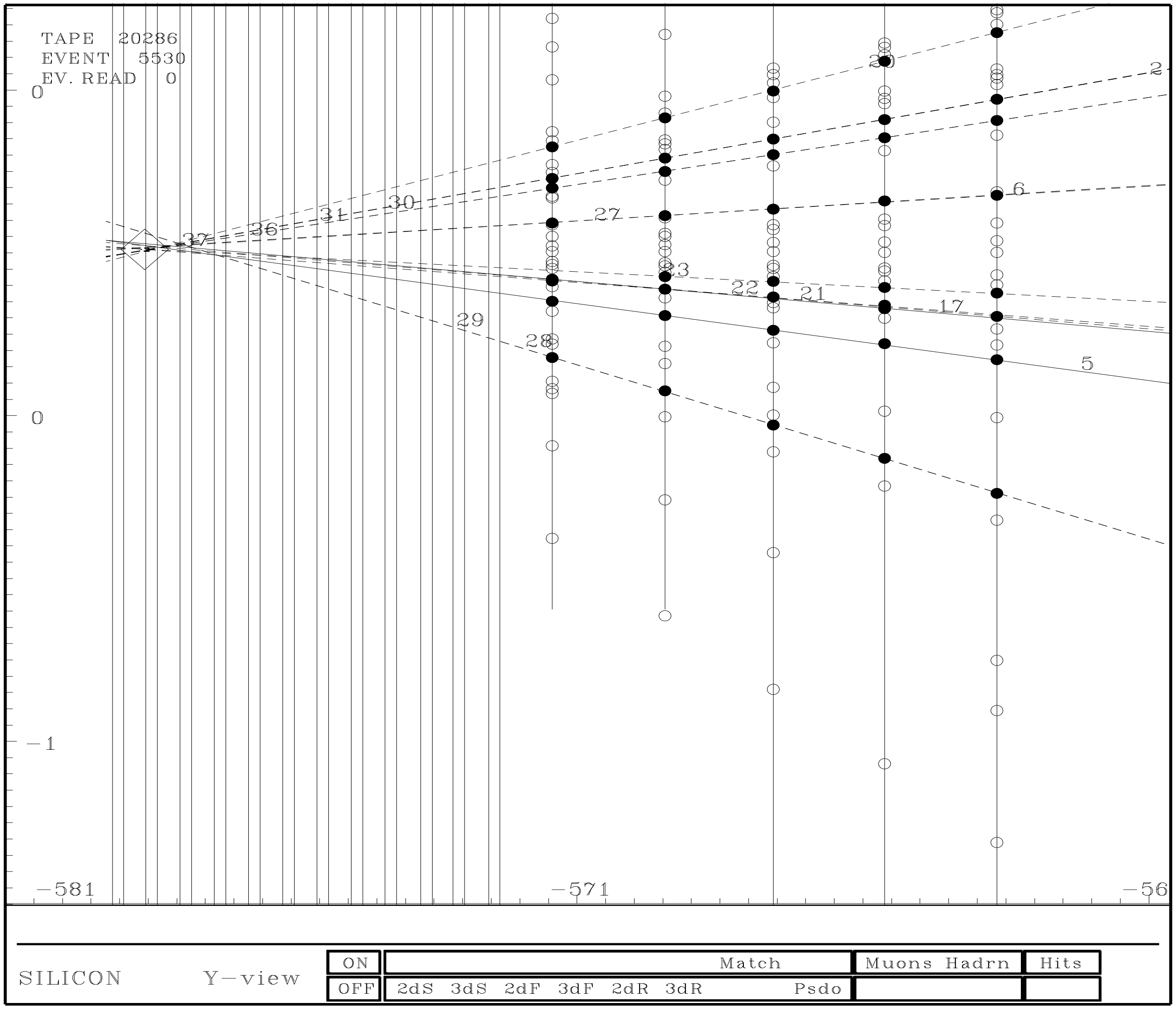

Figure 9.22: The same event discussed in the previous plot is shown with hits in the silicon y planes.

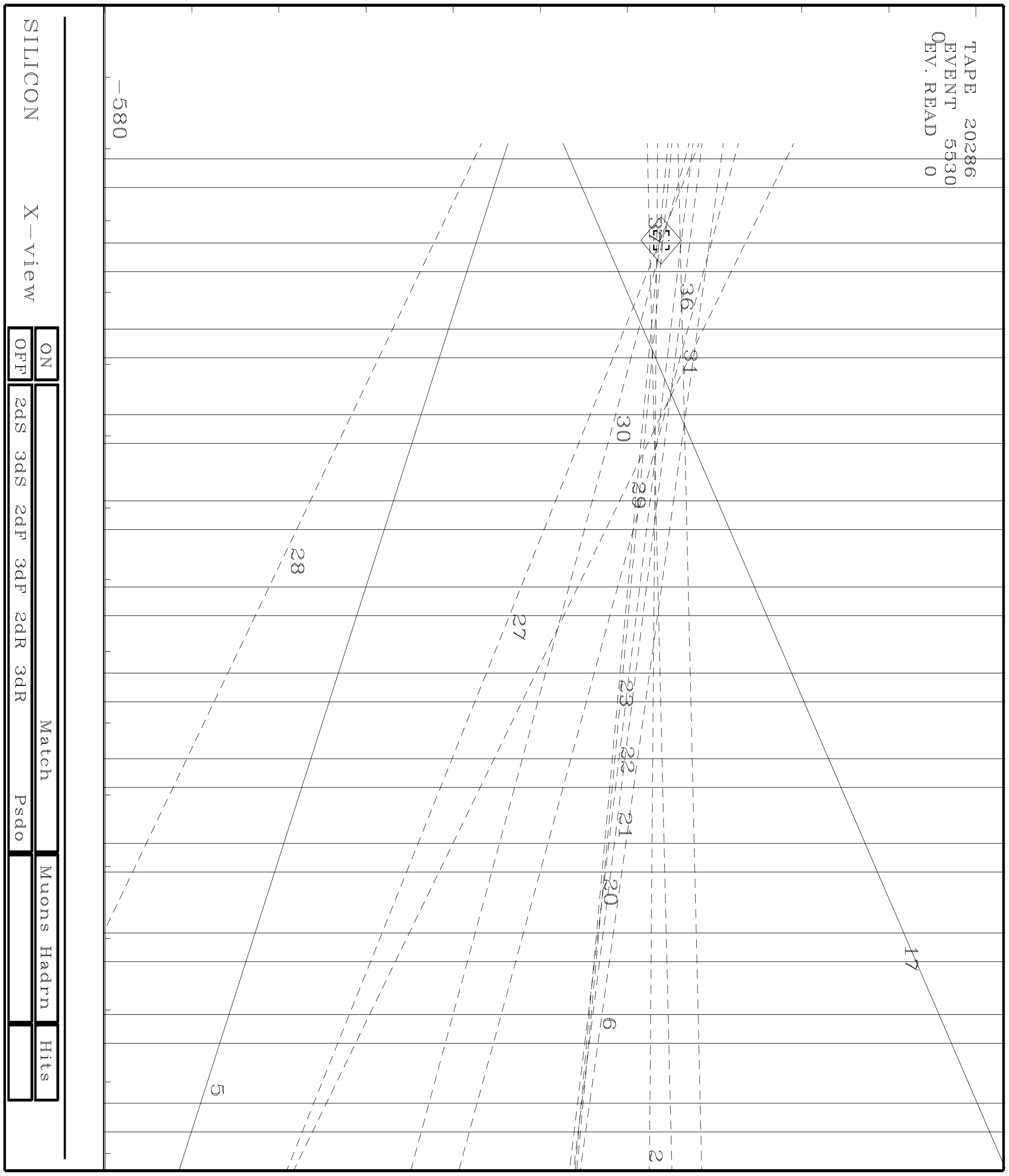

Figure 9.23: A closer look at the tracks projected into the target foils indicate a high probablity of a secondary vertex signifying a B decay topology.

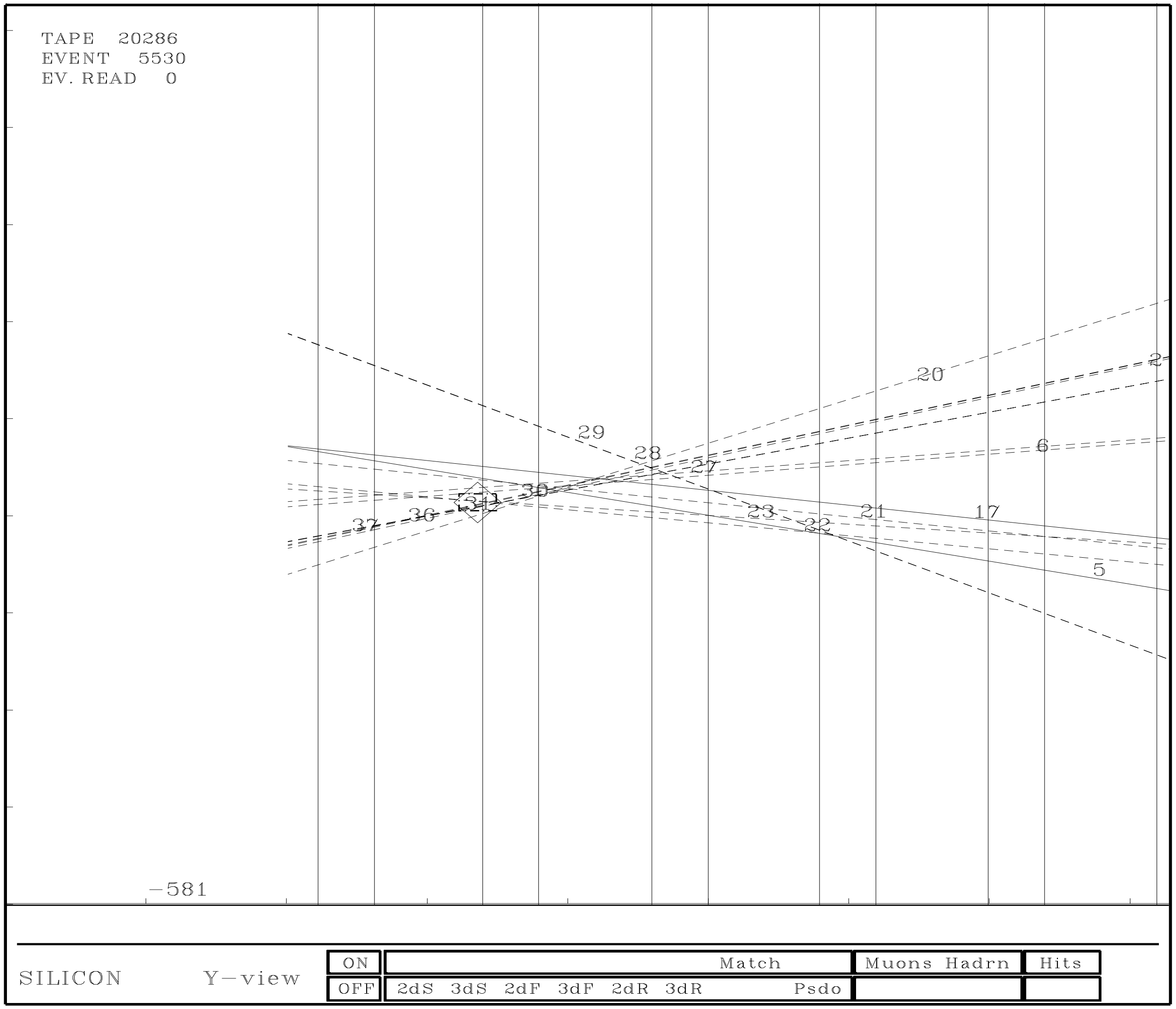

Figure 9.24: The y-view of the target region.

# Chapter 10

# Conclusions

In summary we successfully extracted 900 GeV/c protons parasitically from the Tevatron during collider runs, averaging at 100 KHz for the extraction rate. The average extraction efficiency was measured as 8.6±0.1 % and the average channeling efficiency was measured at 34 ± 4 %, which can be considered an upper limit for the extraction efficiency itself. It needs to be noted that we were essentially limited in the amount of beam extracted by an arbitrary limit of 1 kHz imposed by D0 for their tolerable losses, whereas CDF had their loss limit set at 5 kHz. In a special run with '36 on 3' bunches we reached extraction rates $>$ 500 kHz in the diffusion mode.

The beauty cross section for 800 GeV/c pN collisions was measured to be $42 \pm 22 \pm 7$ $nb$, where the large statistical error is due to the relatively small sample of beauty events after all the cuts were imposed. The number of front hits required on the muon tracks had to be increased in order to clean up the tracks to form the best muon candidate upstream of the analysis magnet. More tracking planes in front of the magnet could have increased the track finding efficiency. More u and v planes could have provided for better resolution in the y projection. This is important as candidate tracks are initially formed in each projection separately and then combined to construct a three dimensional fit. The efficiency drop in the central region of the silicon detector due to radiation damage from the high intensity beam, compounded the problem. Overall, an improved result could have been possible with a longer data taking period than was the case during the 1991 fixed target run for E771. It is interesting to note that the $\pi$N measurement (E672/E706) of the $b\bar{b}$ cross section ($75 \pm 31 \pm 26$ nb/nucleon) is on the higher side of the theoretical prediction. The $p$N measurement from E789 ($5.7 \pm 1.5 \pm 1.3$ nb/nucleon) is lower than the central theoretical value, whereas the E771 value is higher than the theoretical prediction but not inconsistent with the E789 measurement. The E789 measurement is extrapolated over all $x_F$ and $p_T$ due to the limited acceptance of their spectrometer.

As for the future it is interesting to ask whether an extraction scheme like that of E853 can deliver a beam rate to conduct a successful fixed target heavy flavor experiment at Fermilab. These issues have already been explored at some level before the successful completion of E853 at the HQ94 conference for heavy flavor studies at Fixed Target [31]. During the Main Injector era, with 36 bunches and approximately $1.2 \times 10^{13}$ protons circulating in the Tevatron an extraction efficiency of 25% would yield a 12 MHz beam using a bent crystal. There are ways to improve the extraction efficiency as it depends on the bend angle as well as the material of the crystal. In E771 a 4.75 MHz beam with a 5% interaction length target produced $1.6 \times 10^9$ charm pairs during a 30 day run period. Hence, such a scheme can produce of the order of $10^{10}$ charm events in a calendar year when run parasitic with collider operations. These numbers can be scaled down by a factor of $10^3$ due to the smaller cross section to get the beauty yield.

Carrigan [12] has explored the A0 area for extraction using a crystal. The bends required are 4.7 mrad in the vertical plane and 15.7 mrad in the horizontal plane at A0 to clear some of the obstacles downstream of it. A second crystal could be located at PV92, or conventional bending elements could be used to bend the beam back on to the fixed target extraction line. Such an extraction scheme using a bent crystal can be used to deliver a low intensity beam to the Fixed Target area during future collider operations at Fermilab.

# Bibliography

1. A. H. Sorensen and E. Uggerhoj, *"The Channeling of Electrons and Positrons"*, Scientific American June 1989 p96.
2. S.A.Bogacz, D.B.Cline, S.Ramachandran, *"Simulation Results of Bent Crystal Extraction in the Tevatron"*, Nucl. Instr. and Methods B 882 (1996).
3. R. A. Carrigan, Jr. and J. A. Ellison, *" Relativistic Channeling "*, (Plenum, 1987).
4. J. Thompson, *"Introduction to Colliding Beams at Fermilab"*, Fermilab-TM-1909 (1994).
5. G.Jackson, *Results from Beam Diffusion and Collimation Measurements in Preparation for Fermilab Tevatron Crystal Extraction*, Proc.1993 Part. Acc. Conf., Washington D.C., 1993.
6. G.Jackson, *"Extraction from the Fermilab Tevatron Using Channeling with a Bent Crystal"*,Proc.1993 Part.Acc.Conf., Washington D.C., 1993.
7. Z. Tang, *" Silicon crystal under bending "*, Fermilab-TM-1827 (Feb. 1993)
8. R.A.Carrigan et al., *"Extraction from TeV-range Accelerators Using Bent Crystal Channeling"*, Nucl. Instr. and Meth. B90 (1994) 128.
9. C.Thornton Murphy, *"Extraction from the Tevatron Using Channeling with a Bent Crystal"*, Proc. of DPF'92, Vol.2.
10. C. T. Murphy et al., *"First Results from Bent Crystal Extraction at the Fermilab Tevatron"*, Proceedings of the Workshop on Channeling and Other Coherent Crystal Effects at Relativistic Energies, Aarhus, Denmark, 1995, Nucl. Instr. and Meth. B119 (1996) 231.
11. R. A. Carrigan et al., *"First Observation of Luminosity-Driven Channeling Extraction at the Tevatron"*, to be submitted to Phys. Rev. Letters (1996).
12. R. A. Carrigan, Jr. *" Straw Man 900-1000 GeV Crystal Extraction Test Beam for Fermilab Collider Operation"*, Fermilab-TM-1978 (1996).
13. Valery Biryukov, *"Computer Simulation of the Tevatron Crystal Extraction Experiment"*, Phys. Rev. E, Vol.52, Number 2, Aug (1995).
14. E. Tsyganov and A. Taratin, *"Beam Halo Crystal Extraction from the Tevatron During Collider Runs"*, SSCL-Preprint-569, August, 1994.

15. A. Taratin et al., *"Ultrathin Crystal Scatterer for the SSC Beam Extraction System"*, SSCL-Preprint-545, December, 1991.

16. W. Gabella, J. Rosenzweig, R. Kick, and S. Peggs, *"RF Voltage Modulation at Discrete Frequencies, with Applications to Crystal Channeling Extraction"*, Particle Accelerators,1993, Vol.42(3-4), pp, 235-257.

17. B. S. Newberger, H. J. Shih, and J. A. Ellison, *"Effect of Betatron Motion on Particle Loss Due to Longitudinal Diffusion in High-Energy Colliders"*, *Phys. Rev. Lett.* 71 (1993) 356.

18. B. S. Newberger, H. J. Shih, and J. A. Ellison, *"Super Slow Extraction at the SSC Using Channeling in a Bent Crystal" Nucl. Instr. and Meth.* A325 (1993) 9.

19. D. Ritson, *"Obtaining Slow Beam Spills at the SSC Collider"*, in *Proceedings of the Workshop on B Physics and Hadron Colliders*, Snowmass (1993) 681.

20. H.Akbari et al., *"First Results on Proton Extraction from the CERN-SPS with a Bent Crystal"*, Physics Letters B 313 (1993) 491-497.

21. A.A. Asseev, E.A. Myae, S.V. Sokolov and Yu.S. Fedotov, *"On Increasing the Bent Crystal Extraction Efficiency by Using a Thin Internal Target"*, Nucl. Instr. and Meth. A324 (1993) 31.

22. H. Grote and C. Iselin, *The MAD Progam Users Reference Guide*, CERN/SL/90-13 (AP) (1990).

23. T. Murphy, *Internal Note-E853*

24. G. Kane, *"Modern Elementary Particle Physics"*, Addison Wesley.

25. S. W. Herb et al., *" Observation of a Dimuon resonance at 9.5 GeV in 400 GeV Proton Nucleus Collisions "*, Phy. Rev. Lett., 39, 252 (1977).

26. N. Kidonakis and J. Smith, *" Bottom quark production cross section at fixed-target pp experiments "*, ITP-SBB-95-16.

27. M. L. Mangano, P. Nason and G. Ridolfi, *" Fixed-target hadroproduction of heavy quarks "*, Nuclear Physics B405 (1993) 507-535.

28. S. Frixione, M. L. Mangano, P. Nason, G. Ridolfi, *" Charm and Bottom production: theoretical results versus experimental data "*, Nuclear Physics B 431 (1994) 453-483.

29. P. Nason and S. Dawson, *" The total cross section for the production of heavy quarks in hadronic collisions "*, Nuclear Physics B303 (1988) 607-633.

30. S. Ramachandran, *"Beauty Cross Sections"*, "Minneapolis Meeting DPF'96" (Minneapolis, Minnesota, 11/15 august 1996).

31. D. Christian, *"CHARM2000 at FNAL using crystal extraction"*, Proceedings of "HQ94 - 1994 Workshop on Heavy Quark Physics at Fixed Target" (Charlottesville, Virginia, 1994), in "Heavy Quarks at Fixed Target", Edited by B. Cox, Published by Istituto Nazionale di Fisica Nucleare, Laboratori Nazionali di Frascati, 53 (1994).

32. K. Lau, *"Rare Charm Decays in E789, E771 and WA92"*, Proceedings of "HQ94 - 1994 Workshop on Heavy Quark Physics at Fixed Target" (Charlottesville, Virginia, 1994), in "Heavy Quarks at Fixed Target", Edited by B. Cox, Published by Istituto Nazionale di Fisica Nucleare, Laboratori Nazionali di Frascati, 53 (1994).

33. S. Conetti, *"Fixed target B physics at Fermilab and the SSC"*, NIM A333, 142 (1993).

34. G. Introzzi et al., *"B Physics at FNAL E771"*, Nucl. Phys. B (Proc. Suppl.) 27, 257 (1992).

35. W. Selove, *"Detector Elements for a High-Rate Fixed-Target Beauty Experiment"*, Workshop on "Physics at Fermilab in the 1990's" (Breckenridge, Colorado, 1989).

36. B. Cox, *"E771 and Beyond"*, Workshop on "CP Violation and Fixed Target B Physics at Ultra-High Energies at UNK" (Dubna, USSR, 1989).

37. B. Cox, *"Beauty Hadroproduction"*, "Heavy Flavor: Status and Perspectives - 5th International Erice Workshop" (Erice, Italy, 1988).

38. B. Cox, *"Hadroproduction of Heavy Flavors"*, "Les Rencontres de Physique de la Vallee D'Aoste" (La Thuile, Italy, 1988).

39. *"Beauty Physics at Fermilab Fixed Target Energies"*, Proceedings of the "SLAC B Meson Factory Workshop", SLAC Report 324, 59 (1987), Fermilab preprint Fermilab-Conf-88/48 (1988).

40. S. Conetti, *"Dimuon experiments at the Fermilab High Intensity Laboratory"*, in "QCD hard hadronic processes", Edited by B. Cox, Plenum Press, 411 (1988).

41. T. Alexopoulos et al., *"Differential Cross Sections of $J/\psi$ and $\psi'$ in 800 GeV/c p-Si Interactions"*, Submitted to Physical Review D (1996).

42. T. Alexopoulos et al., *"Search for the Flavor Changing Neutral Current Decay* $D^0 \rightarrow \mu^+\mu^-$ *in 800 GeV/c Proton-Silicon Interactions"*, Phys. Rev. Let. 77, 2380 (1996).

43. T. Alexopoulos et al., *"Production of* $J/\psi$, $\psi'$ *and* $\Upsilon$ *in 800 GeV/c proton-silicon interactions"*, Phys. Let. B 374, 271 (1996).

44. T. Alexopoulos et al., *"Measurement of* $J/\psi$, $\psi'$ *and* $\Upsilon$ *total Cross Sections in 800 GeV/c p-Si interactions"*, Fermilab preprint Fermilab-Pub-95/297-E (1995).

45. T. Alexopoulos et al., *"The Fermilab E771 Spectrometer. A Large Aperture Spectrometer to Study Charm and Beauty States as Detected by Decays into Muons"*, Fermilab preprint Fermilab-Pub-95/348-E (1995), NIM A376, 375 (1996).

46. G. Introzzi et al., *"FNAL E771 RPC muon trigger"*, NIM A360, 334 (1995).

47. L. Antoniazzi et al., *"FNAL E771 fast muon trigger"*, NIM A355, 320 (1995).

48. A. Boden et al., *"Characteristics of the radiation damage seen in the silicon microstrip detector of Fermilab experiment E771"*, NIM A340, 491 (1994).

49. G. Cataldi et al., *"Performance of the E771 RPC muon detector at Fermilab"*, NIM A337, 350 (1994).

50. E. Gorini, *"Performance of E771 RPC muon detector"*, Scientifica Acta, VIII 3, 13 (1993).

51. A. P. McManus et al., *"Effects of High Energy Protons on the E771 Silicon Microstrip Detector"*, Radiation Physics and Chemistry 41, 427 (1993).

52. L. Fortney, *"Measurement of Localized Efficiency Loss in a Silicon Microstrip Detector Operated at High Intensity"*, Proceedings of the "Fermilab Meeting DPF'92" (Fermilab, Batavia 1992), Edited by C. Albright et al., World Scientific, 1684 (1993).

53. W. Selove, *"Di-muon and single-muon events from a beauty experiment"*, Proceedings of "Fermilab Meeting DPF'92" (Fermilab, Batavia 1992), Edited by C. Albright et al., World Scientific, 701 (1993).

54. S. N. Zhang et al., *"A High* $P_t$ *Muon Trigger Processor"*, IEEE Transactions on Nuclear Science, Vol. 39, 814 (1992).

55. L. Antoniazzi et al., *"The E771 RPC Muon Detector"*, NIM A315, 92 (1992).

56. L. Antoniazzi et al., *"The TRIGA Board for a Fast Muon Trigger for E771"*, NIM A314, 563 (1992).

57. L. Antoniazzi et al., *"Resistive Plate Counters Readout System"*, NIM A307, 312 (1991).

58. H. Gonzales et al., *"Status of the Silicon Strip High-Rate FASTBUS Readout System"*, Proceeding of the "1991 IEEE Nuclear Science Symposium" (Santa Fe, New Mexico, 1991), Vol. 2, 747 (1991).

59. L. Spiegel et al., *"A Combination Drift Chamber/Pad Chamber for Very High Readout Rates"*, Proccedings of the "1991 IEEE Nuclear Science Symposium (Santa Fe, New Mexico, 1991), Vol. 1, 381 (1991).

60. A. P. McManus et al., *"Performance of a Silicon Microstrip Detector in a Very High Rate Environment"*, Proccedings of the "1991 IEEE Nuclear Science Symposium (Santa Fe, New Mexico, 1991), Vol. 1, 298 (1991).

61. D. Christian et al., *"Status of the Fermilab designed E771 silicon strip readout system"*, Fermilab report (1991).

62. F. Grancagnolo, *"The RPC System of E771, Cosmic Rays Test Results"*, Proceedings of the "4th Topical Seminar on Experimental Apparatus for High Energy Particle Physics and Astrophysics" (San Miniato, Italy, 1990).

63. E. Gorini, *"The Resistive Plate Counter Muon System of E771"*, Proceedings of the "2nd International Conference on Advanced Technology and Particle Physics (Como, Italy, 1990).

64. F. Grancagnolo, *"The RPC as a Muon Detector: The E771 Experience"*, Proceedings of the "Symposium on Detector Research and Development for the Superconducting Super Collider" (Fort Worth, Texas, 1990).

65. M. Bowden et al., *"SSD Module Specification and As-Built Hardware Descriptions"*, Fermilab report TM-1747 (1990).

66. L. Spiegel, *"Upgrade of the Proton West Secondary Beamline"*, Fermilab report TM-1630 (1989).

67. D. E. Wagoner, *"Single Muon Distributions from Beauty in 800 GeV/c pp Interactions"*, Proceedings of the workshop on "High Sensitivity Beauty Physics at Fermilab" (Batavia, Illinois, 1987), Edited by A. J. Slaughter, N. Lockyer and M. Schmidt, 437 (1988).

68. W. Selove, *"Steps Toward High-Rate Fixed-Target B Physics"*, University of Pennsylvania Report UPR-161E (1988).

69. W. Selove, *"A High Rate Trigger System for E771"*, University of Pennsylvania Report UPR-0147E (1987).

70. Andy Boden, *"Observation and Reconstruction of B Mesons in p-Si Collisions at 800 GeV/c"*, University of California, Los Angeles (California), Ph.D. thesis, August 1993.

71. Dong Chen, *"The measurement of the Magnetic Moment of* $\Sigma^+$ *using channeling in bent crystals"*, State University of New York at Albany, Ph.D. thesis, July 1992.

72. M. Arenton et al., *"Proposal P867 - A proposal to continue the study of beauty and charm states in 800 GeV/c pN interactions"*, 69 pp. (1993).

73. T. Murphy, *"Beam Normalisation"*, Internal Note, (1995).

74. M. Arenton, *"Description of the End of Spill Data Record"*, Internal report, 9 pp. (1992).

75. P. Hanlet, *"The E771 Data Acquisition System"*, Internal report, 11 pp. (1992).

76. A. Blankman, *"The E771 1A*1B triggers"*, Internal report, 15 pp. (1992).

77. G. Corti, *"The 1A trigger"*, Internal report, 9 pp. (1992).

78. A. Boden and G. Introzzi, *"E771 Scintillator Muon Triggers"*, Internal report, 6 pp. (1992).

79. P. Hanlet, *"The LED and Random Triggers"*, Internal report, 3 pp. (1992).

80. Z. Cao, *"CPH and Scintillator Interaction Trigger"*, Internal report, 2 pp. (1992).

81. C. Wei and G. Mo, *"E771 Scintillator Beam Trigger"*, Internal report, 4 pp. (1992).

82. C. Wei and G. Mo, *"E771 Halo Veto Logic"*, Internal report, 4 pp. (1992).

83. C. Durandet, *"Silicon Interaction Trigger"*, Internal report, 8 pp. (1992).

84. A. Boden, *"E771 Silicon Detector Data Utilities"*, Internal report, 5 pp. (1992).

85. M. Recagni and A. P. McManus, *"E771 Proportional Wire Chamber's Postamplifier/Comparator"*, Internal report (1991).

86. B. Cox, *"Expected Yields of $B \to J/\psi \to \mu\mu$ in the 1991 E771 Summer/Fall Run"*, Internal report, 20 pp. (1991).

87. B. Cox and S. Conetti, *"Beauty Physics in E771 Using Single and Multimuons Triggers"*, Internal report, 27 pp. (1990).

88. M. Recagni, *"E771 Resistive Pad Counter's Latch Module"*, Internal report (1990).

89. M. Recagni and M. Haldeman, *"E771 Silicon Strip Detector's Auxiliary Board"*, Internal report (1989).

90. M. Arenton et al., *"Proposal P771 - An experiment to study beauty production and other heavy quark physics associated with dimuon production in 800 (925) GeV/c pp int."*, 56 pp. (1986).

91. P. L. McGaughey et. al., *"Cross sections for th eproduction of high-mass muon pairs from 800 GeV proton bombardment of $H^2$"*, Phys. Rev. D Volume 50, Number 5, 3038 (1994).